UNIVERSITY OF OTTAWA

FACULTY OF GRADUATE AND POSTDOCTORAL STUDIES

DEPARTMENT OF MECHANICAL ENGINEERING

Development of a Multi-Body Autonomous Inspection Robot for Small Diameter Pipes

Author:
Jeff LAMONDE

Supervisor:
Dr. Eric LANTEIGNE

uOttawa

July 14, 2017

Abstract

The pipeline network of North America is thousands of kilometer long and is ever increasing. To ensure the safety of every individual whose lives are affected by this network, the inspection of the pipelines are mandatory. With the steady progress and downsizing of robotic components, the wireless inspection of smaller pipelines is now a possibility and is the principal driver of this research. Mainly, the scope of this project is to explore the feasibility of the fabrication of a robot to inspect pipes of diameter of six to eight inches. Various design possibilities and the inherent problems of small confined environments inspections are investigated. The parameters for the fewest number of collisions for the design of a pipe robot is presented and various pipe scenarios are simulated. Finally, a prototype is fabricated and recommendations are suggested for future subsequent iterations of the robot.

Contents

List of Figures

List of Tables

List of Abbreviations

3D	three-dimensional
cm/s	centimeter per second
dia.	diameter
DC	Direct Current
g	gram
Hz	Hertz
in	inch
kg	kilogram
kHz	kiloHertz
km	kilometer
m	meter
MFL	Magnetic Flux Leakage
mm	millimeter
mNm	milliNewton-meter
m/s	meter per second
m/s^2	meter per second square
N	Newton
Nm	Newton-meter
oz-in	ounce-inch
PID	Proportional-Integral-Derivative
rpm	revolution per minute
s	second
V	volt
W	watt
μm	micrometer

1 Introduction

There are many ways to transport water, natural gas or oil and the pipeline is one of them. This mean of transportation has been used for centuries [1] by other civilizations and remains relevant to this day. These ancient pipelines were made of lead, bamboo or clay, rather than the more popular steel or plastics of today, but they still served their purpose to deliver water or gas to a more densely populated region.

Just as they were initially, pipeline systems are a very efficient way to transport liquid or gas. They require high investment costs, but the cost to transport the good per unit of volume drastically falls when the installations are in operation [1]. Pipelines are more economical than other means of transportation for liquid or gaseous products such as trucks and trains and is most certainly a reason of their popularity[1].

As of 2014, there was more than 2,000,000 km of pipelines in the United States alone [2]. A great number of these major oil and gas pipelines were built during World War II and some even as early as the 1930's and are still in use today [3]. It means that many of these pipes are more than 50 years old and will probably be in need of replacement or repair over the next few years. In order to prevent a natural disaster, these pipelines must be inspected at regular intervals. Especially knowing that after 30 years of service, the likely of damages to the integrity of the pipe is increased. [4] Also, the construction of pipelines is not likely to stop anytime soon, as many companies have projects to build additional lines [5]. Consequently, an increasing amount of pipeline will have to be inspected for defects.

Inspection is an important factor in the life of a pipeline for many reasons. Firstly to prevent any harm or damage to individuals or the environment in the event of a leak, a rupture or an explosion. A sudden stop in the delivery of a pipeline system would also cause shortages in products at the receiving end of the pipeline and could lead to financial losses.

Many different inspection methods have been developed by companies and research institutes in recent years to address this alarming situation. Since pipelines are confined environments improper to human inspection, robots were developed to gather data and images of pipes. Nonetheless, some interesting points brought up by other researchers in pipe inspection robotic systems gave fuel to develop a specific solution to the general pipe inspection problem.

Many existing pipe inspection robots suffer from the fact that they are tethered. While typically this scenario provides more control over the robot, it requires a manipulator on site and also has a maximum range dictated by the cable length.

1.1 Objectives

The main objective of this research is to design a multi-body autonomous mobile robot for small diameter pipe inspection. This very broad objective is sundered in various smaller tasks the robot should accomplish. The robot should first of all be able to move through various pipe environments. A pipe environment is a semi-controlled setting. It is technically supposed to be evenly shaped, clean and have only a certain number of possible connections. In this scenario, the robot should be able to operate in straight pipes of 6 in to 8 in as well as any change in diameter between these two boundary values. The robot should also be able to move through 0° to 180° pipe bends of radii as small as one and a half diameter. Example pipe configurations the robot should be able to navigate through are shown on Figure 1.

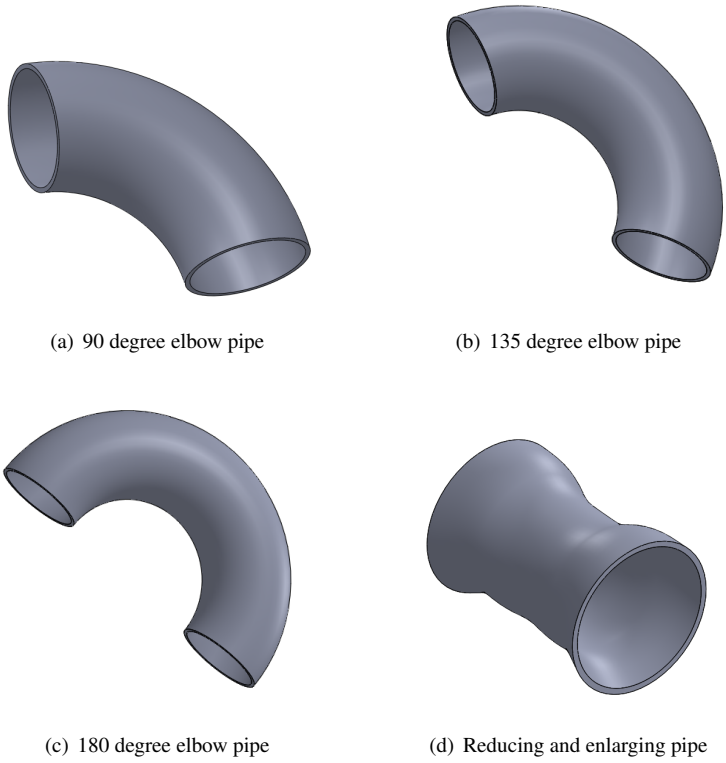

(a) 90 degree elbow pipe

(b) 135 degree elbow pipe

(c) 180 degree elbow pipe

(d) Reducing and enlarging pipe

Figure 1: Pipe configurations the robot should be able to navigate in

The robot should also be able to operate in any direction. Which means it should be able to move horizontally, vertically, or any angle in between. In addition, the robot should be able to find and locate abnormalities inside a pipe. The objective is to locate as small a defect as possible. Finally, the robot should operate wirelessly and

autonomously. In other words, it should be able to advance in a pipe in any situation previously described without any human intervention.

The goal of this thesis is the determination of important design parameters for navigation without collision of the pipe inspection robot and on the development and fabrication of the mechanism.

1.2 Contribution

The work of this research provided optimized values for multiple design parameters, such as the size of the wheels, the spacing between the shoulder joints and the length of the trailer joint to allow the entire robot assembly to navigate in a pipeline without singular configurations. The design of two modules with different purposes has also been suggested. A power module to carry other passive modules as well as a sensing module to inspect the pipelines it travels into.

Simulations have also been performed to evaluate the impact of different parameters and to find values for them that don't cause any collision during navigation. Numerical results have been obtained through simulations. Finally, recommendations have been proposed to improve the design of both modules on subsequent iterations of the robot.

1.3 Organization

This thesis will be organized as follows:

Literature Review An overview of the various technologies and advances in pipe inspection and navigation robotics is presented in Chapter 2. This literature review encompasses many aspects of pipe inspection, from the backbones of the drive mechanisms to the sensing devices.

Preliminary Designs The first iterations of the design from the first hand sketches to the final computer-assisted drawings are presented in Chapter 3 along with details of the design process.

Conceptual Design Chapter 4 discusses the decisions for the robot's mode of locomotion and sensing and the the overall geometry for operation without collisions.

Simulation Multiple simulation scenarios of a computer model of the robot in various situations in order to get data on collisions as well as motors positions and speeds are presented in Chapter 5.

Discussion and Manufacturability The advantages as well as the drawbacks of the current design as well as improvements for a subsequent design are discussed in Chapter 6. Also, the first prototype built is shown and detailed.

Conclusion Finally Chapter 7 summarizes the presented ideas and proposed design.

2 Literature Review

In this chapter, various sensing and inspection devices will be evaluated. Pipe inspection robot architectures and locomotion methods will be evaluated for use in pipe diameters of 6 to 8in.

2.1 Sensing

This section will discuss various sensing devices that are typically used in robotic pipe inspection. These four types of sensors were considered: cameras, lasers, ultrasonic sensors and magnetic flux leakage sensors.

2.1.1 Camera Inspection

Pipes are commonly inspected by visual means through a camera. This can be done by having a live monitor that shows the instantaneous images as they are being taken by the camera on the inspection robot or the robot records images and videos during the inspection to analyze later [6]. While these methods are straightforward and arguably the easiest inspection method to implement, they rely on human supervision and therefore have inherent uncertainty.

Some advantages of camera inspection of a pipeline include the small size of the device itself and low energy requirement. Newer cameras of small sizes can record good quality images and videos and at a relatively small cost. This makes the camera a good redundant inspection device. It requires little energy and space, at the expense of giving more qualitative than quantitative results.

Some disadvantages of camera inspection is the time required to analyzed the gathered results. If human work is required, then the inspection of long pipelines might be costly in time and salary. Also, videos and images tend to take a lot of memory space. Even if digital memory has been shrinking in size for many years, it could be an issue on untethered robot.

2.1.2 Laser Inspection

Laser inspection technology makes use of lasers to inspect or measure the interior of a pipe. This can be done in different ways. The laser can be projected on a cone and then be reflected on the pipe wall [7] or by actually filming two lasers being projected on the pipe wall at different angles [8] or by using a laser proximity sensor to detect the distance between the robot and the wall, [9], among many other methods. Even though all these methods make use of lasers, their data collecting methods differ greatly. Two methods will be explored in further details.

Conical Triangulation One way to measure the quality of a pipe interior with a laser is with conical triangulation. Is this method, a laser beam is reflected on the surface of the pipe using a conical mirror and the resulting ring of light is analyzed through a camera. The process is illustrated on Figure 2.

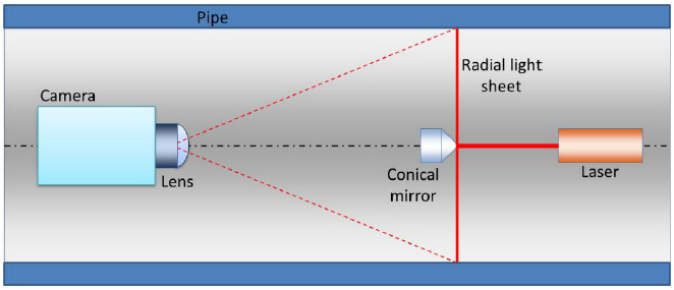

Figure 2: Principle of conical triangulation [7]

This method has been used to evaluate the quality of a pipe interior[7, 8, 10]. This method actually links two method of inspection in one. A laser beam is projected on a surface and a camera gathers the data. This method can be precise to less than 1 mm, but necessitates some other important details to function properly. The robot moving through the pipe has to be perfectly centered with the pipe axis and the laser beam must be reflected exactly at a right angle to the pipe surface to take useful data. Otherwise the ring of light would be distorted and yield poor results. In addition, a camera usually gathers images that are distorted and needs calibration. It's possible to see how a typical image is distorted by a camera lens on Figure 3.

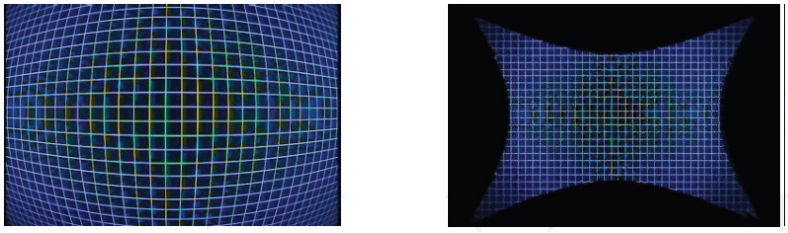

(a) Image before calibration

(b) Image after calibration

Figure 3: Typical camera image calibration process [8]

Also typically on these robots, an encoder measuring the distance traveled by the robot is used to tell the robot to take a picture of the ring of light after a certain distance to get data that are evenly spaced. However encoders are susceptible to slippage of the wheel and some other sort of encoder would need to be used independently of the wheel encoder to easure the traveled distance of the robot. So even though this scenario requires many parts and critical adjustment, it gives very precise data that can

be analyzed rapidly.

Proximity Sensors Pipe distance measurements can also be made using the proximity sensor method [9]. In this method, the theory of light beams is used. More specifically, a laser beam is emitted from a source, bounces on a reflective surface and is returned to a receiver. Thus, knowing the speed of a laser beam in air and the time it took to come to the emitter, it's possible to get the distance from the sensor to the measured surface. The process is shown on Figure 4.

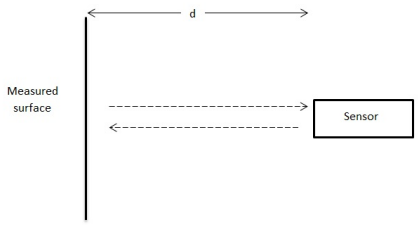

Figure 4: Proximity sensor measurement principle [11]

However, this method yields only a single measurement data point, the distance of a laser dot from the sensor. Therefore the idea with this method of inspection to get more data is to have many sensors working simultaneously or have fewer sensors being rotated around the pipe axis to gather data for the whole circumference of the pipe. Similarly as with the previous method, an encoder is required to know at what speed the robot is traveling to match the measurements with distance traveled by the robot. If many laser sensors are used, then it can get costly and would increase the overall size of the robot. On the other hand, if one laser sensor is rotated around the pipe axis, fewer parts are required, but a motor and an encoder are needed. This method also requires the robot to remain centered on the pipe axis.

2.1.3 Magnetic Flux Leakage Inspection

The quality of a pipeline can also be assessed using magnetic flux leakage technology. More specifically, this technology uses a strong magnetic field to carry a magnetic flux into the pipe wall. The flux created is strong enough so that the pipe wall is saturated and the remaining flux leaks out. At this point, hall effect sensors measure the density of the leaked magnetic flux as they travel along the pipe with the robot. This method has been used for the inspection of pipeline wall from within and from the outside on exposed pipelines [11],[12].

Generally, robots that use this method of inspection to inspect from within use a circular array of hall effect sensors distributed evenly around the pipe axis. These sen-

sors then measure the variations in the magnetic flux. As long as the wall of the pipe remains of even thickness, the flux density stays the same. Therefore, if there is a change in flux density, it means that the material is thinner or thicker. So these variation in thickness can possibly mean erosion in some parts of the pipe or damage or a weld joint for instance. The intensity of the flux leakage is proportional to the change in thickness, or to the size of the gap if there is one. The principle is shown on Figure 5.

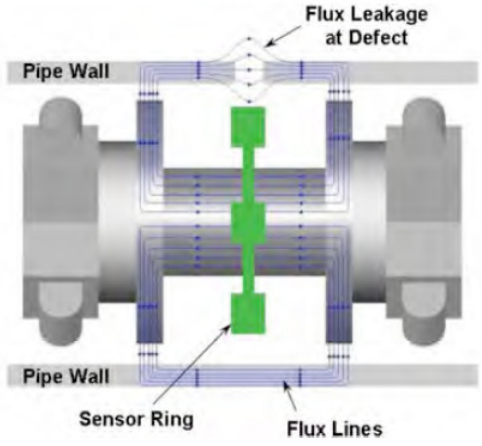

Figure 5: Magnetic flux leakage inspection method [11]

The magnetic flux leakage technology allows the measurement of a pipeline quality without the need for propulsion since this method works even when the fluid in the pipeline is flowing. However it also comes with a loss of control over the speed of the robot and therefore also on resolution as well. Typically, large robot gathering data using magnetic flux leakage carry multiple sensors to counter this limitation, which is not possible on small robots inside small pipelines, because of the lack of physical space. Lastly, MFL technology works with magnetic fields and is necessarily limited to ferrous pipelines.

2.1.4 Ultrasonic Inspection

Another inspection method considered is ultrasonic sensors. This method, explained by Beller [13], uses acoustic emitters and sensors in order to measure the pipe wall thickness, noticing variations where defects are present, whether the defects are inside the pipe or outside the pipe as it is shown on Figure 6.

The emitted ultrasound will go through the material and also bounce back from the outer wall. This echo can also be monitored by the receiver to measure to thickness of the pipe by knowing the distance to the front wall and the distance to the back wall.

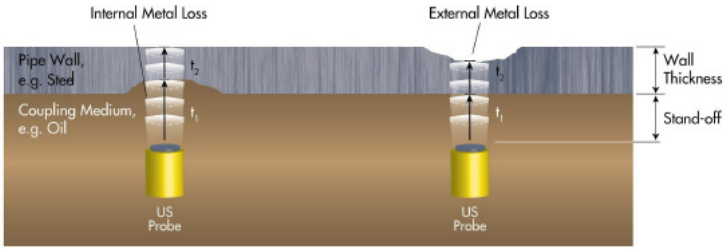

Figure 6: Ultrasonic inspection method [13]

This obviously depends on the thickness and the quality of the sensor used.

One of the advantages of this method is that it can be used in in almost all pipe environments and materials and can also detect cracks as well as corrosion. However, like laser inspection, ultrasonic sensors get only a single data point at a time of distance to the nearest obstacle. So multiple sensors are needed to gather data in different different directions, or the sensor has to be moved, which can increase the size or the complexity of the robot. Finally, ultrasonic inspection can be complicated on curved pipe walls, as the ultrasonic wave tends to bounce off the walls erratically.

2.1.5 Other Sensors

Other types of sensors have been explored, though they were uncommon in the literature. The infrared proximity sensors typically have low precision although newer sensors such as the high-precision IR displacement by Sharp has a $50\mu m$ resolution[14]. As precise measurements are required, infrared sensors are out of the equation. Also, mechanical measurement of the pipe surface was considered. Though this method has been used[15], it is not the most efficient method of measurement for pipe wall surfaces. This method requires arms that bend on the pipe wall and by measuring the deformation of the arm, it's possible to know the distance from the arm shoulder to the pipe wall, therefore detecting defects. This method only detects defects that fall under the arms during travel, so assessing all the circumference of the pipe with such devices is difficult. Finally, X-Ray sensors have been considered for use in a mobile robot, but haven't been selected for the array of sensors of the proposed robot because X-Rays are very energetic rays that would rapidly deplete the batteries of an autonomous robot. Also, this kind of imaging would be qualitative assessment of the pipeline because the gathered images wouldn't clearly indicate defect measurements and individual analysis of every image would have to be performed by humans, which is not the objective. A regular camera for data redundancy would be sufficient and easier to implement being much more common than X-Ray sensors.

2.1.6 Resolution

This robot is designed with the idea of taking measurements while running along the pipe. Therefore, there can only be a limited amount of data to be gathered by unit length of pipe. The robot is taking measurements continuously, but is also moving at a constant speed, so there will always be a gap between two measurements. It's important to know the length of this gap, since it is proportional to the minimum size of a detectable defect. But in order to do so, it's necessary to have the measurement frequency of the sensor f_m in measurement per second and the linear speed of the robot V_{lin} in m/s since they dictate the gap size. The resolution then would be:

$$R_{axial} = f_m \left[\frac{\text{measurements}}{\text{s}}\right] \frac{1}{V_{lin}} \left[\frac{\text{s}}{\text{m}}\right] \quad (1)$$

$$R_{axial} = \frac{f_m}{V_{lin}} \left[\frac{\text{measurements}}{\text{m}}\right] \quad (2)$$

In the case the measurements would be taken radially, or around the interior circumference of the pipe, the equation would change a little bit. Thinking in terms of a rotating motor with speed ω_{motor}, the calculation would be:

$$R_{radial} = f_m \left[\frac{\text{measurements}}{\text{s}}\right] \frac{1}{\omega_{motor}} \left[\frac{\text{min}}{\text{turn}}\right] 60 \left[\frac{\text{s}}{\text{min}}\right] \quad (3)$$

$$R_{radial} = \frac{60 f_m}{\omega_{motor}} \left[\frac{\text{measurements}}{\text{turn}}\right] \frac{1}{\pi D_{pipe}} \left[\frac{\text{turn}}{\text{m}}\right] \quad (4)$$

$$R_{radial} = \frac{60 f_m}{\omega_{motor} \pi D_{pipe}} \left[\frac{\text{measurements}}{\text{m}}\right] \quad (5)$$

The maximum size of an axial defect $L_{axial\ defect}$ that could be missed would be the length between two measurements. It would be calculated this way:

$$L_{axial\ defect} = \frac{1 \text{ measurements}}{R_{axial}} \quad (6)$$

$$L_{axial\ defect} = \frac{1}{R_{axial}} [\text{m}] \quad (7)$$

In order to get the maximum size of a radial detectable defect, a similar procedure can be applied. It woulg go like this:

$$L_{radial\ defect} = \frac{1 \text{ measurements}}{R_{radial}} \quad (8)$$

$$L_{radial\ defect} = \frac{1}{R_{radial}} [\text{m}] \quad (9)$$

2.2 Wheeled Robots

There has been a lot of development on pipe crawling robots in the last few years and many researchers came up with very different ways to power and steer their robots in pipes. The major design concepts are the line, the triangle with wheels and the triangle with tracks. Additionally, some other original designs have been proposed and will be discussed.

Since the previously studied designs all address the same efficiency problematic, other research has been done on the subject to incorporate wheels to these design to maximize efficiency during long travels inside pipes. These designs are separated in two different categories: Vehicle robot [16, 15, 17, 18, 19, 20, 21, 22] or Train robot [23, 24, 25].

The main difference between these two types of robot is the number of wagons or sections they have. A vehicle robot has only one driving section, or module, while a train robot has multiple sections each equipped with the same locomotion apparatus. Both have their advantages and drawbacks. The vehicle robots are usually lighter and more efficient while they can be limited in the type of environment they can be put into. In difficult to operate conditions, like a 90 degrees L-turn or T-junction in a pipe, a train-like vehicle has the major advantage of being able to be powered by other wagons when the first wagon, or head wagon, faces such a situation. The different design ideas, or architectures, surrounding wheeled robot are presented in the following section.

Even though many different architectures exist, an article from N.S. Roslin $et\ al.$ [20] compares the major types of design in much details. The architectures compared in this article are the line, the wheeled triangle and the tracked triangle types of robots. Although not every possible type of robot is presented and the data is not quantitative, the analysis provides a broad overview of the most typical pipe crawling robots. The data is presented in Table 1.

The data presented in Table 1 provides insightful information on the behavior of various types of pipe crawling robots. Since the desired robot has to travel in pipelines of any diameter from 6 to 8 in while carrying sensors for inspection, some criteria from the table are more important than others. Suitability in curved, vertical and horizontal pipes, diameter adaptation and multiple bodies are crucial qualities for the desired robot. Therefore, the two triangle types seem more suited for the required tasks than the line type. However, with the data from Table 1, it is still uncertain whether the tracked type or the wheeled type would be the most desirable design in a pipeline environment. The higher efficiency of the wheeled type is a major advantage over the tracked type though, as the robot is to be used in a semi-controlled environment of a pipeline that is theoretically clean and unobstructed.

Table 1: Comparison of the different types of inspection robots

Type	Tracked Triangle	Wheeled Triangle	Line
Suitability	Curved pipe Horizontal pipe Vertical pipe Uneven surfaces	Curved pipe Horizontal pipe Vertical pipe	Curved pipe Horizontal pipe Vertical pipe
Advantages	Diameter Adaptation Omni-directional Large contact area High traction Centered Multiple bodies	Diameter Adaptation Less friction High speed High mobility Multiple Bodies Centered	Obstacle avoidance Small radius turns Minimal actuators Lighter Smaller
Disadvantages	High friction Requires large radius	Requires large radius Requires flat surfaces	Little dia. adaptation Single Body Not centered Requires flat surfaces

2.2.1 Line Type

The line type robot is a design that consists of opposed set of wheels that provide traction to the robot, as seen on Figure 7.

This slender design allows more space to mount cameras on the side as well as good steering abilities. [17] This design also can adapt to different pipe diameters and is very versatile as it can avoid some obstacles in the pipe. It requires spring loaded arms and DC motors on each side preferably. Moreover, this structure is rather simple and open and therefore has room for other components, like sensing devices. The most prominent foreseeable problem to this design is the possible difficulty this type of architecture would face in a pipe bend. The low number of contact points between wheels and the wall might cause singularity configurations in sharp corners or other such scenarios.

2.2.2 Wheeled Triangle

Similarly to the line type, there is the more common triangle design. It consists of sets of three wheels spaced equally of 120°. Many different researchers developed this concept[16, 26, 27]. An example wheeled triangle robot design is shown in Figure 8.

Since it is the same general idea as the previous line type, they share many advantages. However, adding an extra set of wheels necessarily increases the the number of components and size of the robot.

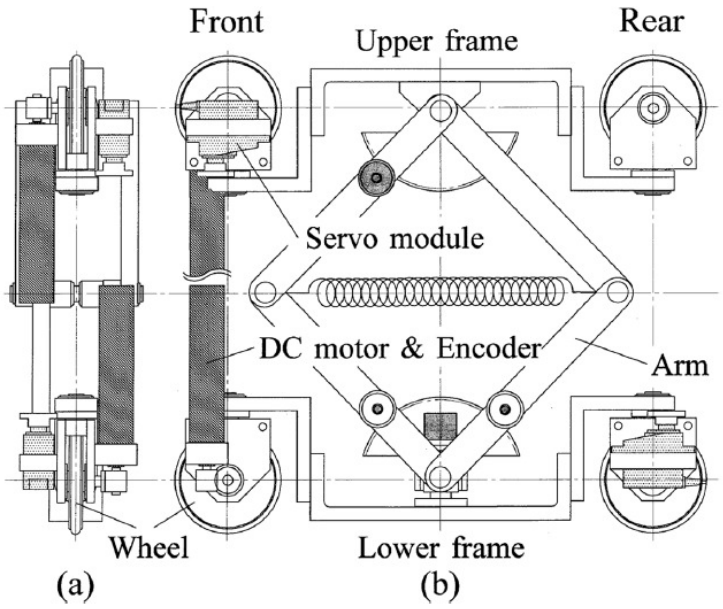

Figure 7: A line type of robot [17]

Another variation of this subcategory of robots is the tracked triangle style[28, 29, 30]. In this design,tracks are used instead of wheels. Using tracks allows inspection of almost any type of pipes as they can handle damaged pipeline, large obstacles and different diameters[20].This can be done at the expense of more energy consumption as tracks are less efficient than wheels. Otherwise, this design has similar features to the wheeled triangle design: It can adapt to different diameters, it can carry sensors and can be used as a train robot if desired; an example of which is shown on Figure 9.

2.2.3 Four Wheels

Some designs are also built with four wheels. These robots gain stability, but are less energy efficient since there is one more wheel causing friction on the pipe wall and requires multiple springs to be continuously loaded to adapt to different pipe configurations. This design can be useful in situations leading to possible singular configurations because more wheels can remain in contact with the wall. An example of such situations is shown on Figure 10.

This very flexible design however comes with the drawback of being possibly more difficult to use as a train-like robot than other designs. Mostly because the robot can move in any four directions. However if would not be impossible to link multpile instances of this design to travel inside pipeline. Also, this design is not meant to go

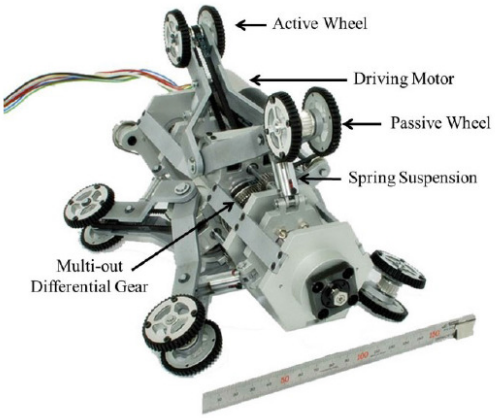

Figure 8: A three wheel type of robot [27]

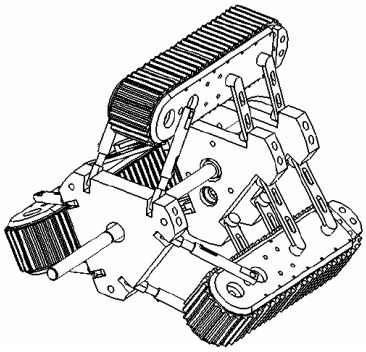

Figure 9: A typical three tracks robot

along the axis of the pipe. While this is not a problem in itself, it might cause issues if onboard sensors need to be aligned with the pipe axis. On the other hand, this design can adapt to various pipe diameters and has room for some sensors.

2.2.4 Hypermobile Robots

Hypermobile robots have a greater number of actuators than typical robots and possess many degrees of freedom.More specifically, hypermobile robots have redundant joints or links and therefore have more degrees of freedom that the minimum required for locomotion. This redundancy is leads to hypermobility because it allows more flexibility or adaptability for the robot. This greater adaptability is especially useful for robots in uncontrolled environments or confined environments.

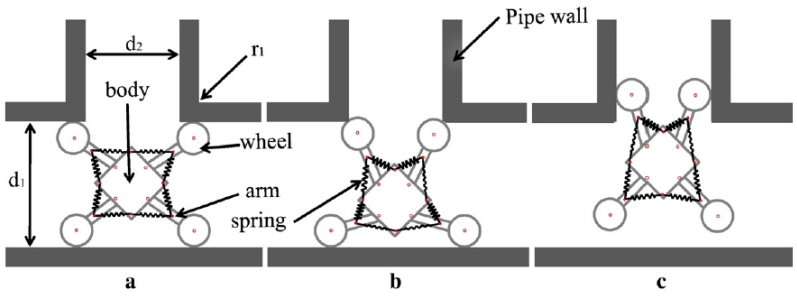

Figure 10: A four wheel type of robot[19]

Hypermobile robots are not a novelty and the first generations of this breed of robot dates to early 1990's. [31]. The main subcategories of hypermobile robots are manipulators [32] and rough or peculiar terrain navigation[31, 33]. The latter being the most popular use of hypermobile robots.

Two designs that are studied are the Explorer [34] and an operator-driven snake-like robot with 4WD-4WS segments [35]. The first one is a multi-body robot designed for pipelines. It has several bodies that have different purposes. Some carry sensors, some electronics and others batteries. The joints between each bodies are articulated, but the wheels on the robot are passive as it is meant to travel in live pipelines. It can be seen on Figure 11.

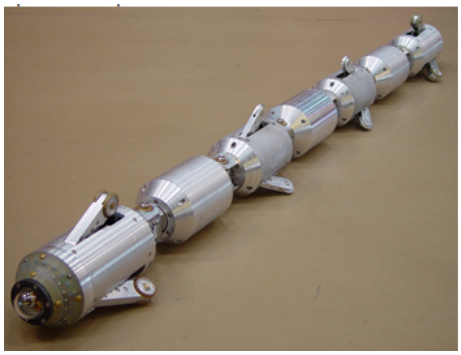

Figure 11: The explorer robot [34]

This concept is akin to a train, where a certain number of wagons drive the vehicle and the others carry important components. It has multiple sets of powered arms and wheels on various bodies for locomotion. However, this design has active wheels and

passive joints. This way, each segment can travel along the same path with more stability [35]. A sketch of the concept is presented on Figure 12.

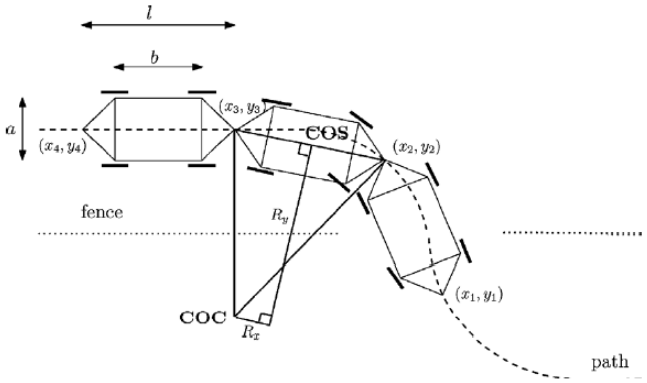

Figure 12: A sketch of a snake-like robot with multiple 4WD-4WS segments[35]

These two types of robots are hypermobile robots, but behave differently. The Explorer on Figure 11 is moved by the fluid in the pipeline it is inspecting. The active joints between each module orient the robot in the pipeline and the arms and wheels are passive and only for support. Therefore this design has the ability to contain various equipment in each module as it is not necessary for each of them to carry locomotion mechanisms.

On the other hand, the design presented on Figure 12 does not require fluid flow for locomotion. It relies on every module's active mechanisms for locomotion. This design can overcome various singularity configurations because of its multiple degrees of freedom. However, it requires more energy to have active mechanisms on every module.

2.3 Hardware

All these different robot architectures rely on more specific mechanisms for different functionalities. Designs of similar purposes will be covered within the same subsection. More specifically, the selected components and their arrangement are explained as well as further comments regarding their efficiency or effectiveness for autonomous pipe inspection.

2.3.1 Driving Mechanisms

In this section, they way a robot converts the electrical energy of its power supply unit into mechanical energy at the wheels is studied. The typical points for evaluation are

the size of the assembly and the efficiency.

Worm Drive at the Wheels A model uses a worm gear to reduce speed from the motor to the driving wheel as shown on Figure 13.

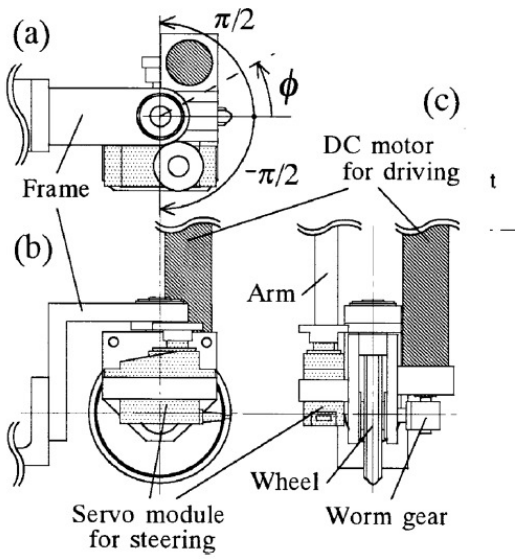

Figure 13: Worm drove at the wheels mechanism [17]

This design benefits from the large reduction ratio of worm drives, therefore this arrangement is very compact, as all systems are fitted on to the wheel directly. Another advantage of this gear reducer is the fact that worm gears cannot be driven from the output, hence the mechanism also acts as a brake. Yet this is achieved at the expense of efficiency as worm drives are typically the least efficient of gear mechanisms.

Centered Worm Drive Another proposed design shows an electric motor aligned on the pipe axis and the output of the shaft is reduced by a worm gear as well as two more gears as seen on Figure 14. The figure shows the central worm ME, transmitting power to gears E and G all the way to wheels D. This drive mechanism is supported by another set of wheels labeled F.

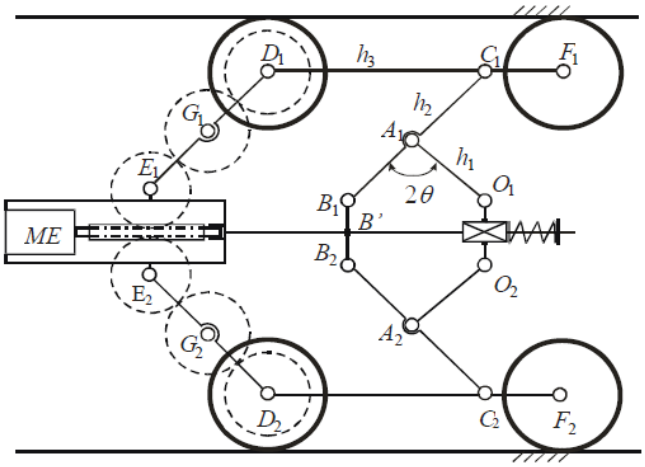

Figure 14: Centered worm drive mechanism [16]

Figure 14 shows that this concept allows an even larger reduction ratio than the previous drive mechanism, but requires to be steered differently. The gearbox is also larger, but is towards the center of the pipe to avoid interference with the pipe wall. Using similar components, it has the same advantages and drawbacks as the previous drive mechanism, it has a large reduction ratio that doubles as a braking system, but is not efficient.

Another driving mechanism found in autonomous mobile robots is the planetary gears with worm drive shown on Figure 15. This design has a worm gear mechanism centered on the pipe axis and other sets of wheels are kept in contact with the pipe wall with a system of planetary gears. Additional guide unit wheels are at the other end of the mechanism to keep it balanced.

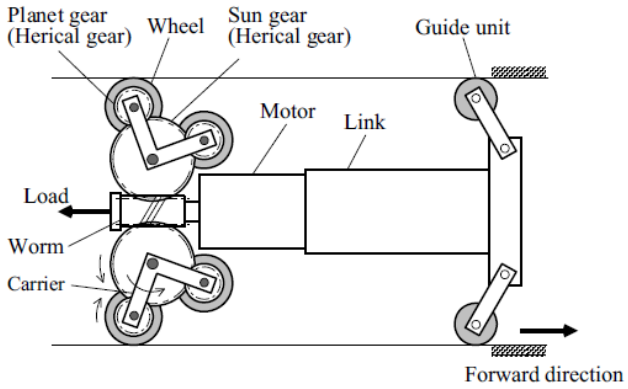

Figure 15: Planetary gears with worm drive mechanism [36]

Planetary Gearbox with Belts Another concept shows a planetary gearbox that drives a pulley. This pulley then drives a bevel gear that is linked to the active wheel by a belt. The concept shown on Figure 16 illustrate the mechanism and labels important components.

This design allows multiple reduction ratios while being quite compact. This design is also centered on the axis in a way that it makes the robot adaptable to various pipe diameters and bends and offers the possibility of having a multi-body robot, which reduces the efficiency of the drivetrain. The major drawbacks to this design are its complexity and the number of parts.

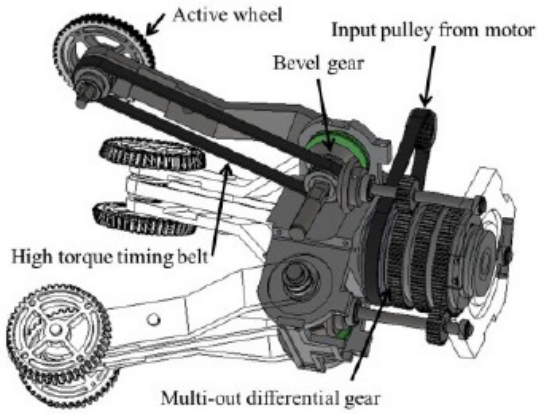

Figure 16: Planetary gearbox with belts mechanism [27]

Quadruple Worm Drive Another concept shows four driving wheels placed evenly around the circumference of the pipe, driven by their independent worm gear and DC motor as seen on Figure 17. While this design seems controllable with its inclination wheels and slider mechanism for diameter adaptation, it is most likely very complex to maneuver correctly. Also, it requires a large number of electronic parts and therefore is likely to necessitate a large housing. This design also uses worm drives and necessitate less energy to maintain active, but has low efficiency. Finally, this model, though bulky, can adapt to some pipe diameter variations and is centered to accommodate other bodies or sensors.

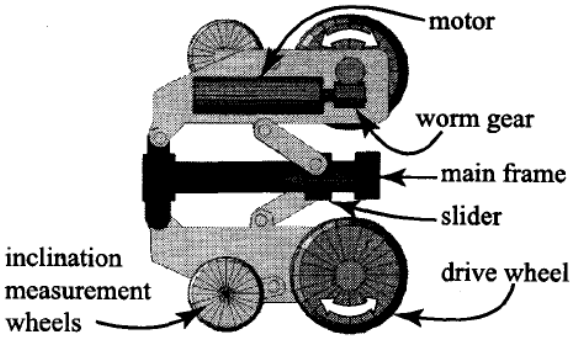

Figure 17: Quadruple worm drive mechanism [37]

Harmonic Drive Harmonic drives are high ratio gear reduction systems. They have mutiple components not present in other drive mechanism and the general components are shown on Figure 18.

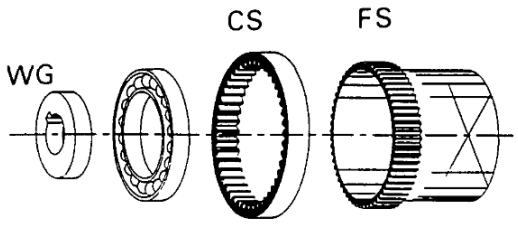

Figure 18: Harmonic drive schematic representation [38]

In typical applications, harmonic drives have an elliptical wave generator (WG) rotating, a fixed circular spline (CS) and an output flexible spline (FS). Therefore tyipcally this kind of drive makes the output gear rotate the equivalent of two teeth while the input wage generator rotate one full turn[38, 39]. Another representation of this drive system is shown on Figure 19 on a more realistic schematic of this mechanism.

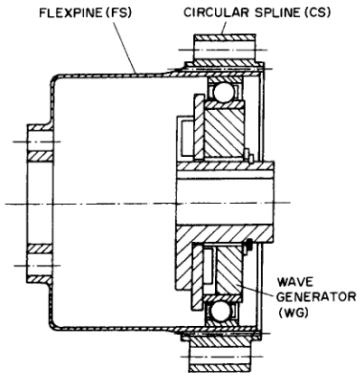

Figure 19: Harmonic drive example mechanism [39]

The main advantages of this kind of drive mechanism is the high possible reduction ratio obtainable. The efficiency of this type of drive isn't constant and can vary. Therefore this mechanism isn't high efficiency. Another advantage of this type of drive though is the low backlash. It has lower backlash than in other types of gear mechanisms, especially worm gear mechanisms, with values of backlash near zero[40, 41].

This type of drive mechanism is assembled coaxially like a planetary gear mechanism, which might prove an advantage in a cylindrical body where space is limited. The high reduction ratios might be a problem however for the use of a harmonic drive in a wheeled driven robot as these ratios might be synonymous with low range of motion. Also, from the literature, harmonic drives seem to be used more frequently in manipulators than mobile robots [38, 39, 40, 41].

2.3.2 Pipe Diameter Adaptation

This section examines multiple methods for reconfiguring the robot geometry to navigate into different pipe diameters and geometries.

Four-Bar Mechanism The mechanism shown in Figure 20 features a scissors like body with a spring between the arms to ensure contact with the walls.

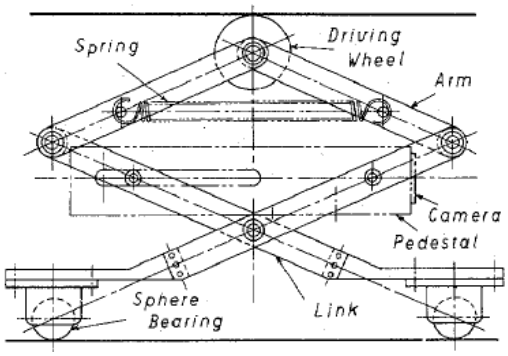

Figure 20: Four-bar mechanism [42]

In this design, a four-bar mechanism allows the extension or retraction of the body of the robot through the use of a contraction spring. The spring brings the linkages closer together in order to maintain contact with the wall of pipes of various diameters. One of the advantages of this model is its simplicity. This design uses passive elements to stay on the pipe wall, so no further energy is required to keep it in position, which is favorable for autonomous robots. This design might not allow precise radial positioning in the pipe due to the mechanical nature of the linkage.

Centered Spring There was also another simpler design that consists of a spring aligned with the axis of the pipe that pushes the driving wheels on the walls as pre-

sented on Figure 21.

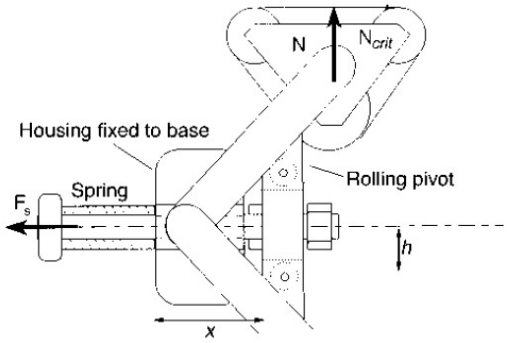

Figure 21: Centered spring mechanism [15]

This design has few components and mechanisms and it makes this design compact and efficient. It also has the advantage of being centered on the pipe axis. However, both arms of the mechanisms are activated simultaneously and could possibly lead to singular configurations due to loss of degrees of freedom.

Screw-Spring Mechanism Another type of spring-based diameter adaptation is presented on Figure 22. This design features adjustable screws that travel along a rod, changing the overall height of the assembly. The bottom springs are actually for suspension and are not actively pushing the bars of the mechanism.

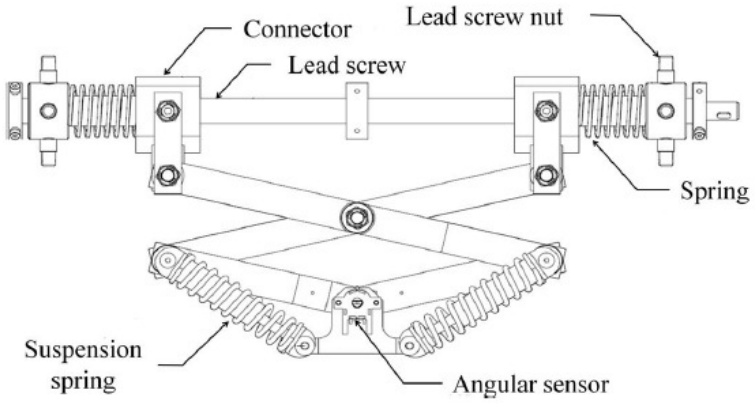

Figure 22: Screw-spring mechanism [43]

This concept combines both previous types of diameter adaptation together. While this idea might be the most precise method, it contains a larger number of parts and is therefore more prone to failure. The large number of parts increases the size of the robot and reduces the space available for electronics.

2.3.3 Performance Comparison

The large majority of autonomous mobile robots are powered by direct current motors and batteries and therefore have a basis for comparison. Various design parameters for this comparison are compiled in Table 2.

Table 2: Description of the variables of the kinematic model

Type of Robot	Speed (cm/s)	Voltage (V)	Torque(mNm)	Power (W)	Mass (g)	Gear Ratio	Dia. Range (mm)
3 Tracked[43]	250	N/A	N/A	N/A	7800	N/A	400-700
3 Wheeled[44]	14	6	30	0.708	189	221:1	90-110
4 Wheeled[36]	1.1	6	50 to 80	N/A	95	N/A	48
Screwdrive[45]	16.3	N/A	N/A	N/A	1800	2:1 or 3:1	175-205
Screwdrive[46]	N/A	9	1402.9	5.625	450	24:1	122-131
3 Tracked[30]	5.5	12	0.741	0.972	266	64:1	80-100
Screwdrive[22]	8	N/A	N/A	N/A	1300	33.2:1	163-173
Screwdrive[22]	10	N/A	N/A	N/A	470	19:1	68-72
Screwdrive[22]	5	N/A	N/A	N/A	480	32:1	68-72
Screwdrive[22]	3	N/A	N/A	N/A	250	84:1	38-43

With data from 10 articles it's impossible to establish a clear trend for most variables. However, Table 2 gives the order of magnitude for multiple variables to start a design. First of all, the speed of most robots fall between 3 and 16.3 cm/s, with the exception of the first 250 cm/s three tracked robot on the first line of Table 2. The discrepancy of this value with respect to the other speeds is probably due to the fact that this design was made to operate in larger pipe sizes as the diameter range column shows.

Torque, voltage and power data have a much wider range of values and are therefore difficult to compare with each other. Also these numbers were not as easily obtained as other categories. Only three or four articles provided them.

Mass data also covered a wide range of values, from 95 to 7800 g. But eight out of ten robots had a mass between 195 and 1800, which is still a wide gap, but gives a better idea of the average mass of the different design. Also, the mass of the different designs seem to correlate with the pipe diameter range they could travel into. This makes sense as a larger robot is necessary for larger pipes and subsequently has more components and a larger mass.

Gear ratio data varied from 2:1 to 221:1, but most values were between 19 and 84 and gave a range of values that seemed to make sense for various robot designs.

2.4 Simulations

Mechanical designs of many kinds go through the planning stage before being fabricated. Electro-mechanical devices like robots are no exceptions and are typically designed with care to ensure proper functionality. However, robots generally behave in a predicted fashion dictated by computer programs and algorithms. These simulations are tools that can validate the design of a robot without the need to go through a building phase and consequently are interesting tools for designers.

2.4.1 Collision Detection

Collision detection algorithms are computer programs that dictate the navigation a robot so that it avoids obstacles and collisions on its path. Collisions are mainly detected or predicted by sensors, but the algorithms used to process the information gathered can vary. Notable examples are dead-lock avoidance schemes [47], look-ahead control [48], iterative linear-quadratic regulator [49], Boundary Following [50] and many others [51],[52], [53]. The main goals of these algorithms is to avoid singularity situations or any configuration or location that the robot would be stuck into and to prove the validity of the design and mathematical model defining the robot.

In many ways, simulations are useful if not essential to robot designs. Especially for confined environments and obstacle ridden paths in mobile robots. In obstacle avoidance path following robots like ”Pekee” from Lapierre et al. [54], simulations are necessary to ensure the design will work in a real environment. In its obstacle avoidance course simulation, the robot shows its ability to escape difficult corner situations and recalculate its route to follow the original path as closely as possible. It is following these simulation results that the researchers can go further and use a real robot in a field experiment.

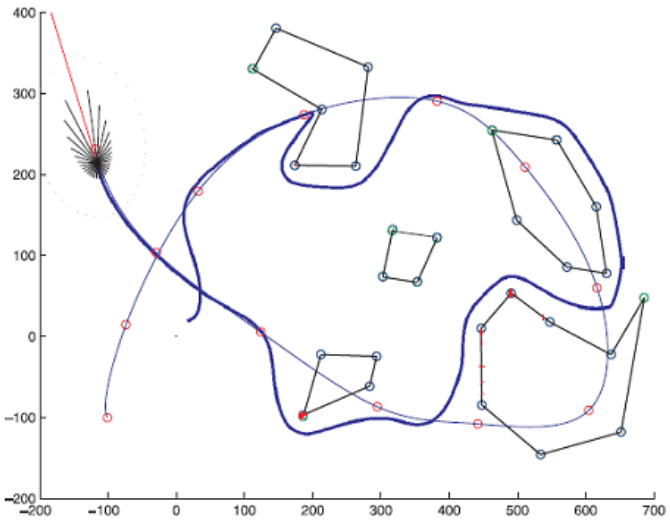

(a) Obstacle course simulation [54]

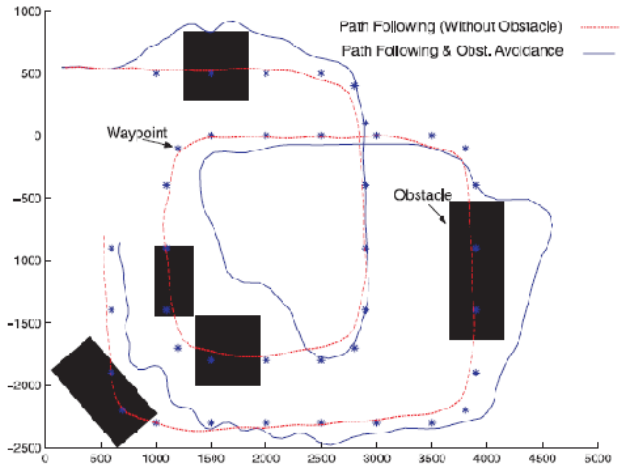

(b) Obstacle course experiment [54]

Figure 23: Obstacle course simulation and real life experiment

In the simulation of Figure 23, the desired path represented as a fine line can be seen going through the obstacles on the course. The actual route of the robot is shown with a bold line and it's possible to see that the robot avoids obstacles to travel to the next waypoint on its course, represented by circles. Then in the real experiment of Figure 23, the robot traveled from waypoint to waypoint while avoiding obstacles like the simulation showed earlier. Therefore simulations are shown to be a good prediction and design tool for researchers.

Simulations are also useful in the process of designing a robot, as parameters in a simulation can be changed to explore various situations. After the development of the mathematical model and the basis of the simulation, it's possible to change some parameters of the environment of the simulation to see the behavior of the robot in such situations. These changes are more rapidly performed and are at a lower cost in a simulation than in a real prototype robot. For instance, changing the shape of an obstacle in a software can be done quickly as opposed to a real obstacle in a laboratory setting. Therefore simulations allow the theoretical validation of more possible scenarios in a given amount of time than real life experiments. This flexibility of using different simulation scenarios to prove the validity of a robot design and mathematical model is demonstrated by Ya Chun Chang et al. [47] in an article where the robot encounters static and dynamic obstacles on its path in a simulation. The simulations prove the worthiness of the model and ensures the robot never collides with an obstacle, as data about collisions are gathered throughout the simulation. These simulations paved the way to a real experiment in which the robot behaved mostly like what was predicted in the simulation.

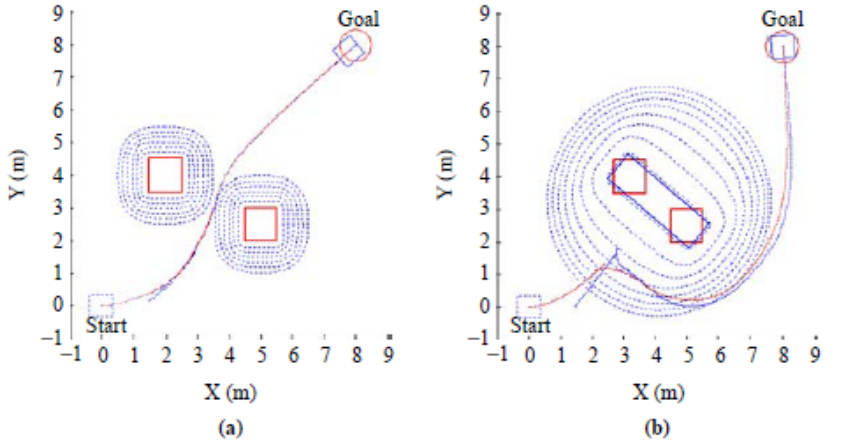

(a) Simulation of two collision scenarios [47]

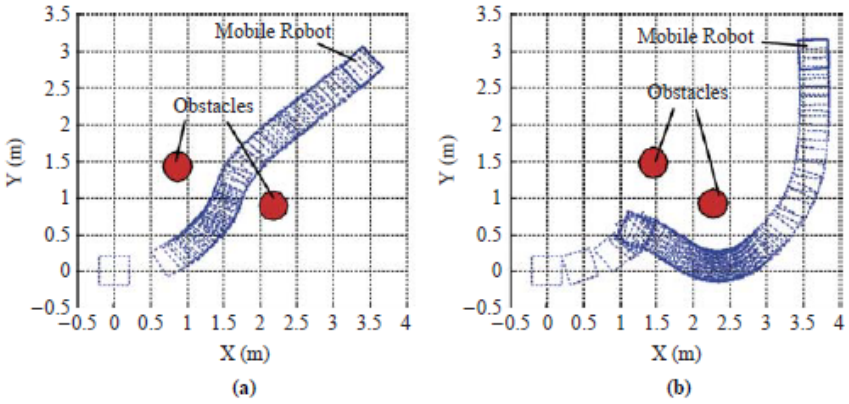

(b) Real experiment of two collision scenarios [47]

Figure 24: Comparison of simulation versus real life experiment

In Figure 24, the actual robot behaved and moved very closely to what what shown on the simulation for both scenarios. Hence, simulations are also tools to predict with exactness the behavior of robotic devices as well as to validate the prototyped design.

2.4.2 Dynamic Multiple Body Simulations

Some simulations involve different parameters than only object detection and path planning and aim their focus towards forces and material resistance to validate the robot's design. The aim of dynamic simulations is to validate the design of a robot, optimize some design parameters and confirm the functionality of all subsystems without going through the process of building the robot. These simulations are a low cost and low delay method of confirming design choices for a given robot.

Dynamic multi-body simulations can validate the solidity of a chosen material in a design or the size of critical components. Some simulations allow the calculation of internal stresses in mechanical assemblies and these tools can therefore be used to confirm the sizing of components or the material selection of a given part [55] or find the maximum load carrying capacity of an assembly [56]. A sample analysis is shown in Vishal et al. [55] shows the resulting stress and deflection in the leg of a walker robot during motion. These results are useful in two ways: First, they confirm the solidity of the part itself and ensure it won't break during use. Second, they show the deflection in the part and this extra precision can be added to the simulation for more accurate simulations if need be. Softwares used for multibody analyses may vary depending on the types of configurations, but for robots, ADAMS[57] is a popular choice [55, 58], but other softwares are sometimes used such as Pro Engineer (CREO) [59, 60] and ANSYS [61, 55].

Simulation algorithms are also as tool to validate the design parameters of the robot itself. Given the inherent simplicity of changing variables in a working simulation, various designs of the same robot can be explored without the need to build one. This way, design parameters of the robot, such as member lengths or joint locations can be optimized for certain tasks [62], [48], [60], [58].

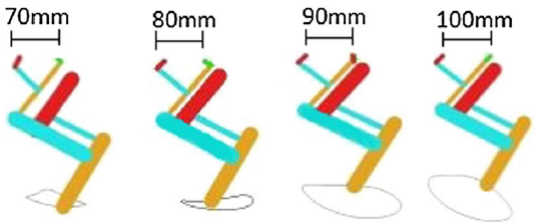

Figure 25: Effect of change of certain design parameters on the behavior of the robot

In Figure 25, the change in position of a joint change the general gait movement of this specific robot leg. Simulations are efficient for optimizing designs as changing some parameters is relatively fast compared to building the part itself and it can help quickly determine the values of design parameters that don't produce any collisions through iterations.

In a similar fashion, design parameters can be tried out and iterated in simulations rapidly to validate design selections such as electric motors and actuators. Also, it's possible to see in real time the impact of changes of certain parameters on path planning and reaction forces in joints [55], [63]. These iterations and changes can be performed directly in the solid generation software such as Pro Engineer [59, 60] or in more general use softwares like Matlab [64, 60].

In conclusion, dynamic simulations and collision detection simulations are economical and reliable tools to study the performances of various metrics on a given robot design. Whether for optimization, collision detection algorithms, design parameter iterative changes and scenarios variety, simulation tools are a necessity for the design of a robot to ensure its functionality and behavior.

2.5 Main Design Model

The development of a robot design for this research has been mainly based on the work of Douadi et al. [65, 66] and Sarfraz [25]. These research documents characterized the metrics of a multi-body snake-like robot for confined environment inspection.

2.5.1 Description

The proposed model in the work of Douadi et al. [66] is a robot for data gathering and exploration in pipeline environments. It shows several bodies of identical size connected by identical revolute joints in between every module. Each body has two arms located at the middle of the robot length on the external sides. Figure 26 shows the configuration of the arms with respect to the body.

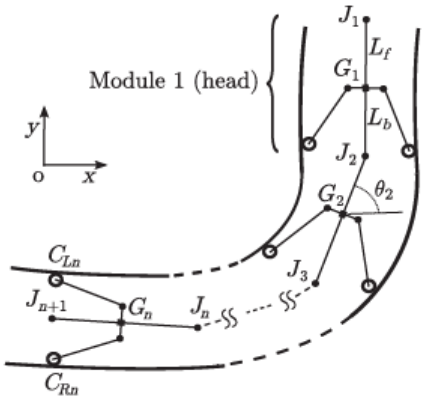

Figure 26: Configuration of the robot proposed by Douadi et al. [66]

Figure 26 shows multiple bodies in a schematic form with arms and wheels located at the end of the arms. The arms are independently moved with active joints to keep contact with the pipe wall and the robot is propelled forward by motors on each wheel.

This design with four active joints on each module has multiple degrees of freedom to provide controllability in confined spaces and ultimately to try to avoid singularity positions during travel. The path of the robot in the pipeline is the pipe's axis and the robot can orient itself in any direction with respect to this axis, given the degrees of freedom it possesses. An angle of 0° being the most obvious position for a robot of this design. This angle value would position the robot directly in line with the pipe axis, making sure the body is the furthest from the wall. The simplified model in two different pipe configuration angles is shown in Figure 27.

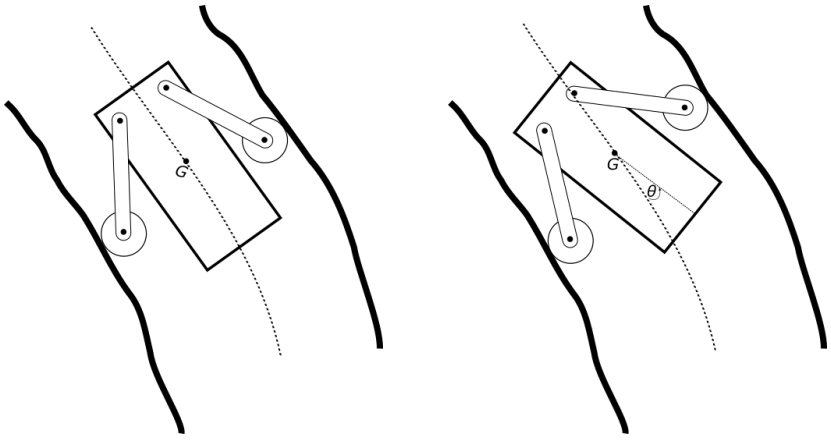

(a) Robot design with a body orientation of 0° with respect to the pipe's axis

(b) Robot design with a body orientation of 30° with respect to the pipe's axis

Figure 27: Robot design in two different orientations in a pipeline

In Figure 27 the robot is shown traveling inside a given pipeline with different orientation angles in order to be able to locate specific defects in the pipe wall or navigate difficult situations. It shows the versatility of the design provided by the extra degrees of freedom from having two arms in the horizontal plane. It only shows one body module however and the complete design includes multiple similar bodies each having their own angles with respect to the pipe's axis.

2.5.2 Design Characterization

The main objectives of these research papers are to prove the controllability of such a model in different pipeline configurations and find the peak values of torque for these pipe route scenarios for the wheel joints and arm joints.

Controllability The controllability of a robot can be proven in various ways through different types of simulations. Finding the dexterity index of the robot during travel is one and has been developed in Douadi et al. [66]. The dexterity index is a value ranging from zero to one that indicates the proximity to a singular position for a given configuration of the robot. This measure of dexterity can be used to prove that the robot has a continuous workspace in which to operate and can therefore travel along its path without entering in a singular configuration and be stuck. The dexterity index of the studied model has been found for different values of arm length and angle of the body with respect to the pipe centerline. The results are presented on Figure 28.

Figure 28 shows the continuous workspace of the robot for a 135° pipe curve for different lengths for the arms. The graph on the left represent the robot's dexterity in-

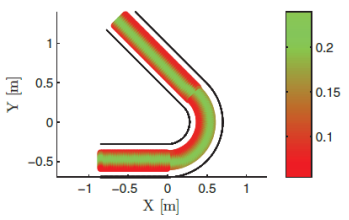

(a) Dexterity index of the robot for different arm lengths with an orientation of 0° with respect to the pipe's axis [66]

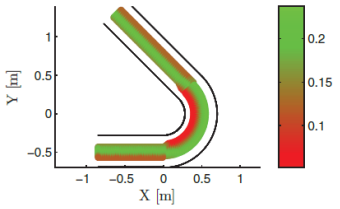

(b) Dexterity index of the robot for different arm lengths with an orientation of 30° with respect to the pipe's axis [66]

Figure 28: Dexterity of the robot for varying arm length in different orientations

dex with its body aligned exactly on the pipe's axis, while the figure on the right shows the dexterity index for the robot with its body aligned at 30° with respect to the pipe axis. The fact that there are no voids or isolated patches in the dexterity index shows that the robot could travel without entering singular configurations for both of these situations. Also it is demonstrated that the robot is furthest from singular positions at the center of the pipeline,which is logical since its body has more room to move close to the center of the pipe.

In the same article, the robot with five modules is shown to move through two different pipe configurations without hindrance while staying mostly on the pipe axis. The simulations are presented on Figure 29.

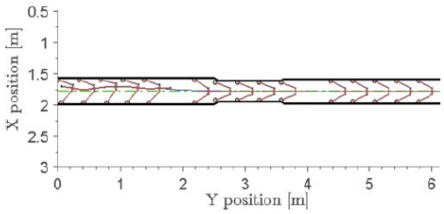

(a) Five module robot in a pipe of changing diameter [66]

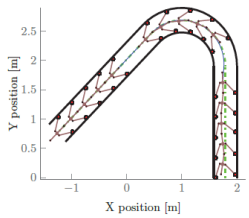

(b) Five module robot in a pipe of bending 135° [66]

Figure 29: Snapshots of the five-module robot in different pipe scenarios

Figure 29 shows that this robot design can navigate inside pipelines of varying diameters and with curvatures of 135° without disturbance and is an additional sign of the controllability of this robot design in a pipe environment.

Joint Torque Peak Values Another article by Douadi et al. [65] presents the dynamics and control of the same type of robot architecture in pipelines. More specifically,

the dynamics of a four-body robot through a pipe of varying cross-section and another pipe with a curvature of 135°. This simulation is similar to the kinematic simulation performed earlier, but the joint torques are calculated during the process with a PID controller. An example graph of the joint torque value gathered is shown on Figure 30.

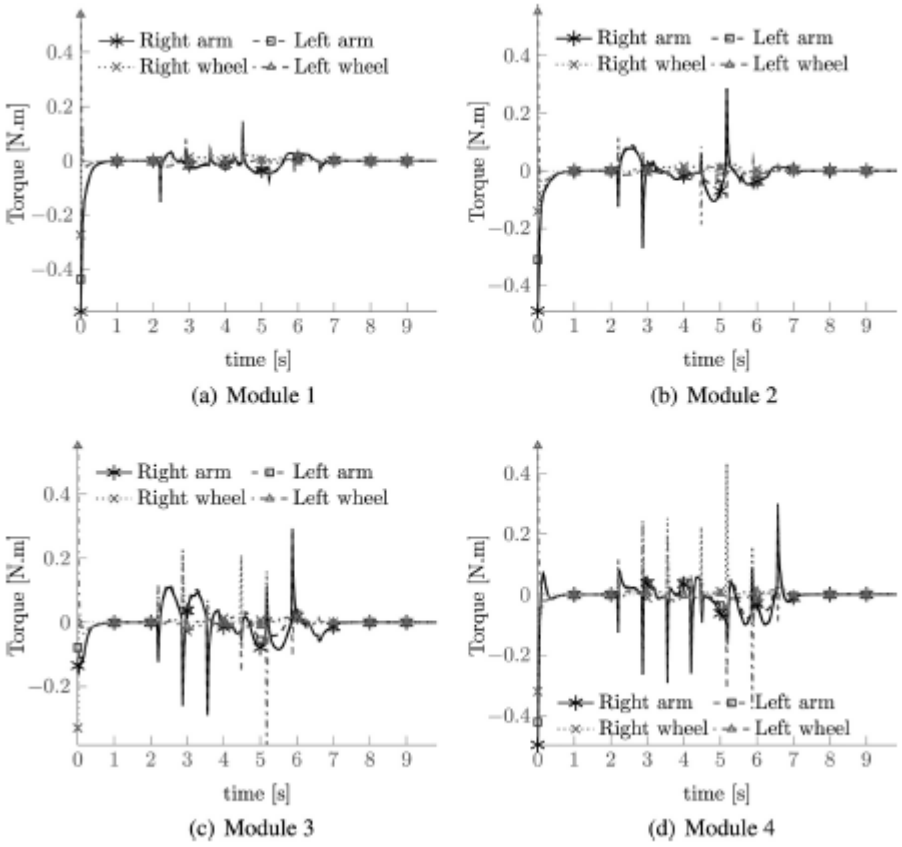

Figure 30: Joint torque calculation for a four-body robot in a 135° elbow pipe [65]

Figure 30 shows the torques for the entire simulation for the 4 active joints of each module. It's then possible to extract the peak values for each joint in order to select motors for the fabrication of the robot. Although these values of torque would only be appropriate for a robot of this exact design, these values range in an order of magnitude possible to reach for small electric motors and suggest that robot of this design could function in reality.

Design Optimization Design parameters for a multibody snake-like inspection robot of the studied design have been optimized in part in the work of Sarfraz [25]. Optimized design variables were the arm lengths, the bodies' length and width as well as the location of the shoulder joints. These parameters have been optimized for maximum achievable workspace in various pipeline environments. An example workspace graph from Sarfraz analysis is shown in Figure 31.

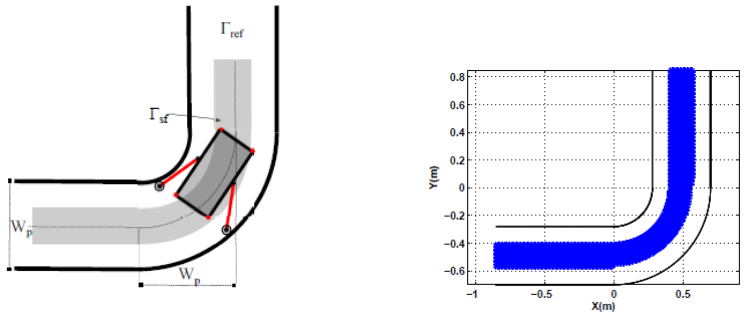

(a) Example workspace determination scenario from Sarfraz [25]

(b) Workspace of the main design in a 90° pipe configuration [25]

Figure 31: Workspace determination in a 90° pipe bend with the body's orientation remaining at 0° with the pipe centerline

These graphs were obtained with the use of a discrete optimization algorithm. This kind of optimization method involves the iterative change of variables and the continuous analysis of the output to determine the best combination of variables for the given design. The same algorithm can be reused in different pipe configuration scenarios and the results can be averaged out to determine the design parameters for all the possible pipe configurations the designed robot has to travel through.

This kind of simulation helps the robot designer choose dimensions and design properties for its robot and also confirms the controllability of the robot at the same time, as a continuous, unbroken workspace for the entire pipe length means the robot stays controllable and free of singularity for the entire time of the simulation. It is another tool to build a working and efficient robot.

Applied Simulation Techniques Combining these various simulation techniques is a way to prove the worthiness of a robot design both on paper and in actuality. They have been used in this work for the proposed design that will be described in the following sections.

First of all, controllability through simulation of the proposed design has been performed. The robot has been simulated traveling through various pipeline configura-

tions, similar to the ones presented in the works of Douadi et al. [65, 66] and Sarfraz [25] to confirm that the proposed design is able to navigate these environments without hindrance while remaining able to accomplish its task of data gathering.

Then, joint torque analyses have been performed on the proposed robot design with varying values for basic design parameters. The information gathered from these analyses has been the groundwork for the selection of motors and components for the robot and to ensure the requirements for these electronic components could be be met. Also, joint torque analyses have been performed to find the values for some design parameters to avoid collisions during navigation. Although this kind of analysis could not exactly pinpoint a specific value for the optimal design parameters, it provided a trend and guideline for further analyses.

Finally, a design optimization algorithm has been developed to find the optimized design parameters. The algorithm used collision detection as a main factor and tried to minimize the number of collision between the robot components and the pipeline while maximizing joint torques and remaining controllable. The same algorithm has been used for various pipe configurations in order to prove the robot is controllable for the entire simulation and that the optimized design variables do not provoke any collision during navigation.

These simulations are a main aspect of this research in order to design a functioning robot and are the object of the next sections.

3 Preliminary Designs

In this section, various ideas and concept for a pipe inspection robot have been explored. They have been the first steps of the design process, which was a significant portion of the work done to reach a conceptual design.

3.1 Hand Sketches

The very first steps in the design was to draw a preliminary version of a robot with the desired design characteristics. As it was mentioned in the previous section, these parameters were the arm length, the body length, the body diameter and the shoulder joint location with respect to the body length. The important ideas at first were to try to fit all the necessary equipment for the robot to navigate and inspect in the same module. By pre-selecting motor size and other important equipment, such as a micro-controller, a rough sketch was obtained. It is shown on Figure 32.

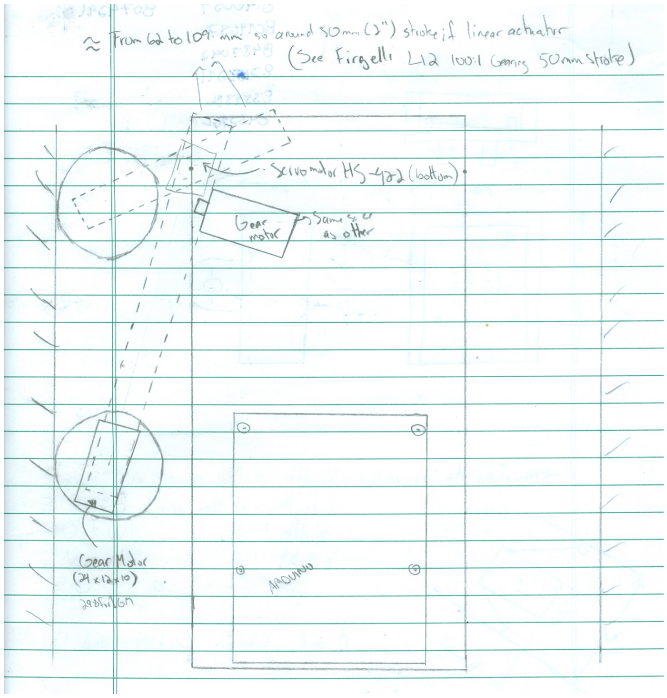

Figure 32: First hand sketch of the design

This design used an arduino as a micro-controller and the lower rectangle in the body of the robot is the actual space an arduino UNO device would take. An arduino UNO was the micro-controller of choice at first because of the relative small size of the device compared to the number of possible connections available on the board. It

was possible to see that it would take almost half the space of the module and therefore this design was not optimal. Also, in this sketch, the servo motors for the arms were pre-selected, but were an order of magnitude too small for was would be required of the robot for navigation and were minimized in this sketch. And the last characteristic of this initial sketch is the fact that the arm length was going to be adjustable in length. The adjustment in length was going to be performed either by a linear actuator or by a rack and pinion mechanism. This latter mechanism is shown on Figure 33.

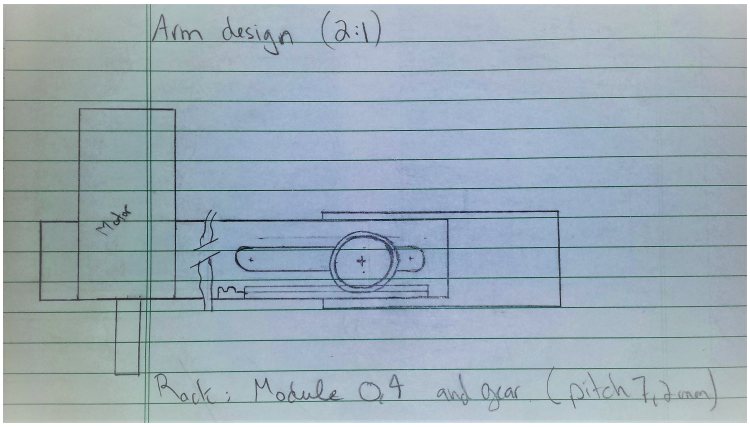

Figure 33: First hand sketch of the design, length adjustment mechanism

The wheel motor on the left of the figure rotates the wheel and this wheel is translated along the arm's length to adjust to the pipe diameter. There would have been a slot in the hollow end of the arm to allow the gear shaft to pass freely while it was driving the end wheel back and forth along the rack and pinion mechanism. The right end of the mechanism would have been were the shoulder servo motors would have connected. This arm extendability was a net benefit when it came to dexterity, especially in pipes of small radius diameter and even sharp bends [25].

However, it became clear in the process of design, that this length adjustment benefit would come at the expense of extra energy consumption and motor space inside the module. Also the required torque on the motor used would cause a selection of a larger motor than what was originally selected and drawn on the sketch. A linear actuator would also be problematic to fit inside the module and would necessitate large energy quantities to maintain activated during navigation. These were the main reasons why this design feature was abandoned early on in the design process. The next idea explored to activate the shoulder joints, with more reasonably sized servo motors was a belt driven mechanism. a sketch of this design idea is shown on Figure 34.

This figure shows the two main servo motors placed at 180° with respect to each other to take up the smallest volume inside the main module. The belt was conceptually

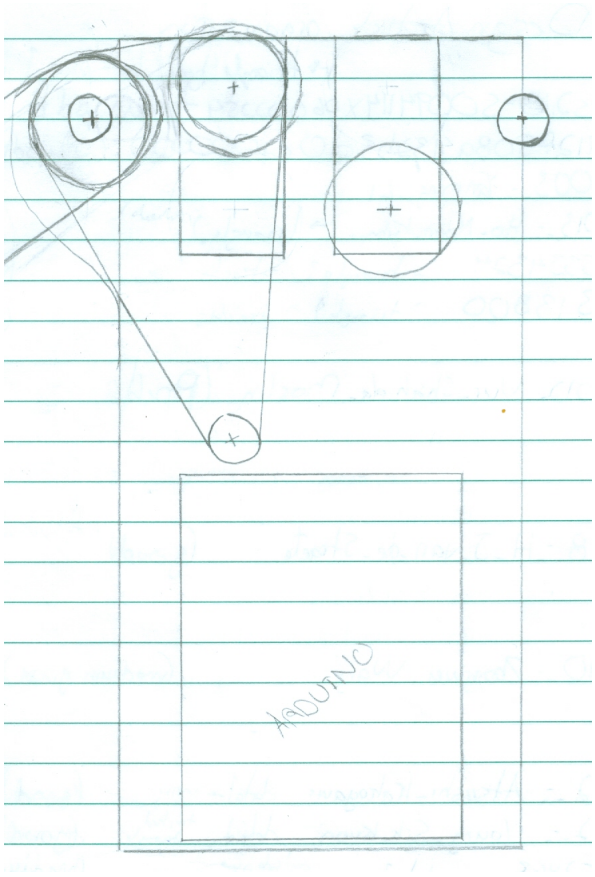

Figure 34: Second hand sketch of the design

going from the servo to the shoulder joint, placed outside the body in this design, passing by another tension pulley placed under the servo motor, next to the micro-controller on the sketch. The advantage of a belt-driven design is the possibility of adjustment of the location of the servo motor or the shoulder joint during the design process as the belt used can be adjusted in length and tension to accommodate design changes when needed. A more specific schematic of the way this belt driven design works is shown on Figure 35.

This design was more thought out and more details of the way the mechanism would have worked were sketched up. In Figure 35 the shaft that transmit power from the belt to the shoulder joint and the arm was designed. The shoulder shaft G took torque from the pulley H that was driven by the belt connect directly to the servo motor. Then the arm F2 is driven by a key in a keyway on the shaft and retaining rings are installed to prevent movement of components axially on the shaft. The lower part of

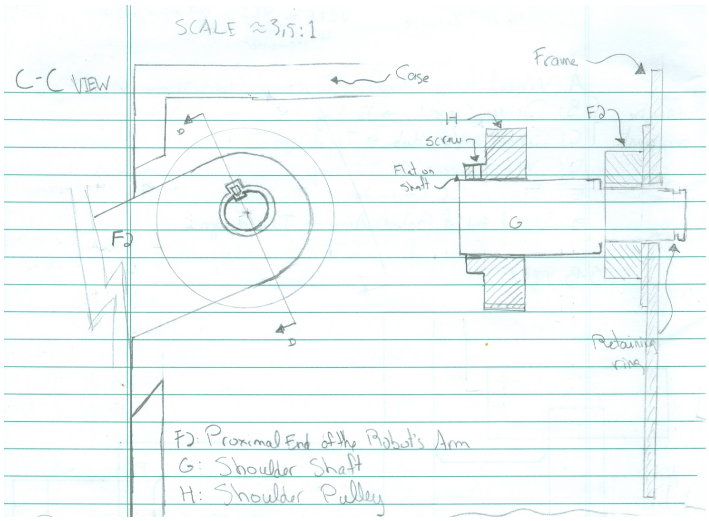

Figure 35: Mechanism of the belt driven mechanism design

the sketch shows an overall view of the casing for this design.

There were still design issues at this stage of the design however. First of all, the necessary amount of servo motors to make navigation possible is four, and the was room for only two servo motors connected via belts to the shoulder joints. Therefore the electronics would have to be moved to another module and this module would be the powered module only and therefore, more volume was available for motors and the necessary driving mechanisms for navigation. Also, the required current to keep the servo motors at a specific angle during navigation was going to be large and this problem would lead to larger, heavier batteries and possibly more modules to carry the same tasks. Another way to provide torque to the shoulder joints was required. More specifically, a passive torque generating device was required to reduce the torque produced from the servo motors. The idea was to use springs to help extend the arms to the outside and apply more contact force on the pipe walls. A general sketch of this idea is presented on Figure 36.

This figure shows how a torsion spring could be added outside the main body of the module to add torque at the shoulder joint represented by a pin on the figure. However, this design idea was flawed for many reasons. First, the torsion spring acting on the arm requires the shoulder joint to be outside the body of the robot. This could potentially lead to problems during navigation, because a protruding section to place a joint could interfere with the pipe in smaller diameter sections or in bends. This was not a problem at this stage, but could be a major one during the simulation phase later. Second, the torsion springs would provide additional torque to help provide better contact force on the pipe walls and therefore traction, but when the robot would navigate in a reducing

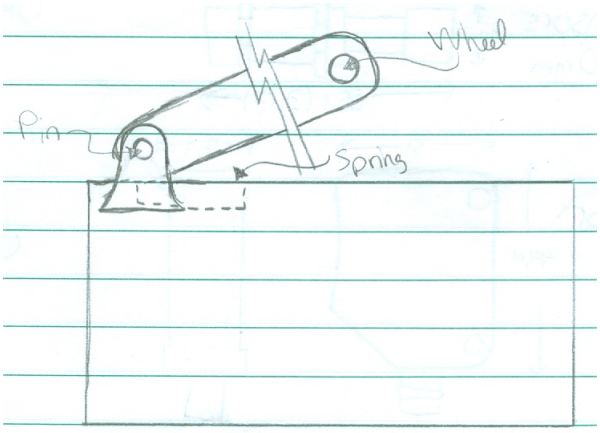

Figure 36: Third hand sketch of the design

diameter section of pipeline, the servo motors would need to act against the springs and therefore would be insufficiently sized for their tasks. Finally, balancing the springs to get even torque on all sides would be a delicate operation as the robot's body needs to be centered on the pipe axis to gather meaningful results from the sensors.

The idea to clear this problematic situation was to use a worm drive mechanism for the shoulder joints. The main advantage of a worm drive mechanism is that is required no energy to maintain at a specific position. The worm drive mechanism cannot be activated from the output and therefore once is placed at the desired position, it doesn't require energy and current to the servo motor to maintain in place. At this moment, with the major problems of space and torque requirements relatively under control, the next steps were to go from paper to computer generated design.

3.2 Conceptual Designs

The first computer assited drawing made was from the design stage shown in Figure 33. At this stage, the design was at a rough step of the process. The overall shape of the robot was defined, but the details weren't clear. The design is shown on Figure 37.

This image shows the main ideas developed for the robot for the architecture of the robot. Two bodies are there with different functions, the front body is the powered module with the motors and the arms. The second module carries the sensors. The two bodies are connected by a passive joint. The passive joint in this design actually had three joints that provided rotation around different axes. The arm design was short and had a large motor. Two arms were powered and two others were spring loaded to the pipe wall. This design was a compromise to compensate for the lack of space for four servo motors.

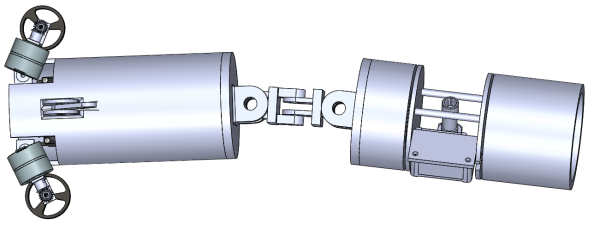

Figure 37: Assembly of the first CAD model

The powered module at the front of the assembly was developed in more details however, and images were gathered. The interior of the front powered module is shown on Figure 38

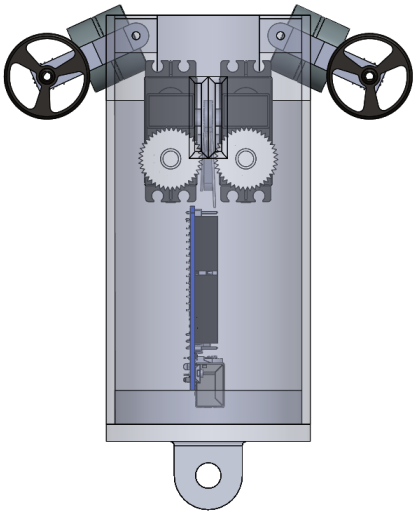

Figure 38: Inside of the first CAD model powered module

It's possible to see on this figure that including the electronics in the same module as the servo motors would be a difficult task. This constraint brought forward the concept of belt driven shoulder joints in order to relocate the servo motors and be able to control and adjust the location of the shoulder joint. The CAD model representing the hand sketch of Figure 34 is shown hereafter in Figure 39.

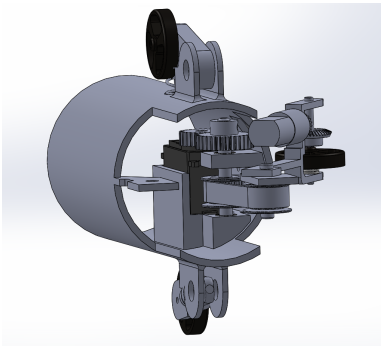

(a) Belt driven CAD design overview

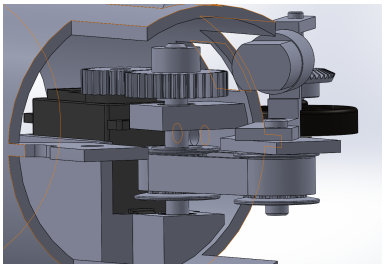

(b) Belt driven CAD design close up view of the mechanism

Figure 39: Second CAD design using a belt driven mechanism

This figure shows the belt driven mechanism for the shoulder joint of the robot that was previously hand sketched in Figure 35. This designed used gears to transmit torque from the servo motor to a shaft that then transmits torque through a pulley and belt mechanism to the arm. The servo motor shown in this figure in enclosed in a box to secure it and the shafts used to transmit torque and are integrated to the body of the robot. This design also incorporated spring loaded mechanisms to support the other two arms of the powered module. The mechanism is shown in Figure 40 along with another type of spring mechanism imagined possible for this design.

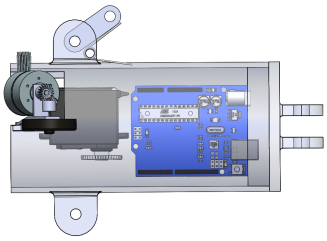

(a) Spring loaded arm CAD design number 1

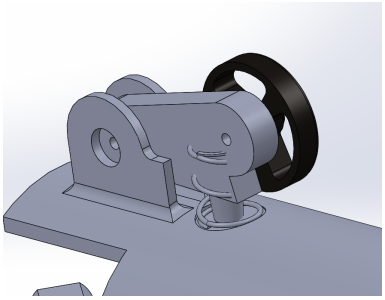

(b) Spring loaded arm CAD design number 2

Figure 40: Spring loaded mechanisms for the support arms of the powered module

These design show two different ways to used the potential energy of springs to help the support wheels stay in contact with the pipe walls at all times. Figure 40a uses a torsion spring between the arm and the outside body of the robot. This spring has an axis of rotation on the protruding support flange for the wheel and extends the

arm. Figure 40b on the other hand shows a linear spring with an encased support on the outside body of the robot and pushing on the arm to extend it. These two designs proved not to be interesting as it was mentioned in the previous section and were removed from the design to include 2 other servo motors inside the body and moving the electronics in another module. At this point, the design looked like what is shown on Figure 41.

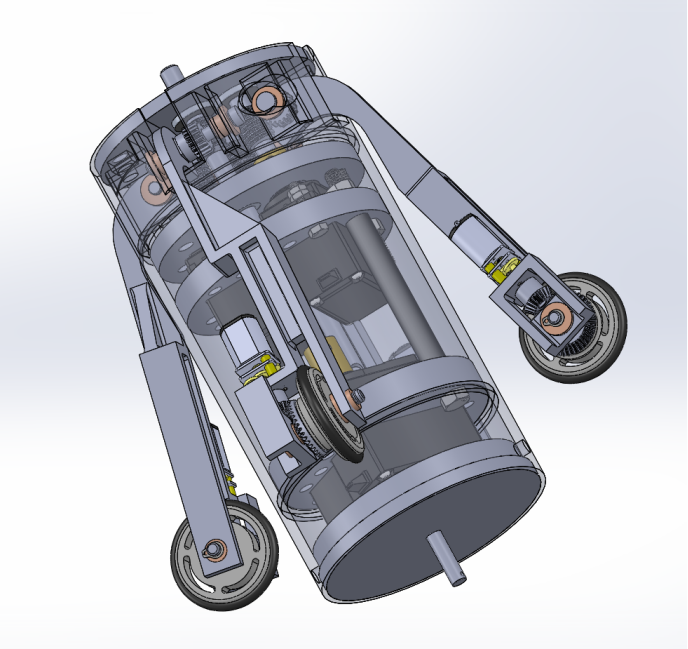

Figure 41: First CAD design with four servo motors and no electronics or springs

This design is the first design to include the four required servo motors inside the body and that has no electronics. This design is the one that has been progressively updated and tweaked to reach the final design. The work on this design is what confirmed the possibility of the conceptual idea for this robot. It is this design process that allowed the project to transfer from the drawing board to an actual prototype. This design has the required mechanical requirements to navigate in a pipeline, carry other modules for sensors, batteries, electronics and other such components and can be adjusted for optimal values of positions of joints after simulation for most efficient navigation in a pipeline.

4 Proposed Design

In this section, the major design guidelines of the design will be explored and explained. Two articles in particular are the main drivers for this research. They are presented in Douadi $et\ al.$ [65, 66]. This two-dimensional model consists of multiple similar bodies connected with passive joints as shown on Figure 42.

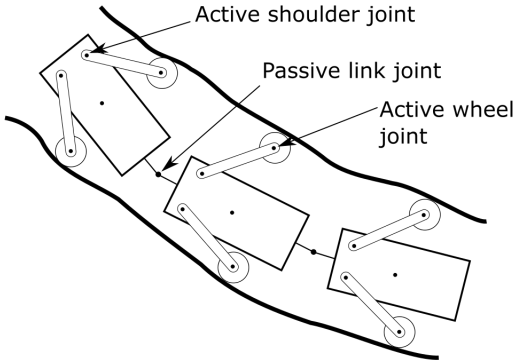

Figure 42: General architecture of the designed robot

All the bodies, arms and wheels are the same dimensions. Each body has a set of driven wheels at the end of each arm. These arms are also powered by active shoulder joints toward the front of each body. All bodies are linked by a passive joint that allows each body to rotate.

Most of the pipelines in Canada are of diameters between half an inch and six inches according to the Canadian Energy Pipeline Association [67]. Smaller pipes are typically less inspected since most existing robots are large in size and cannot travel in such pipes[3, 68].

Also, robots traveling in smaller pipelines have a greater probability of encountering a singularity position because of the confined environment that a small diameter pipeline is. Moreover, since internal corrosion is a common type of defect[69], less dexterous robots can have difficulty traveling in more rugged and corroded internal pipes.

This design is suitable for small pipe inspection for many reasons. A multi-joint robot can overcome singularity positions by having numerous powered bodies. If one body enters a singularity configuration at some point, it can still be moved by the other bodies to get out of this position. However, this dexterity has the drawback of having redundant modules and therefore multiple components and bodies.

Therefore, the proposed design for small diameter pipe inspection is a small mobile robot with multiple bodies, linked by passive joints. It has active shoulder joints and wheels and has four arms on every powered module. These modules, or bodies, carry out different tasks and are described in the following sections.

The presented model is a hypermobile robot with multiple bodies with various functions, but is propelled by active wheels and the joints between each segment is passive. Hypermobility means having a greater amount of active joints than necessary for navigation. The extra energy required by the active joints is justified nonetheless for the added adaptability of hypermobile robots. A sketch of the modules with their main components and function is pictured in Figure 43.

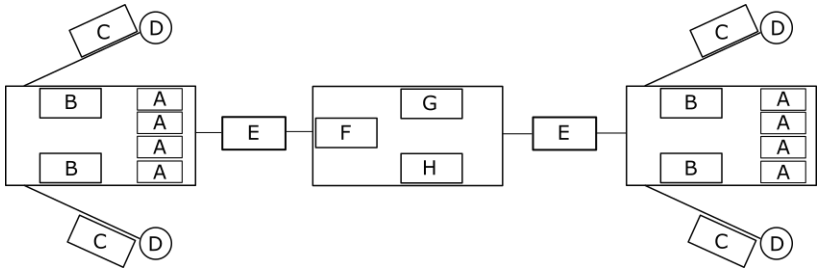

Figure 43: The proposed architecture for the robot

Labels from Figure 43 are detailed in Table 3.

Table 3: Proposed design component label descriptions

Label	**Representation**
A	Servo motor
B	Worm and worm gear mechanism
C	Gear motor
D	Wheel
E	Universal joint
F	Motor
G	Laser sensor
H	Ultrasonic sensor

The novelty in this design is that every odd numbered segment is a powered module with four active arm joints and wheels at 90°. Also, every even numbered segment is passive, has no wheels and carries essential components as batteries, controllers or sensors. The term passive here implies that these modules have no part in the navigation of the robot. The energetic contribution for traveling inside the pipeline is entirely

performed by active modules. Finally, every link between the segments is passive. All the modules' overall dimensions are equal and the arm length and wheel radius of each powered module are also the same.

The mains reasons for such ideas are that the proposed design will most likely be more adaptable and less subject to singularity configurations in a confined pipe environment while remaining centered on the pipe centerline for the sensors. It also allows each segment to follow the same path, in this case, the centerline of the pipe. Moreover, it would be possible to change the final number of modules depending on the desired options on the robot. For instance, the robot could have a minimal amount of modules to maximize its autonomy, or it could carry a vast array of sensor on multiple modules to get a better resolution of the pipeline. The details of the content and the tasks performed by each segment, or module, will be explained hereafter.

4.1 Powered Module

This module contains the drive mechanisms. This module could be compacted down to a minimal size that would go along the optimal dimensions proposed by Sarfraz [25].

4.1.1 Geometry

The most important design guidelines for this module are that all necessary motors as well as their speed reduction mechanisms should be on this module and that the joint of the four arms should be at the same distance from the front of the module. Moreover, these components should all fit within a body of optimal dimensions as described by Sarfraz [25]. On the other hand, these optimal dimensions do not consider every aspect of the robot's mechanisms and the placement of some crucial elements are neglected. These dimensions include the distance between the shoulder joints, the size of the wheels and the length of the linkage between the modules. A methodology to find the values for these dimensions that won't provoke any collision during travel will be discussed in the following section.

4.1.2 Robot Planar Model

The planar model of the robot has the body center aligned on the pipe's centerline and has two front arms, each carrying a driven wheel, as it is presented on Figure 44.

It was shown that some dimensions could be optimized for a multiple-body robot like the one presented by Douadi $et\ al.$ [65, 66]. More specifically, the optimal dimensions for the four main geometric variables of the model. These geometric variables are the arms' length l, the body's height h, the body's width w and the arm shoulder's location a in terms of the pipe diameter.

Since the pipe sizes that the robot will drive into are known, it's possible to have basic global dimensions for designing. For a smallest pipe diameter of 6in, the main

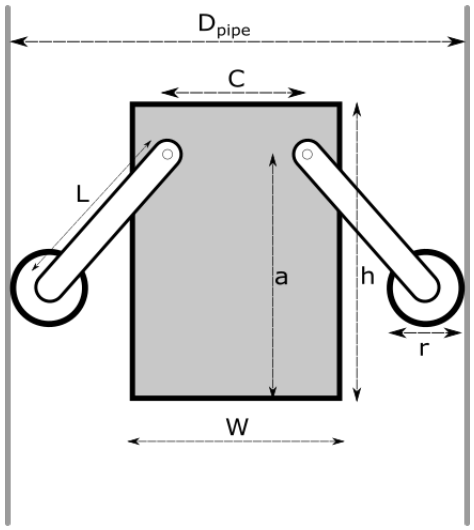

Figure 44: Kinematic model of the proposed robot

design variables for the planar model are shown in Table 4.

Table 4: Global optimal design parameters

Variable	**Parametric Value**	**Value** (in)
w	0.5 ϕ	3
h	1 ϕ	6
l	0.75 ϕ	4.5
a	0.9 ϕ	5.4

The values shown in Table 4 are optimal for pipes of 6 in in diameter. However, with a robot designed to navigate in pipes of diameters varying from 6 to 8 in, the parametric value cannot change to adapt to the diameter during use. Therefore, the use of the most critical, worst case scenario for navigation, the smaller 6 in pipe diameter, will be considered for the design parameter values.

These values will be used as global references in the design of the robot's main features. Moreover, values for C, r will be optimized in the following sections and will be used in the design. The length of the linkage between each module will also be optimized and will be used in the final design as well.

4.1.3 Shoulder Motor Selection

In this section the bare minimum requirements as well as worst case scenario calculations for the sizing of various electronic and mechanical parts will be performed. The calculations are for independently calculating the stall torque for the shoulder joint motors and ensuring they can deliver the necessary amount of torque to make sure there is no slippage of the robot and that they can reach the required angular values during navigation.

First and foremost, it is known that this joint will require high torque and little angular displacement. Therefore a servo motor could be used for this application since these motors are known for their high torque capabilities. The shoulder joint is the one shown on Figure 45.

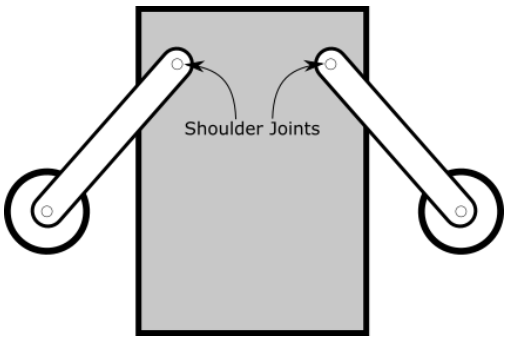

Figure 45: Location of the shoulder joints

The servo motor has to be used with a worm drive gearbox. The major advantage of the worm drive is the lower required amount of energy to maintain the motor in place due to the worm drive self-locking capability. Therefore, the motors draw less current and the batteries can potentially last longer.

There are many important data when it comes to choose the right servo motor. There is the operating voltage range, the torque, the dimensions, etc. But, one of the most important criterion is the stall torque. This value represents the torque applied to the device so that its rotational speed becomes zero. This gives an idea of the maximum torque available from the motor. Also, there are some peak torque values [65] for this joint for a similar robot in a similar situation. The peak value obtained is 0.3131 Nm, which corresponds to 46.10 $oz - in$.

Gearbox Calculations The servo motor is connected to a worm drive with a reduction of 1:10 (See Appendix A for more details). The minimum servo torque can be found from:

$$\tau_{min} \quad = \quad \tau_{peak_{servo}} * \frac{1}{n_{worm}} * \frac{1}{\eta_{worm}} * SF$$

Assuming an efficiency n_{worm} of 0.5 and including a safety factor SF of 2, the minimum servo torque is 0.125N.

Angle Limitation Typical servo motors have working angles of 90 or 180 degrees. Since the minimum working angle of 9.5 degrees is require to move the robot in the pipe environment (see Appendix B), the servo has to move 95 degrees with the 1:10 worm drive. The HS-422 from Hi-Tec was chosen as it has a stall torque of 0.4 Nm at 6V and a working angle of 180 degrees.

4.1.4 Wheel Motor Selection

Similarly to the shoulder motor selection subsection, the calculations performed in this section are preliminary calculations to ensure the selected motors are fit to carry the robot in the worst possible conditions in pipeline navigation. They are performed independently in this preliminary design sizing section assuming the shoulder joints provide the necessary torque to avoid slippage in the worst case scenarios. Further calculations are performed in later sections to ensure the combined selection of motors are correct and sized correctly to navigate in the worst possible pipe scenarios.

The selection of the wheel motors is based on two main characteristics: speed and torque. Also, the limited housing space for the motor and each arm will restrict the choice of motor available. The location of the wheel joints are shown on Figure 46.

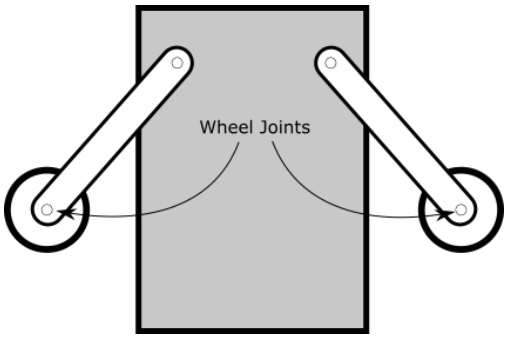

Figure 46: Location of the wheel joints

Also, because of the way the motor will be placed relative to the wheel, the output shaft has to be reoriented by 90°. Therefore a one stage reduction set of bevel gears with a reduction ratio of two is used. A ratio of two was chosen because the highest

ratio was advantageous for the robot, but a ratio higher than two required bevel gears of very different sizes that could not possibly fit in the restricted volume they could occupy. The minimal required torque to move the robot has to be calculated. The peak torque, the reduction ratio of the bevel gears and their efficiency are needed for the calculation.

$$\tau_{min} \quad = \quad \tau_{peak_{dcmotor}} * \frac{1}{n_{bevel}} * \frac{1}{\eta_{bevel}}$$

The bevel gear ratio is 1:2 and the bevel gears efficiency is 0.98. The peak torque required can be estimated in two different ways. First, it can be estimated from a similar robot in similar situations[65] to be about 0.46Nm. However it can also be estimated by calculations. The diagram for the estimation is shown on Figure 47.

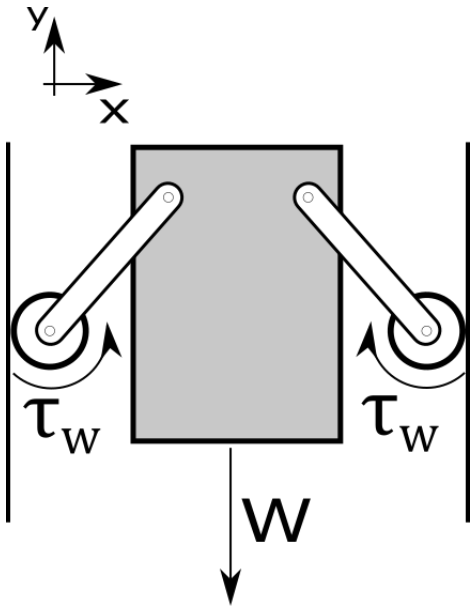

Figure 47: Diagram for peak torque calculation

Assuming the arms are pushed to the wall with sufficient force to avoid slip, the required torque at each wheel, τ_W, is the minimum torque required to keep the robot's powered module centered on the pipe axis and keep its orientation parallel to the pipeline. To keep the cylindrical body of the robot concentric with the pipeline. Summing the forces in the vertical y direction, the following equations can be obtained:

$$\begin{aligned} \sum F_y &= 0 \\ \frac{2\tau_{wheel}}{r} - W &= 0 \\ \tau_{wheel} &= \frac{rmg}{2} \end{aligned}$$

Knowing the value of g to be 9.81 m/s^2, the maximum value possible for r is 0.025m (see section 4.1.5), the only parameter left to estimate is the mass of the robot. The robot powered module is estimated to be 2 kg. It is a rough estimation of mass and it can be reevaluated when the robot is fabricated to ensure this mass is reasonable. The minimum required torque is calculated to be 0.245 Nm.

Since the estimated value of 0.46Nm is greater, the peak torque is evaluated at 0.46Nm. Which means the minimal torque for the gear motor selected is 0.2347 Nm.

Knowing the minimum value of torque necessary for the robot to function, a choice has to be made that has a value at least the calculated minimum, but as small as possible considering that smaller values of torque will generally yield higher speed outputs, which is also preferable here. Having the most important value for the selection, a choice can be made: The ServoCity 90 RPM Micro gearmotor. The most important values from the manufacturers data sheet are presented in Table 5.

Table 5: Data from the gearmotor's manufacturer

Variable	**Value (@6V)**	**Value (@12V)**
$speed$	45 rpm	90 rpm
$stall\ torque$	0.28 Nm	0.49 Nm
$reduction\ ratio$	298:1	298:1

The motor is meant to be run at 6V in the robot design as other components will most likely be running on 6V, but since the motor can handle 12V input voltage, then the data for both voltages are shown.

4.1.5 Joint Placement Impact on Motor Selection

The values presented in the last section are valid values for global parameter optimization of the robot in theory, but they do not account for joints' location. In order to be mechanically able to move, the robot requires some articulated joints. The general layout of the most important joints of the robot moving forward in a vertical pipe is presented in detail on Figure 48.

General Equations From Figure 48, it's possible to get a closure equation for the robot since both wheels must stay in contact with the walls.

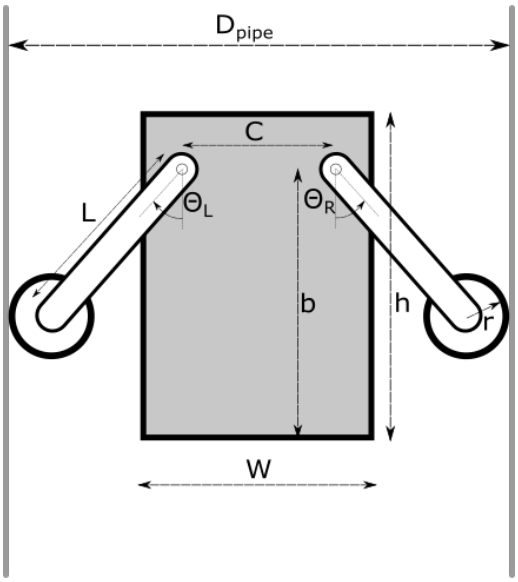

Figure 48: Sketch of the powered module with important design variables

$$r + Lsin(\theta_L) + C + Lsin(\theta_R) + r = D_{pipe} \tag{10}$$

Also, knowing that both angles θ_L and θ_R are equal at all times for straight pipes, the equation can be simplified.

$$2r + 2Lsin(\theta) + C = D_{pipe} \tag{11}$$

Isolating the left wheel in a free body diagram in Figure 49, it is possible to obtain the wheel torque t_{wheel} assuming a constant robot speed.

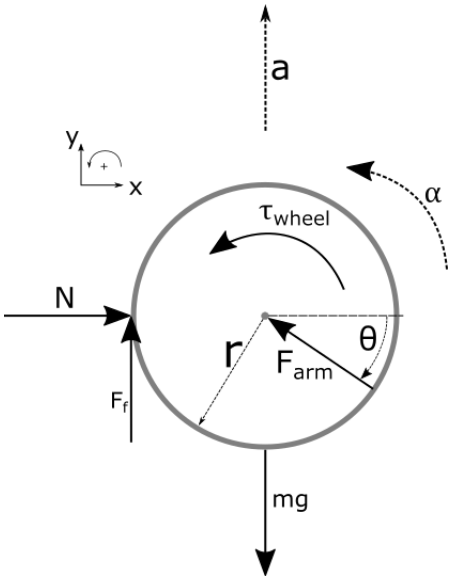

Figure 49: Powered module sample wheel free body diagram

From this figure it's possible to use the following equations for constant speeds:

$$\begin{aligned} \sum F_x &= 0 \\ \sum M_O &= 0 \end{aligned}$$

From which we get:

$$N - F_{arm} cos(\theta) = 0 \quad (12)$$

$$\tau_{wheel} - F_f \cdot r = 0 \quad (13)$$

Also knowing that $F_f = \mu N$, equation 13 can be rewritten as follows:

$$\tau_{wheel} = \mu N r \quad (14)$$

Minimum Required Normal Force The robot must resist slipping when traveling inside a pipeline, therefore a minimum friction force is necessary (See appendix A for more details). In the free body diagram of Figure 49, the friction force F_f is assumed

in the upward direction assuming the wheel rolls up the pipe without slip. This is only true if the following condition is fulfilled:

$$\tau_{wheel} \leq \mu N r \tag{15}$$

Since most variables are still unknowns at this point, this condition will be checked later.

The other free body diagram that is possible to extract from Figure 48 is the one from the left arm on the image. It is shown on Figure 50.

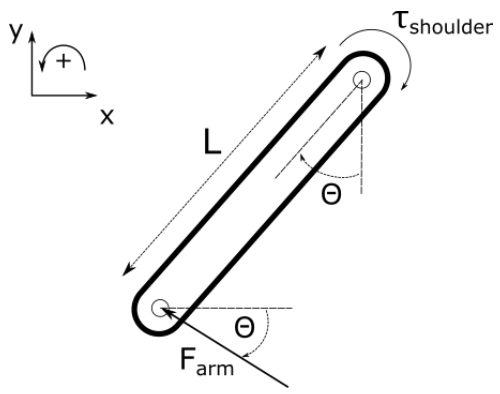

Figure 50: Powered module sample arm free body diagram

From this diagram, the resulting equation is the following:

$$\sum M_O = 0 \tag{16}$$

$$\sum M_O = \tau_{shoulder} - F_{arm} \cdot L \tag{17}$$

$$F_{arm} = \frac{\tau_{shoulder}}{L} \tag{18}$$

Therefore, the new set of equations taken from equations 11,12,15 and 18 is the following:

$$N = \frac{\tau_{shoulder}}{L} cos(\theta) \tag{19}$$

$$2r + 2Lsin(\theta) + C = D_{pipe} \tag{20}$$

$$\tau_{wheel} \leq \mu N r \tag{21}$$

Knowing the values of $\tau_{shoulder}$, L, D_{pipe}, τ_{wheel}, and μ, there are four unknowns left. μ is chosen to be 0.4, which is a conservative value for a coefficient of friction between rubber and steel [70]. In this case a conservative value of the coefficient of

friction from the data between rubber and steel is taken as no reliable data was found on the coefficient of friction between wet steel and rubber was found. Experiments would have to be performed to determine a value for the lowest possible coefficient of friction between rubber and wet steel in a pipeline. These calculations would certainly need to be revised with an accurate coefficient. Also, the value of slippage is estimated considering constant speeds and various values of acceleration and speed could factor importantly in the calculation of slippage and should be included in a more thorough analysis of the slip condition during future work.

The values of r and C will vary from the minima and maxima shown below. Then, using equation 11, the value of θ for the entire range of r and C can be calculated as well as N.

$$\begin{aligned} r_{min} &= 0.005 \\ r_{max} &= 0.025 \\ C_{min} &= 0.015 \\ C_{max} &= 0.060 \end{aligned}$$

The values of θ and N with varying values of r and C are given on Figure 51

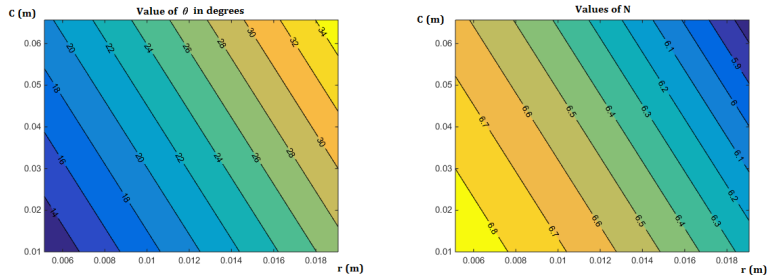

(a) Arm angle for varying values of wheel radius and shoulder width

(b) Normal force for varying values of wheel radius and shoulder width

Figure 51: Values of θ and N for the entire range of r and C

Knowing values of N for all combinations of r and C, it's possible to verify equation 15 for the same range of values of wheel radius and shoulder width since τ_{wheel} doesn't change. The ratio of $\tau_{wheel}/(\mu N r)$ will be calculated and if the result is smaller than 1, then the assumption that the wheels do not slip will stand as correct. Results are shown on Figure 52.

As it is possible to see on Figure 52, the ratios for any configuration is higher than 1, therefore the wheel would slip and not roll in the previous scenario. At this point,

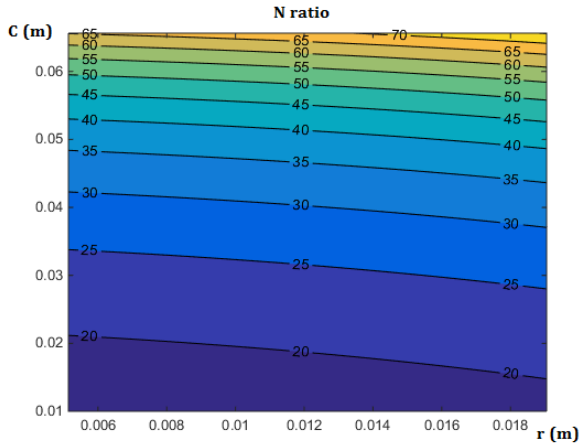

Figure 52: Ratio of wheel torque over maximum allowable traction force

there is a contradiction that needs to be resolved to progress further. The necessary torque according to a simulation by Douadi $et\ al.$ [65] mentions torque values of up to 0.46 Nm for the wheel joint, but a model of the robot shows that reaching this value of torque would provoke slip instead of rolling for the wheel. This is actually a dilemma where both sides can't be satisfied concurrently.

A possible reason for this unsolvable situation is that the estimated values of torque are too large. Alternatively, other design parameters could have been estimated erroneously. However, the ratio of $\tau_{wheel}/(\mu N r)$ has to be lower than 1 to avoid slipping of the wheels. Therefore, another wheel motor is selected.

The 4900 RPM Micro gear motor from $ServoCity$ with it's 0.014 Nm of torque is selected. Since no values of normal force N change with respect to the wheel motor, the ratio of $\tau_{wheel}/(\mu N r)$ can be recomputed to make sure the slipping condition can be avoided.

Figure 53 illustrates the ratio of $\tau_{wheel}/(\mu N r)$ using another servo motor with lower torque. The ratio computed can be lower than 1 for the entire range of r and values of C smaller than 0.45 m approximately. Therefore, the wheels would not slip.

Knowing the most important components for the robot, the design and determination of other design parameters can be performed, such as the values of r and C. The most extreme scenarios for these two parameters are represented on Figure 54.

Figures 52, 53 and 54 illustrate that larger values of r and C are mechanically advantageous to maximize the torque exerted by the shoulder joints motors. Therefore, larger values of r and C minimize the effort required by the shoulder motor. However,

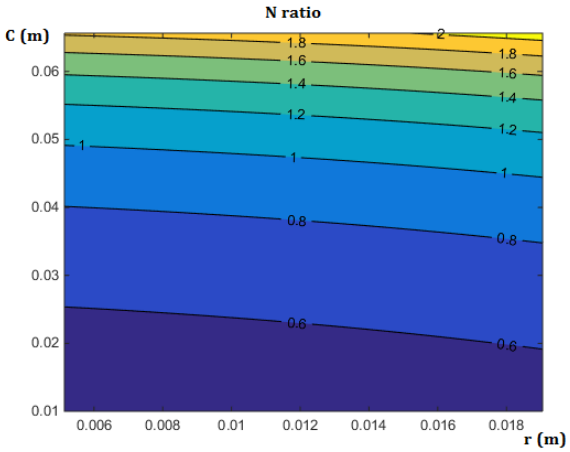

Figure 53: Ratio of wheel torque over maximum allowable traction force after motor change

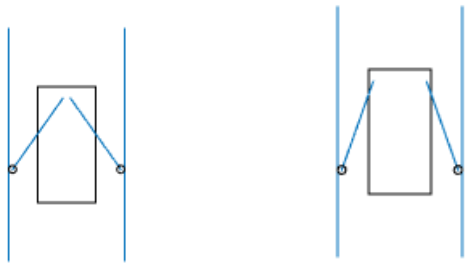

(a) Minimal C and minimal r

(b) Maximal C and minimal r

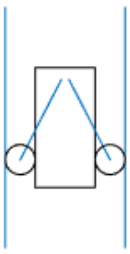

(c) Minimal C and maximal r

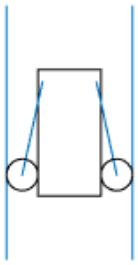

(d) Maximal C and maximal r

Figure 54: Four extreme possible configurations for the robot

the maximal theoretical values might not be physically achievable because of lack of space or interference with other components in certain situations. The values of r vary from the minimal value of 0.005m that would be large enough to allow the robot to move without causing interference between the wheel mechanisms and other components and the maximum r value of 0.025m that would be the largest wheel diameter to avoid interference between the wheels and the body. The values of C vary from 0.015m and 0.060m that are the minimum and maximum distances between the shoulder joints to avoid any interference between the robots' various parts.

4.1.6 Proposed Design

Following the impact of r and C on the design, and taking into account mechanical restrictions and assembly constraints, the powered module design shown in Figure 55 is proposed.

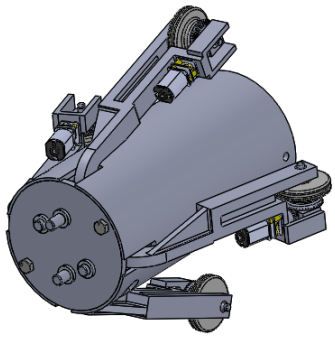

Figure 55: Isometric view of the proposed powered module

In this design, all the components driving the arm linkages are enclosed in the body.

Body The body of the powered module contains the servo motors as well as the power transmitting elements required for locomotion. The mechanical power is transmitted from the servo motors to the arms by a worm gear mechanism. The bare mechanism is shown in Figure 56.

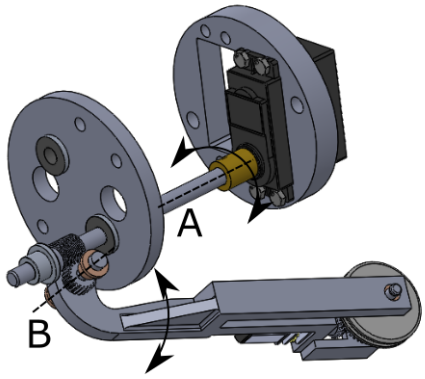

Figure 56: The bare mechanism of the powered module

Figure 56 shows the motion of a servo motor shaft rotating around axis A, that transmits power through the worm gear mechanism and allows an arm to rotate around

axis B. This mechanism is replicated four times, one for each arm of the robot.

This mechanism sits inside the cylindrical body of the robot and is held by holders. The servo motor is fastened to the holder, which is in turn supported by the entire body structure. The mechanism in place inside the body is shown on Figure 57.

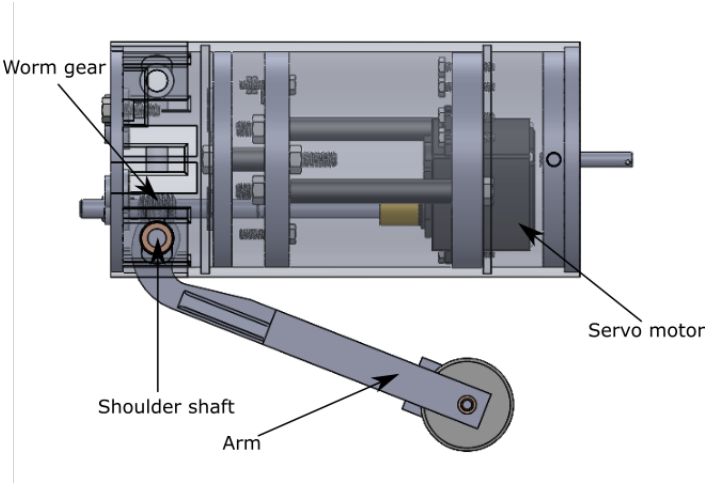

Figure 57: One out of four arm mechanisms inside the main body

Arms The arms are designed to hold their own gear motor and are attached to the servo motors' shafts inside the cylindrical body by a worm gear. The arms connected to the shafts of the two front servos are dimensionally different to the ones connected to the rear servos, but operate in identical fashion.The front type of arm is presented on Figure 58

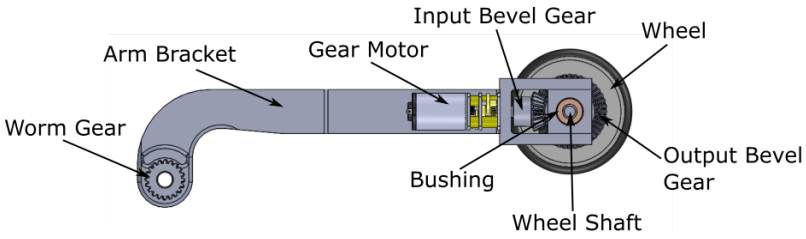

Figure 58: Top view of the arm with labels

The worm gear is secured at one end of the arm and is the connection point with the servo in the body. The gear motor is fixed on the arm bracket and activates a set of

bevel gears that transfer motion directly to the wheel, that is supported on a shaft with bushings.

4.2 Sensing Module

4.2.1 Sensors

The sensing devices used in this pipe inspection robot have to be chosen with different criteria in mind. First, the device itself must be small as the robot will navigate in 6 in diameter pipes. Also, it was mentioned that the optimized value for the diameter of the body of the robot should be half the diameter of the pipe, so the body should have a body of diameter 3 in at most, like the powered module.

The robot will have various sensing devices: a camera, an ultrasonic sensor and a laser sensor. The camera will be mounted in front of the first powered module while the other two sensors will be carried on the sensing module and rotated around the pipe center to gather data about the quality of the pipeline.

Laser Sensor Selection The most important criteria for the selection of a laser sensor for pipe inspection are the size, the precision and the range. The sensor has to be compact to fit with the enclosure of a 3 in diameter cylindrical body, has to be able to take measurements between 1 and 2 in in range with the best possible precision. This is why the selected laser sensor is a SICK Short range distance sensor. This device can measure distances from 20 to 50 mm with a precision of 60 μm with a measuring frequency of $2kHz$ to 250 kHz. It's dimensions are 44.4 mm x 31 mm x 17 mm.

Magnetic Flux Leakage Sensor Selection Magnetic flux leakage inspection device can only be used in ferromagnetic pipelines and this limitation in versatility is the main reason why this type of sensing device has been eliminated. Also, this type of sensor requires sensing devices around the circumference of the sensing body and since the robot has limited space for electronic devices, this type of sensor has been excluded from the proposed design.

Ultrasonic Sensor Selection An ultrasonic sensor functions in a similar way as a laser sensor and could be paired with it for redundancy. The requirements for an ultrasonic sensors are also a small size, with a range of 1 to 2 in. The selected sensor is the SICK ultrasonic sensor UM12. It has a range of 20 to 150 mm, an accuracy of $\pm$ 1% and a working frequency 380 kHz.

4.2.2 Proposed Sensor Module Design

As it has been mentioned previously, the selected method of inspection will be ultrasonic and laser combined. However, in order to inspect the entire circumference of

the pipe, they will be rotated around the pipe axis. Therefore the sensing module will have static and rotating parts. An isometric view of the assembly is shown on Figure 59.

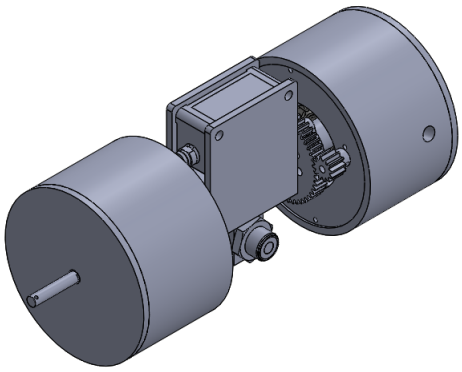

Figure 59: Isometric view of the sensing module

The module is composed of three main sections: two static ends and a central rotating sensor section. The motor located in the rear static section activates the driving gear, which in turn rotates the driven gear and the central shaft is attached to. The sensors are then rotated around the shaft, while the end sections support the shaft with bearings. A slip ring also allows wires to pass from the rotating middle section to the stationary section without entanglement.

Moreover, like the powered module, this module has shafts fixed into the end lids to be linked with powered modules with passive joints.

4.2.3 Resolution and Accuracy

The final resolution of both sensing systems are different, because they gather data at different rates. However, they have the same linear speed as well as rotating speed since they are part of the same module. The ideal number of data points taken at every rotation of the module is arbitrary, but has to be defined. This number will be estimated at 1000 to compute the speed of the motor.

By taking the example of a pipe with equation 5, it's possible to get the maximal motor speed to get the desired resolution. The slowest data acquisition speed is noted f_m and the reduction ratio of the gears is noted n.

$$\omega_{motor} = \frac{60 f_m n}{R_{Radial}}$$

The data acquisition speed of the sensors are in the kHz range, however the microcontroller (Arduino, see section5.3) has a maximum data logging speed through a COM port of a computer of approximately 1000 Hz regardless of the sensor. The gear reduction ratio to be 4, then the maximum speed for the selected motor is 240 rpm. Finding a gear motor that has a lower speed than 240 rpm is not difficult or uncommon. In this case the 175 rpm gear motor from ServoCity would be desirable. So using the calculations from section 2.1.6, it's possible to get the following values for each sensor, presented in Table 6. The linear speed is estimated to be 1 m/s, which is attainable by the motors.

Table 6: Resolution and minimal defect size detectable by the sensors

Data	**Laser Sensor**	**Ultrasonic Sensor**
Typical measuring frequency (Hz)	1000	1000
Axial Resolution(meas./m)	1000	1000
Radial Resolution(meas./turn)	342	342
Minimal axial defect size(mm)	1	1
Minimal radial defect size(mm)	1.396	1.396

5 Simulation

In this section, the robot motion during navigation in various pipe configuration is simulated in Matlab to optimize the wheels' radius, the shoulder width and the length of the joint between each body to avoid collisions and maximum efficiency. The procedure to achieve this is explained in the following sections.

5.1 Possible Pipe Situations

The standardized pipe sizes are given by norm ANSI B36.10M [71] and states the dimensions for pipes of various diameter by giving the nominal diameter, outside diameter and wall thickness for all pipe schedules. The schedule is a standardized number ranging from 5 to 160 and is the indicator of the wall thickness. A low schedule value corresponds to a thin pipe. The standard schedule for pipes is 40 and will be the standard for pipes in the simulations. The values for 6 and 8 inch pipes are given in the table 7.

Table 7: Standard dimensions for schedule 40 pipes of diameters 6in and 8in

Nominal Diameter (in)	**Outside Diameter (in)**	**Wall Thickness (in)**
6	6.625	0.280
8	8.625	0.322

Also, the same norm dictates the minimal radius for elbows or any curved section of the pipeline. There are two types of radii, the short and long radius pipes. The short radius pipes have a centerline radius of 1 times the diameter and the long radius pipes have a centerline radius of 1.5 times the diameter. Since shorter radii are more likely to present difficulties or singularity position for the robot, only the shorter radius pipelines were simulated. Also, the radius of curvature for a pipe is always the same regardless of the number of degrees of the pipeline. Reducing and enlarging section of pipes are also regulated by the same norm.

Four different pipe configurations were simulated in this section: a straight pipe without curvature or diameter changes, a 6 in 90°, a 6in 135° elbow, a 6in 180° return bend and a 8 to 6 in reducing straight section will be analyzed in the simulation in order to cover most of the possible situations the robot could encounter during navigation.

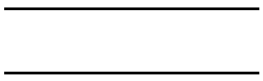

(a) Straight pipe

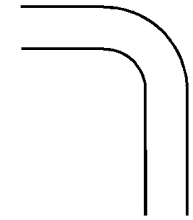

(b) 90 degree elbow pipe

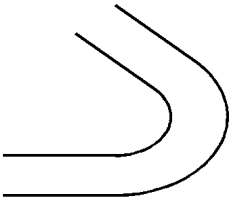

(c) 135 degree elbow pipe

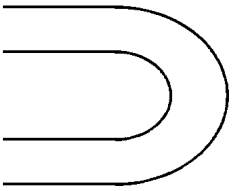

(d) 180 degree return pipe

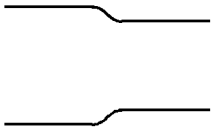

(e) Reducing pipe

Figure 60: Simulated pipe configurations

5.2 Configuration

The simulation of the robot in different pipe situations has multiple objectives. First, to find the values for which various parameters and dimensions produce no collision during navigation and second, to show if any configuration during travel generates a collision with the walls or between two bodies.

5.2.1 Studied parameters

The architecture used to study the different parameters is one powered module at the head of the chain, followed by a passive sensing module without wheels and terminated by another powered module. This architecture is presented in Figure 61.

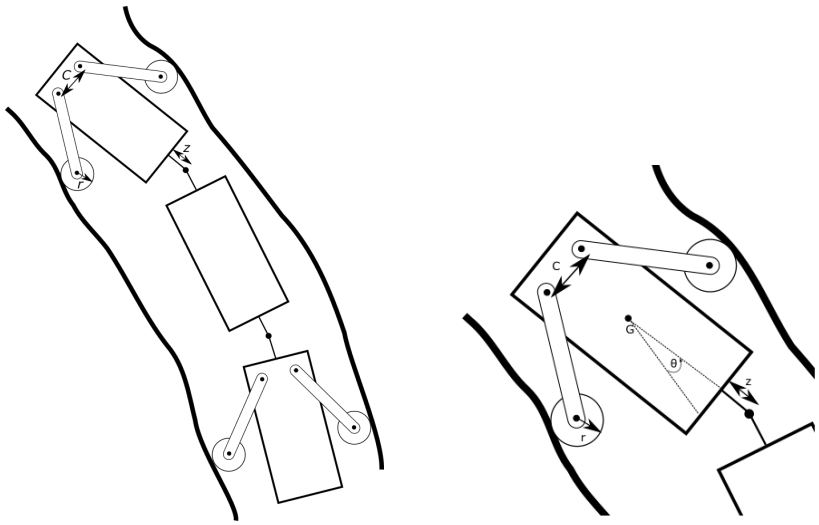

(a) The 3 modules of the robot and the 3 studied parameters

(b) Close-Up of the studied parameters

Figure 61: The studied parameters of the robot

The parameters that can be optimized in this simulation are z the half-length of each connecting member between modules, r the radius of each wheel and C the distance between the shoulder joints. The other parameters are fixed and already optimized from previous works[25].

5.2.2 Robot's Path

One of the most important aspects of the navigation of this robot is the desired path. The powered module's body center will move on the pipe's centerline, with an angle of 0° with respect to the centerline. This way, the corners of the front module are the furthest away from the pipe wall and from a possible collision.

How this would be achieved on an actual built model might be an issue though. The powered module would require some sensors to get data about the location of the pipe's axis. Close close infrared sensors could be used in this case, if deployed around the main body, their signal could be merged to compute values on the pipe's axis during navigation. Mechanical distance detectors could also be used to get data on the pipe's axis and the position of the body with respect to the pipeline. On the other hand, implementing these sensors to the main robot design would require further investigation and work for a fully functional prototype.

The second and third modules have slightly different patterns. The second body, the sensing module, has to keep its center on the pipe's centerline in order to gather data. Therefore the third module, another powered module, will adjust its position to keep the passive sensing module on the desired path. Passive joints allow free movement between each module. An example scenario is shown on Figure 62.

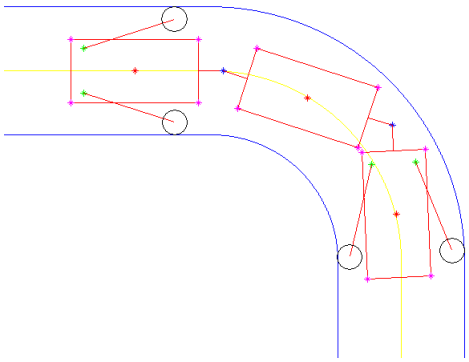

Figure 62: Robot's path along the pipe centerline

The centers of volume (G) of each module, universal joints, and shoulder joints are represented by red, blue and green stars respectively. The simulation attempts to maintain the G of each module as close to the yellow centerline of the pipe.

5.2.3 Collisions

There are four major types of collisions to be detected. The first type of collision is between a corner and one of the pipe walls. The second type is collision between of of the arms and the pipe walls. These two types are external collision, they happen between the robot and its environment and they can be seen on Figure 63.

The other two types of collisions are internal. They represent collisions between two components on the robot. These two collision types can either be collision between

a wheel and the body or between a 2 bodies when they are at angle between each other. They are shown on Figure 64.

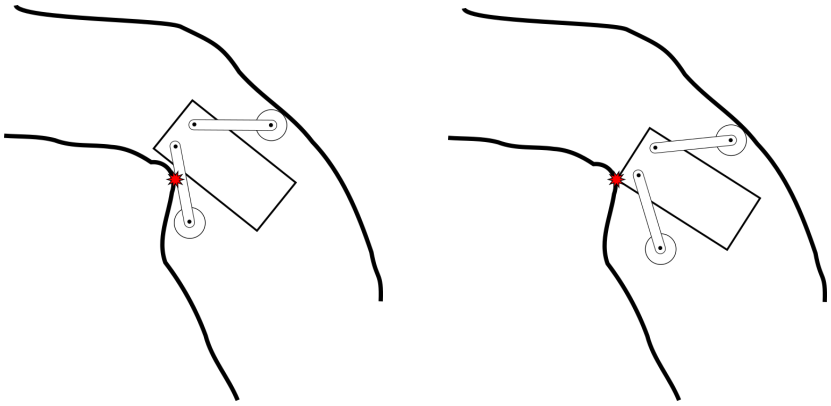

(a) Collision between an arm and a wall (b) Collision between a corner and a wall

Figure 63: Two possible types of external collisions

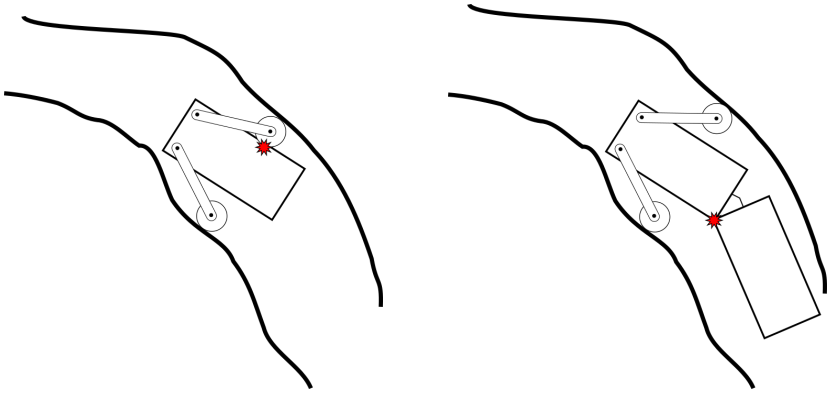

(a) Collision between a wheel and a body (b) Collision between two bodies

Figure 64: Two possible types of internal collisions

5.3 Simulation Procedure

Overview The simulations performed to analyze the design parameters of the proposed robot as well as the number of collisions during navigation have been programmed in Matlab. These programs are two-dimensional geometric analyses of the robot's main features during navigation in different pipeline scenarios. Every frame of the simulation, the robot's features are drawn on a graph using predefined sets of constraints and afterwards, collision detection functions are run to detect interference between the environment of the simulation or between different parts of the robot's body. Simple geometric shapes were used to represent various robot parts for simplicity. The detailed procedure of the simulation program is explained in the following section.

Detailed Procedure First, a predetermined pipe situation is chosen and the pipe walls and centerline are drawn on a figure. Then a first iteration of all modules, arms and wheels is drawn using predefined initial values. Then, the algorithm loops and moves the arms of the first and third modules until the wheels are touching the walls with a precision smaller than $0.1°$. It can be observed on a single module on Figure 65.

Figure 65: Arm movement of the robot

After, the second module is placed at the end of the first module at varying angles in successive iterations until the center of the body is placed on the centerline as shown on Figure 62. Then similarly to the first 2 modules, the last module is placed following the sensing module and the algorithm loops its angle and arms positions multiple times until the center of volume is on the centerline and the wheels are touching the walls.

When the three modules and four arms are placed and within the error margin for the simulation, the first module's center of volume is moved along the centerline and the algorithm loops every modules positions and angles to respect the desired path again. This process is repeated until the first module reaches the predefined end of the centerline. During the simulation, the arms' angular positions, the wheels' positions, the wheels' speeds and the number of collisions is gathered for further analysis.

5.3.1 Objective

The first objective of the simulation is to detect if there will be one or more collisions for a given set of parameters during a simulation. The goal is to have a certain number of sets of z, r and C that produce zero collisions during the entire simulation. However, this objective is not necessarily achievable with the given parameters taken from previous work. These previously optimized values have to be tested to check if they produce collisions or interference and should be changed if they do.

5.3.2 Algorithm

The values of z, r and C are optimized by iterating each variable over the range of values provided in Table 8 and measuring the number of collisions produced.

Table 8: Range of values for values to be optimized

Variable	**Minimum Value (m)**	**Maximum Value (m)**
r	0.005	0.025
C	0.030	0.061
z	0.015	0.045

The flowchart of the algorithm used to optimize the values is shown in Figure 66. All combinations of z, r and C are tested using a brute-force method to obtain the behavior of the robot under all possible combinations as well as the number of collision with each combination of variable.

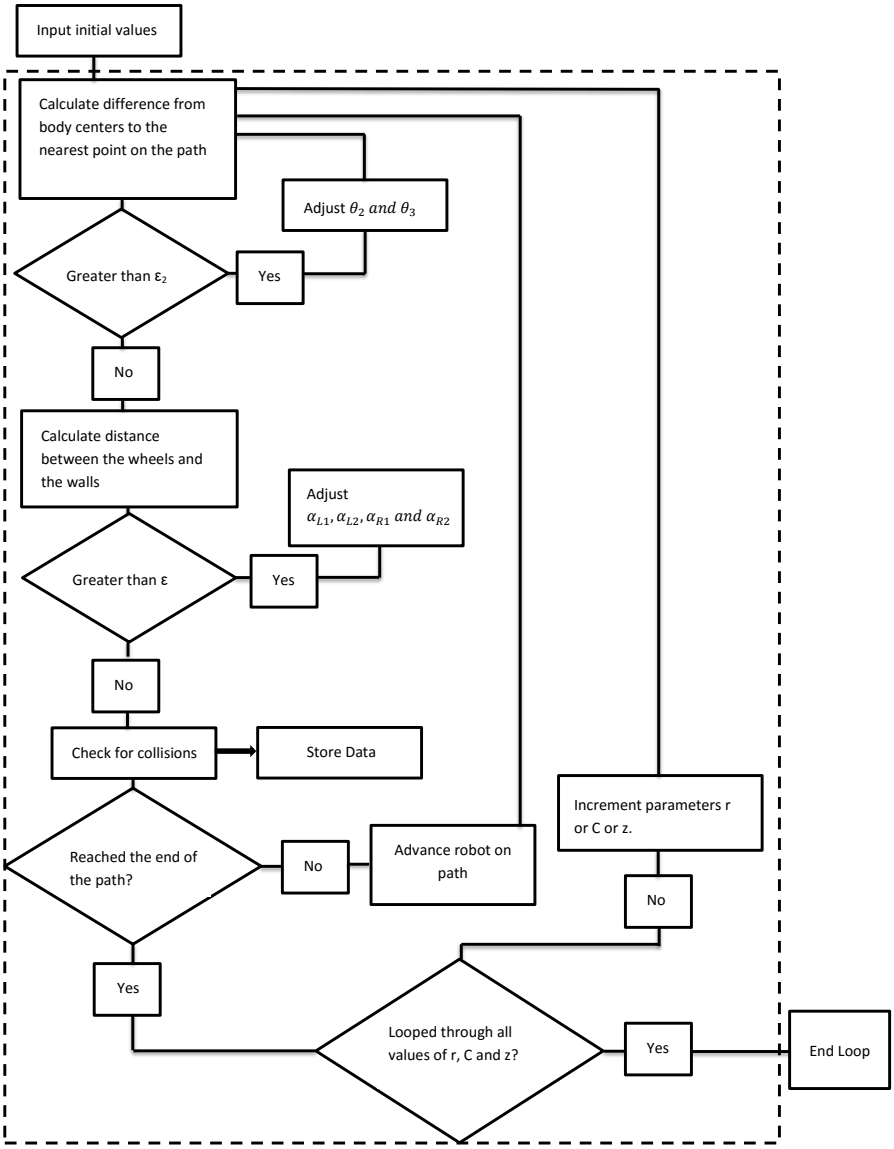

Figure 66: Algorithm to detect the number of collisions per simulation

5.3.3 Algorithm Results

The method described gives the number of collisions per set of variable. These values plotted on a level graph is shown on Figure 67.

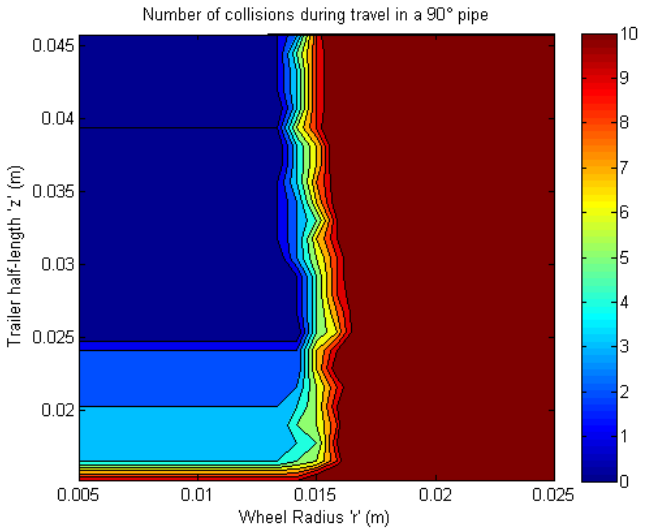

Figure 67: Number of collision with changing parameters r and z with $C = 0.3D_{Pipe}$

This graph shows the region of values of r and z that are collision-free in dark blue for a value of the shoulder joint location C equal to $0.3D_{pipe}$. The graph shows plainly that for shorter trailer half-length z or larger wheel diameter r, there are more collisions.

The same experiment is repeated for various values of C. These results are shown on Figure 68.

The results for various values of C, shown in Figure 68, illustrate that the shoulder joint location has little influence on the number of collisions for this scenario.

Also, the number of collisions drastically increases for a wheel radius over 0,015m. Bigger wheels' radius reduces the angle of the arm with respect to the wall. This is advantageous as the contact force exerted by the shoulder joint motor is increased as the contact is made with the wall at a more perpendicular angle. Also, a greater wheel radius means faster traveling speed for the robot. Though high linear speed is not a crucial requirement for the robot, the ability to move faster would allow it to cover more pipeline distance per battery charge.

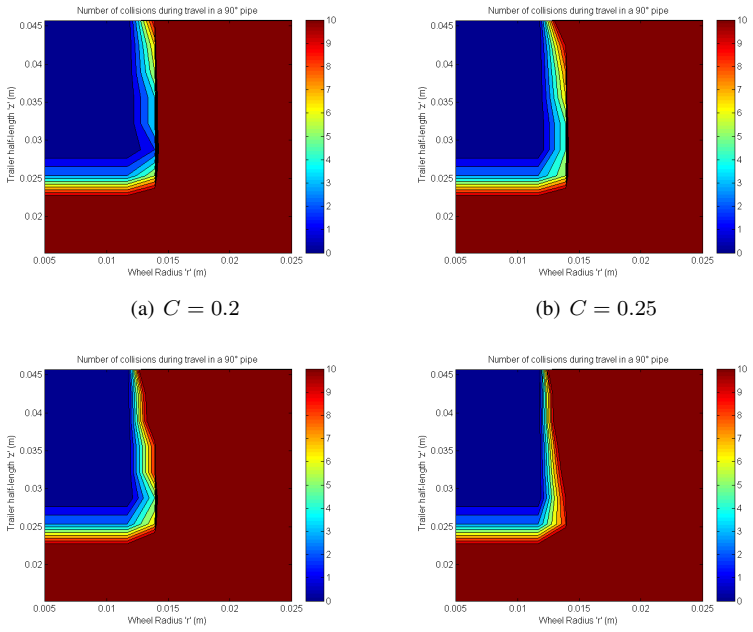

(a) $C = 0.2$ (b) $C = 0.25$

(c) $C = 0.35$ (d) $C = 0.4$

Figure 68: Collision simulations in a 90° pipe with varying values of C

To determine the most accurate wheel diameter, the simulation was performed using a narrower range of values. This focus on a smaller set of values for the wheel radius is performed to be able to visualize with more accuracy the effect of the wheel radius on the number of collisions. The initial simulation was too coarse to evaluate this effect with precision. The number of collisions jumped from 0 to 10 rapidly with the increase in r, so reducing the range to 0.012m to 0.014m, where the simulation showed an increase in collisions, could help understand the effect of the r value. Results are shown on Figure 69.

These graphs show similar patterns, but seem to suggest that the C parameter plays an important role. The dark blue region corresponding to zero collision during travel shrinks when C increases. However, larger values of C are desired because they provide a better mechanical advantage for the shoulder joint motors.Therefore, the gathered results show that values for parameters r, z and C that don't produce any collision during navigation are 0.0125m, 0.03m and $0.4 * D_{pipe}$ respectively.

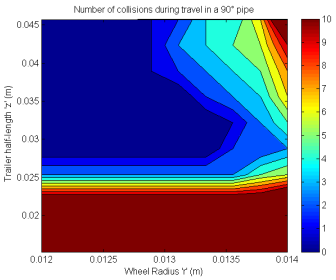

(a) $C = 0.2$

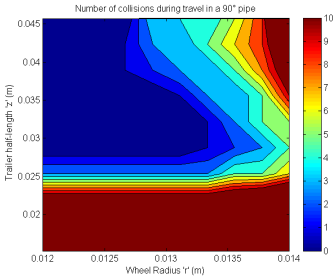

(b) $C = 0.25$

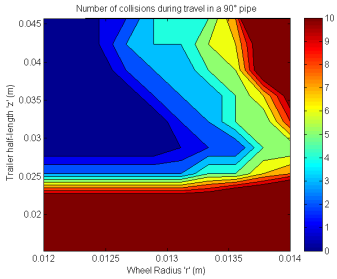

(c) $C = 0.3$

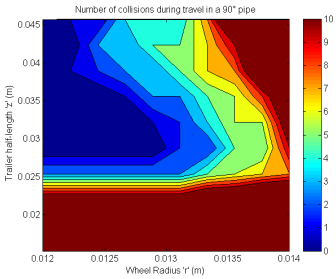

(d) $C = 0.35$

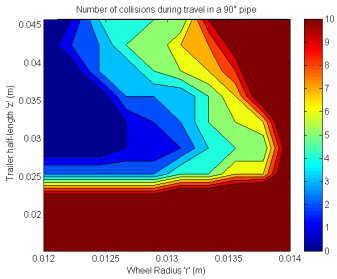

(e) $C = 0.4$

Figure 69: Collisions in a 90° elbow bend for various values of C

5.4 Robot Navigation

Knowing the optimized parameters obtained in the previous section, it's possible to simulate a robot with these parameters traveling in various pipeline configurations to analyze the navigation of the proposed design. The results are presented by simulation scenario. It is important to note that the obtained results in this section are for simulation in perfect pipelines without defects.

5.4.1 Straight Pipe

The simulation for a straight pipe results in constant arm angles and wheel velocities, the results of which are presented in Appendix C. Unsurprisingly, these obtained results are achievable by the selected motors as they remain constant during travel.

5.4.2 90° Elbow Pipe

The 90° elbow pipe bend is the first simulation challenge for the pipe inspection robot. The robot has to follow the desired path that was defined and explained in section 5.2.2 to keep the robot modules' centers on the pipe centerline axis. Using the algorithm described previously, the simulation was performed using parameters that produced no collision. The simulation is represented in six steps on Figure 70.

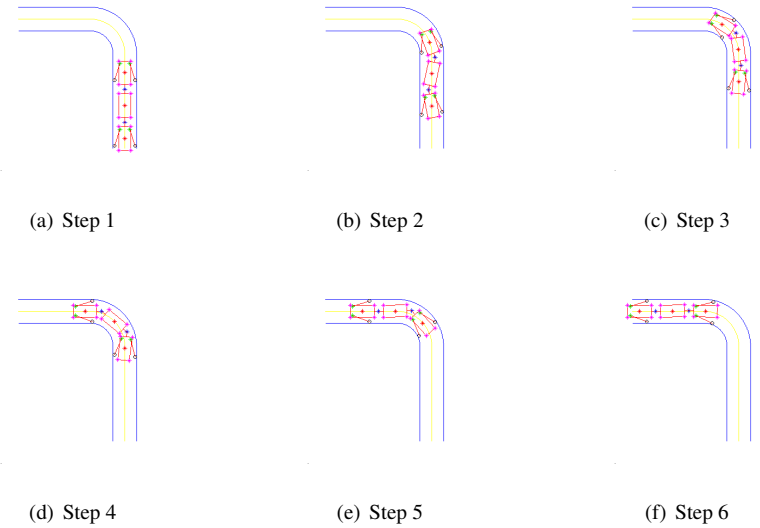

(a) Step 1 (b) Step 2 (c) Step 3

(d) Step 4 (e) Step 5 (f) Step 6

Figure 70: six steps of the entire simulation of the three first modules in a 90° elbow bend

This combination of figures illustrates that the robot can travel inside the pipeline with all the modules' centers on the pipe centerline axis. The center of volume of each module is represented by a red star and the pipe's centerline axis by a yellow line.

During this simulation, the value of multiple variables were stored to visualize the position or speed of various components to replicate the motion when the robot is fabricated. The values obtained this way are the angle of each arm with respect to the body, the distance traveled by each wheel, as well as the speed of each wheel at all times. They are shown respectively on Figures 71, 72 and 73.

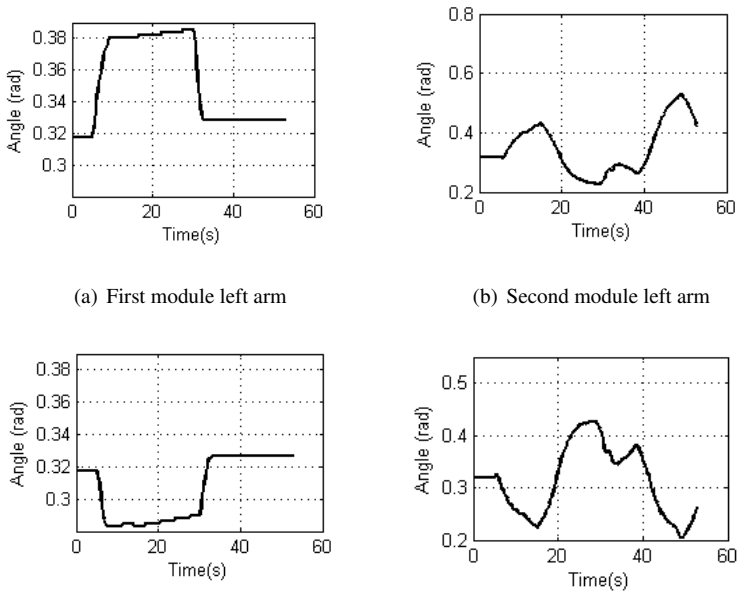

(a) First module left arm

(b) Second module left arm

(c) First module right arm

(d) Second module right arm

Figure 71: Angle of the arms of the two powered modules during travel in a 90° bend

On Figure 71 it's possible to see that the movement of the arms of the first module are more linear and they dictate the overall configuration of the robot. The second powered module's arms are continuously adjusting to ensure the sensing module stays centered on the pipe axis, hence the fluctuations seen on the graphs.

Also, the highest arm angle displacement is experienced on the first module's left arm (top left graph on Figure 71) and is approximately 0.06 rad. Which translates to around 3.5°, which is well within the 18° operating angle of the arms.

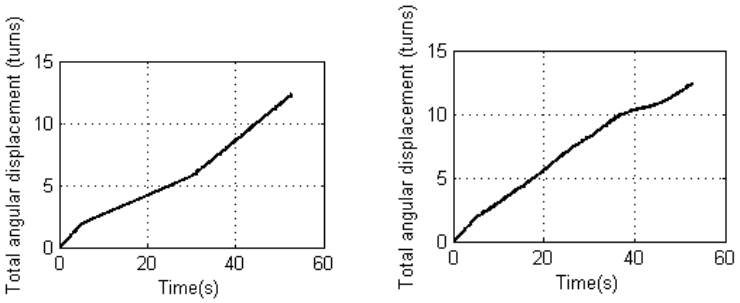

(a) First module left arm

(b) Second module left arm

(c) First module right arm

(d) Second module right arm

Figure 72: Angular position of the wheels of the two powered modules during travel in a 90° bend

On Figure 72, the angular displacement of each wheel is shown. Mostly linear line segments are obtained, with slight variations in slope when the modules are in the bent section of the pipe. These slope changes are mostly due to the fact that during a turn, the outer wheel needs to rotate faster to keep the robot with the same orientation.

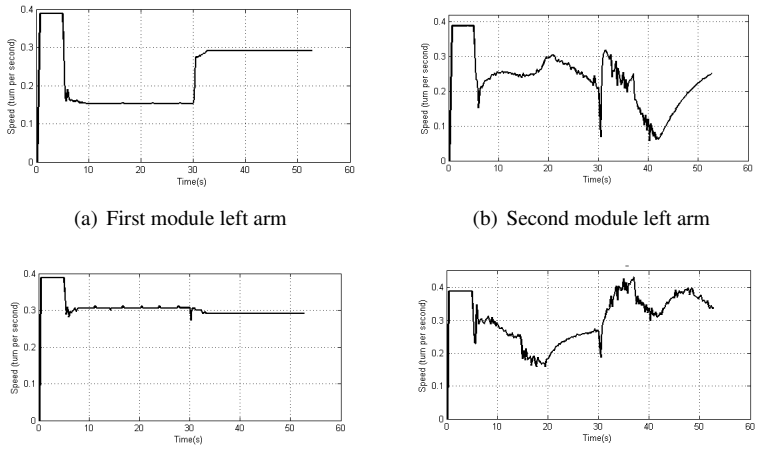

(a) First module left arm

(b) Second module left arm

(c) First module right arm

(d) Second module right arm

Figure 73: Angular speed of the wheels of the two powered modules during travel in a 90° bend

On Figure 73, the value of speed of the wheels are shown. This is arguably the most valuable result since the robot will be navigating using the speed of its motors as it will be explained in section 7. It's possible to see in these graphs that like the arms, the first module dictates the wheels' speeds and the second module adapts to provide stability and alignment for the sensing module.

The most extreme values of speed encountered during the simulation are 0 at the very beginning and approximately 0.45 turns per second during the peak speed periods. It translates to a speed value of 27 rpm, which is well below the theoretical maximum of the system of 2450 rpm (4900 rpm / 2).

Since the values required of the motors are attainable without causing collisions, the robot is able to navigate this type of pipeline. However, the large gap between the required speed and attainable speed is explained by the fact that the simulation was performed for 60 seconds, which averages the linear speed of the robot at about 0.02 m/s. The linear speed of the robot could possibly be raised without changing motor selection to cover more pipeline length. This simulation was aiming to confirm that the robot could travel in this type of pipeline without hindrance with the selected motors, but further simulations could be performed to validate the maximum speed of the robot.

5.4.3 135° Elbow Pipe

In a similar fashion to the last scenario, a simulation has been performed in a pipe with a bend of the same radius, but over 135° instead of 90°. The main parameters and conditions are kept, which means that the robot travels while keeping all the body centers as close as possible to the pipe centerline axis, all wheels stay in contact with the walls and these are passive joints between each module. The simulation broken down in six steps is shown on Figure 74.

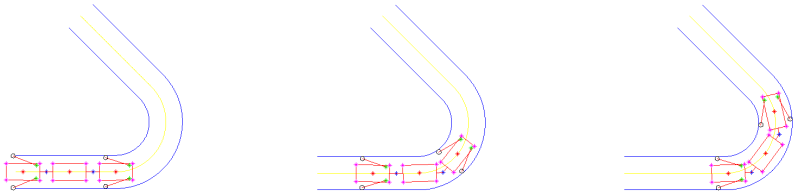

(a) Step 1 (b) Step 2 (c) Step 3

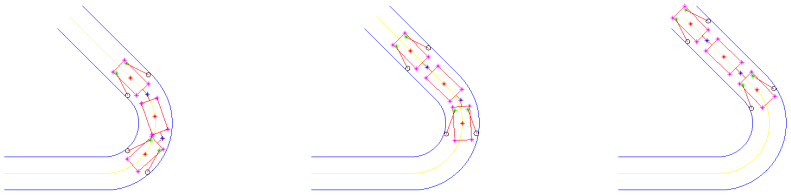

(d) Step 4 (e) Step 5 (f) Step 6

Figure 74: six steps of the entire simulation of the three first modules in a 135° bend

In this scenario, the angles and positions of the arms and wheels was also gathered. The results obtained for this simulation show a similar trend as the 90° pipeline results, although they have their own particularities. First of all the arms' position over time are shown on Figure 75.

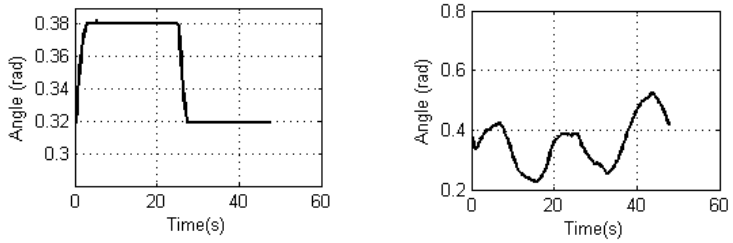

(a) First module left arm

(b) Second module left arm

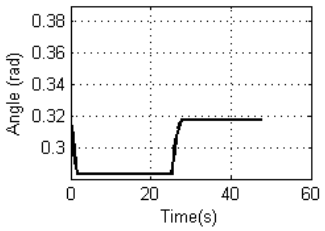

(c) First module right arm

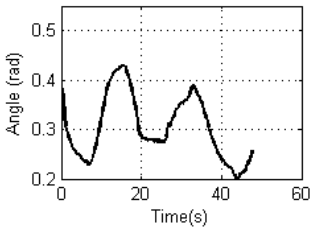

(d) Second module right arm

Figure 75: Angle of the arms of the two powered modules during travel in a 135° bend

The arms of the second power module have an alternating motion to keep the centers of volumes on the centerline path. The first power module dictates the overall position of the robot. The largest angular displacement is performed by the second module left arm and ranges from about 0.23 to 0.5 rad which is around a 15° variation. It is still inside the 18° maximum range of the motor.

The wheels' angular displacement are shown on Figure 76 and the larger right arm values obtained represent a left turn in the pipeline. The continuous curves indicate singularity-free movement during the simulation.

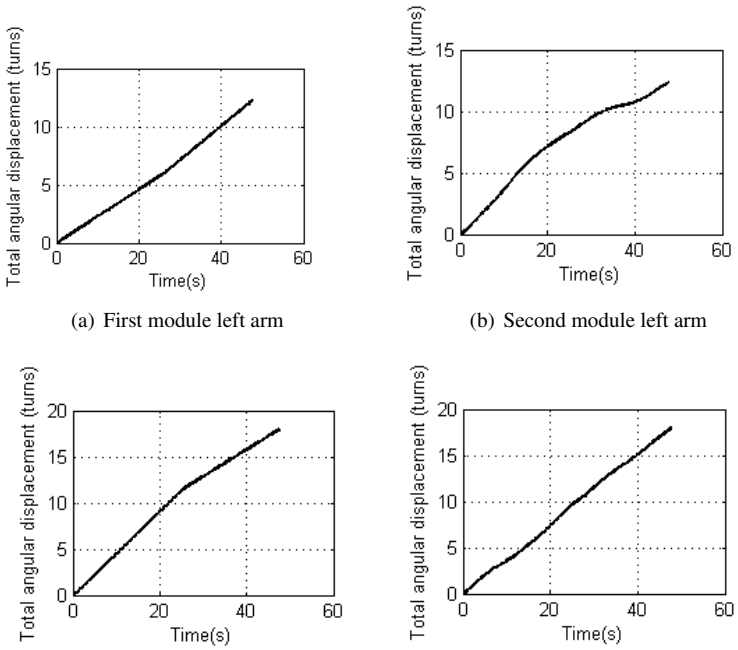

(a) First module left arm

(b) Second module left arm

(c) First module right arm

(d) Second module right arm

Figure 76: Angular position of the wheels of the two powered modules during travel in a 135° bend

The wheels' speeds are shown on Figure 77.

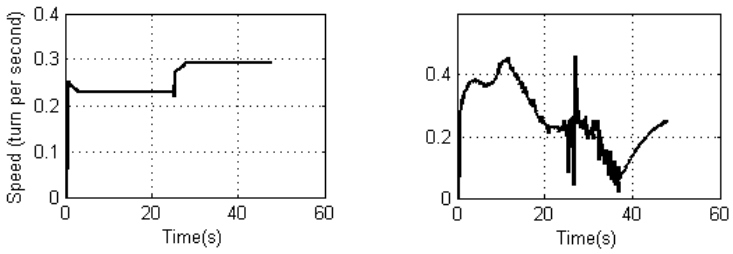

(a) First module left arm

(b) Second module left arm

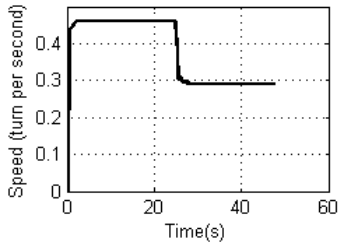

(c) First module right arm

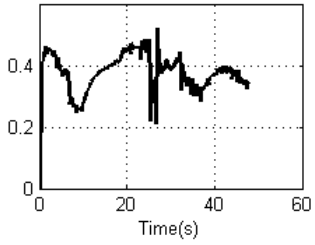

(d) Second module right arm

Figure 77: Angular speed of the wheels of the two powered modules during travel in a 135° bend

The speeds of the first modules' wheels are mostly stable, with variations when the robot goes from a curved section to a flat section or vice versa. The second powered module wheels' speeds fluctuate more, especially in the transition regions. The main reason is that the overall speed is dictated by the first power module and when it gets out of the curved section, it accelerates a little bit and the other modules have to respond appropriately. This simulation also yields maximum wheel speeds of approximately 0.45 turn per second that are attainable by the motors.

5.4.4 180° Return Pipe

To complete the study of the robot in curved pipelines bends, a simulation in a 180° pipe has been performed. The simulation is shown in six steps on Figure 78.

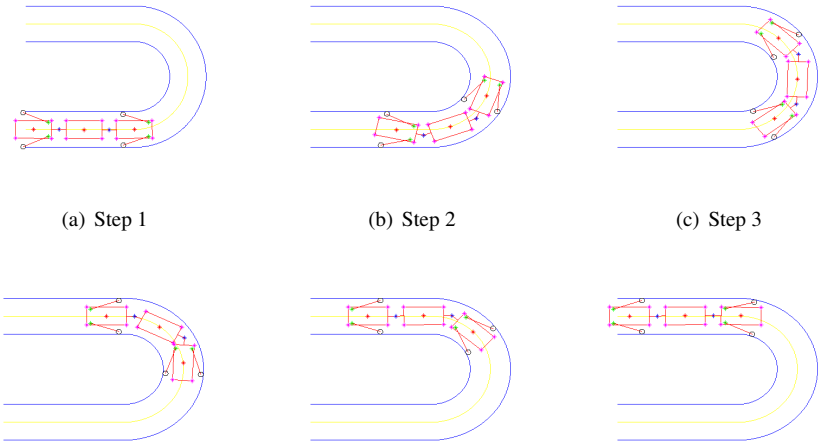

(a) Step 1 (b) Step 2 (c) Step 3

(d) Step 4 (e) Step 5 (f) Step 6

Figure 78: Six steps of the entire simulation of the three first modules in a 180° return bend

The same data is taken from this simulation to obtain the arms' angle as well as the wheels' angular displacement and speed over the time of the simulation. The data is shown respectively on Figure 79, 80 and 81.

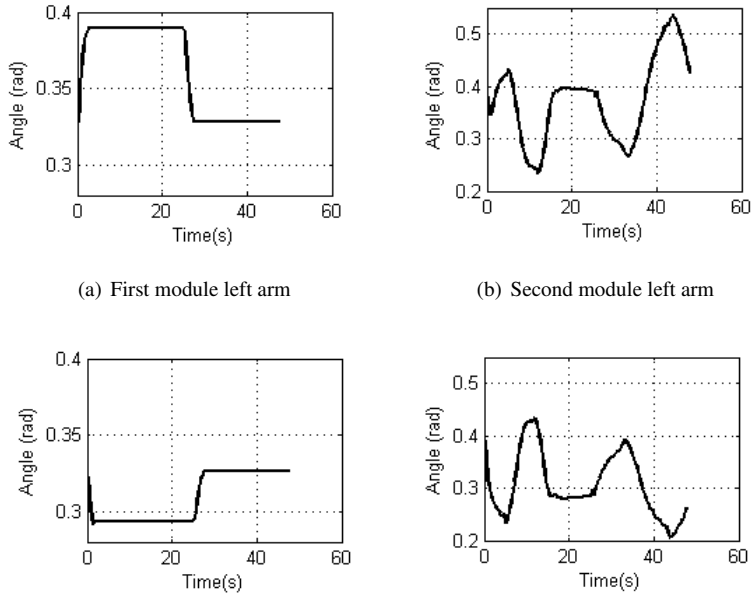

(a) First module left arm

(b) Second module left arm

(c) First module right arm

(d) Second module right arm

Figure 79: Angle of the arms of the two powered modules during travel in a 180° return bend

The three graphs show the same characteristics as the previous simulations in 90° and 135° pipe bends, with minor differences, due to the longer curvature of the pipeline. Essentially, the robot still shows smooth and stable movement on the first power module and undulating movements for the second power module to keep the body centers along the centerline.

The arm angular positions show maximum amplitude on the second module left arm again and is of 0.28 rad. This is also within the 18° range of the arms' servo motors.

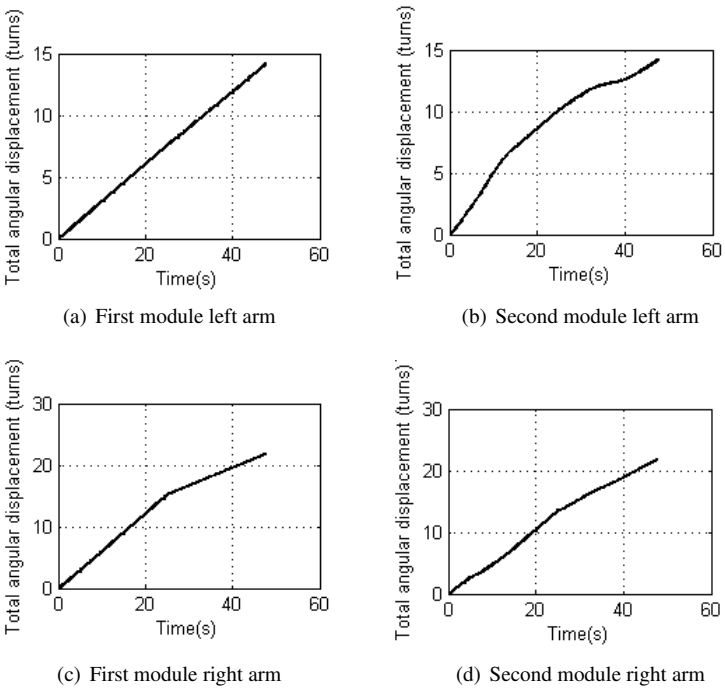

(a) First module left arm

(b) Second module left arm

(c) First module right arm

(d) Second module right arm

Figure 80: Angular position of the wheels of the two powered modules during travel in a 180° return bend

The linear segments on Figure 80 represent smooth, singularity-free movement. Also, the right wheels show more displacement than the previous pipe scenarios. This was expected, as the curvature is longer than the other scenarios.

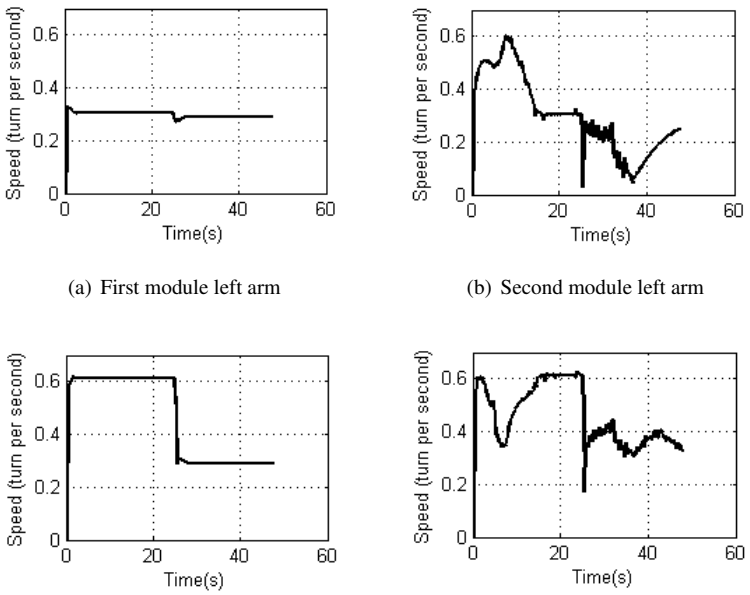

(a) First module left arm

(b) Second module left arm

(c) First module right arm

(d) Second module right arm

Figure 81: Angular speed of the wheels of the two powered modules during travel in a 180° return bend

The maximum speeds for the wheels reached peak values of 0.6 turn per second ($36rpm$) which is higher than the other pipe bend scenarios, but still within the maximum attainable values for these motors.

A notable particularity of this simulation is the sudden drop in wheel speed at around the 35 second mark. This time corresponds to the front module leaving the curved section to enter the straight section. This causes a small shift in the front wheel speeds and also causes the second module wheels to adjust their speeds to compensate for this change, in this case in dropping the speed momentarily.

The robot is therefore also able to navigate without collisions in a 180° pipe bend.

5.5 Changing Diameter Pipe

The robot is designed to adapt to any pipe diameter between 8 and 6 in. Therefore, a simulation a a pipe section reduction from 8 to 6 in is performed to analyze the ability of the robot to travel in pipelines of this type. The simulation in shown in six steps on Figure 82.

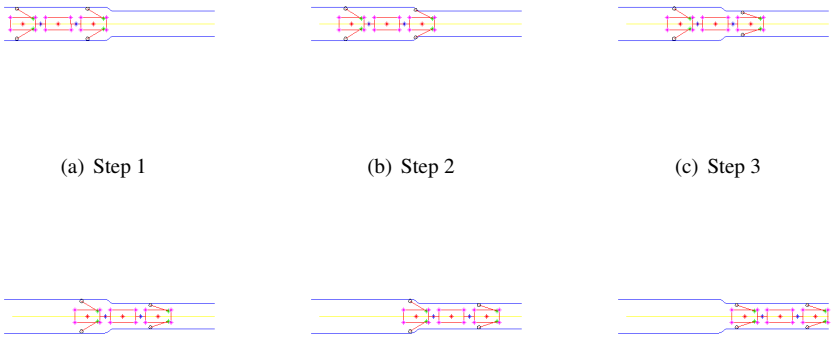

(a) Step 1 (b) Step 2 (c) Step 3

(d) Step 4 (e) Step 5 (f) Step 6

Figure 82: Six steps of the entire simulation of the three first modules in a pipe of reducing diameter (8 to 6 in)

As with the other simulations, the robots' analytical motor positions have to be obtained through this simulation. They are shown in Figures 83 and 84. The wheels angular positions don't illustrate different information and therefore are presented in Appendix C.

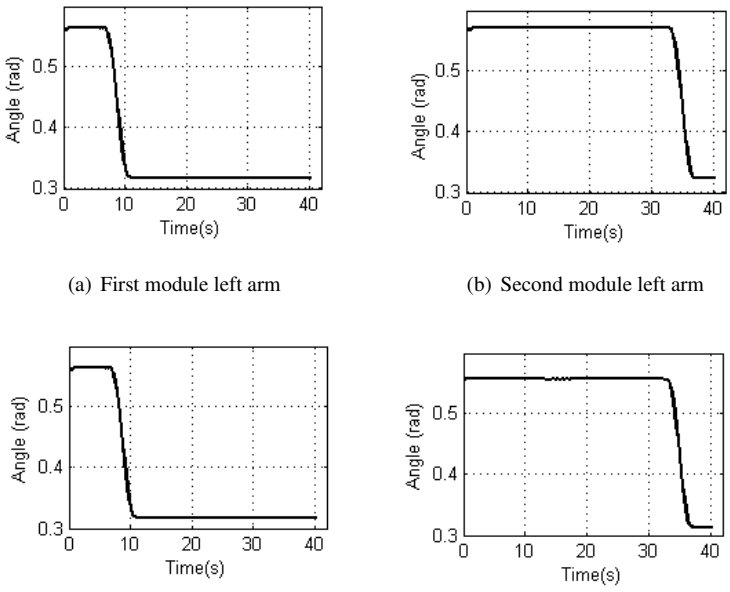

(a) First module left arm

(b) Second module left arm

(c) First module right arm

(d) Second module right arm

Figure 83: Angle of the arms of the two powered modules during travel in a pipe of reducing diameter (8 to 6 in)

Figure 83 looks as expected. The front module enters the reducing section before the second module and they retract around the body to accommodate the smaller diameter in a symmetrical way. Both modules show the same values of angles, which is expected since the two modules are identical. The maximum angular displacement for the arms in this scenario is approximately 14.3°, which is also within the range of the servo motors.

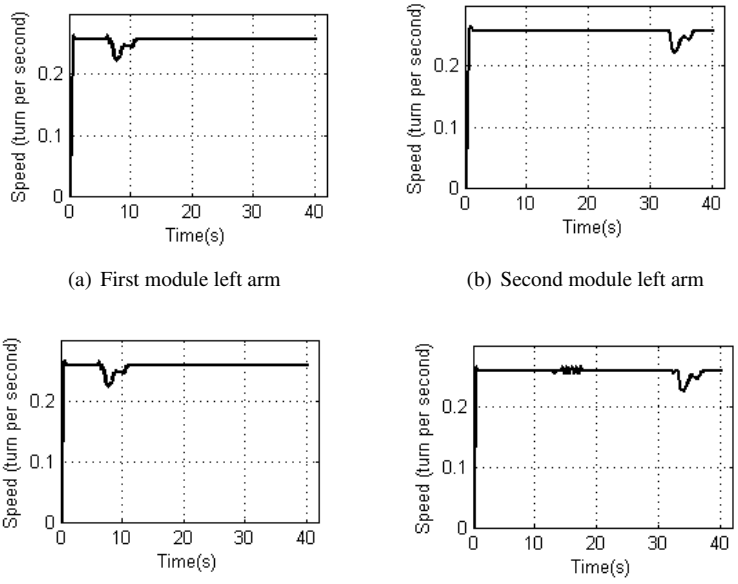

(a) First module left arm

(b) Second module left arm

(c) First module right arm

(d) Second module right arm

Figure 84: Angular speed of the wheels of the two powered modules during travel in a pipe of reducing diameter (8 to 6 in)

Figure 84 shows that the speed of the wheels remain mostly constant when the pipeline is flat, as expected. However, when the diameter varies, the speeds of the wheels fluctuate a bit so the module entering the reduction in diameter stays at the same overall speed as the other module. Also, the graphs are very similar for the left and right wheels, which is expected in a straight pipeline with even diameter reduction on all sides. Also, the speeds required of the wheel motors in this simulation are within their range and the robot is hence able to navigate in a pipe reducing section from 8 to 6 in.

6 Discussion and Manufacturability

In this section, all the differences between the original design ideas and the fabricated robot will be explained. Also, the limitations of the robots will be presented with their underlying consequences. Finally, modifications and fixes will be suggested for subsequent iterations of the robot.

6.1 Design

There has been many design choices made throughout the development process of the proposed robot. However, some of these choices could be improved to achieve a more efficient performance of the robot.

6.1.1 Body

The robot's body is the main structural part of the entire assembly. It's main purpose is to be the housing of all the important mechanical components required for the locomotion of the robot. The body must also be compact with respect to the components it contains, as it must be of dimensions defined earlier in previous work and this one to be most efficient in operation and still allow navigation without collision in pipes of 6 to 8 in. The description of the assembly details are presented in the following section.

Body Design In this section, the assembly details of the proposed design will be explored more thoroughly. Each arm assembly consists of a servo motor connected to a worm shaft and supported with bushings on structural components. A single servo assembly is presented in two different views on Figure 85.

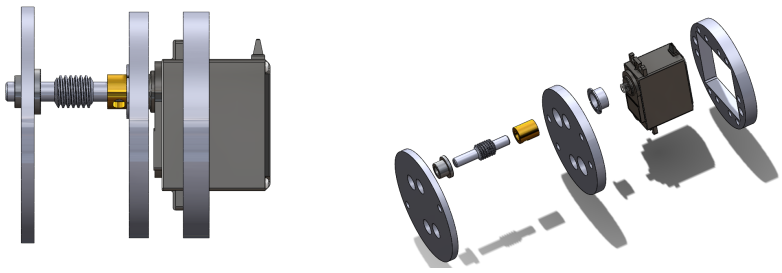

(a) Assembled single servo motor assembly

(b) Exploded view of single servo motor assembly

Figure 85: Single servo motor assembly

Figure 85 shows one servo assembly to represent the mechanism as well as the support points of the servo and the shaft. The entire robot powered module consists of four of these assemblies and are presented on Figure 86.

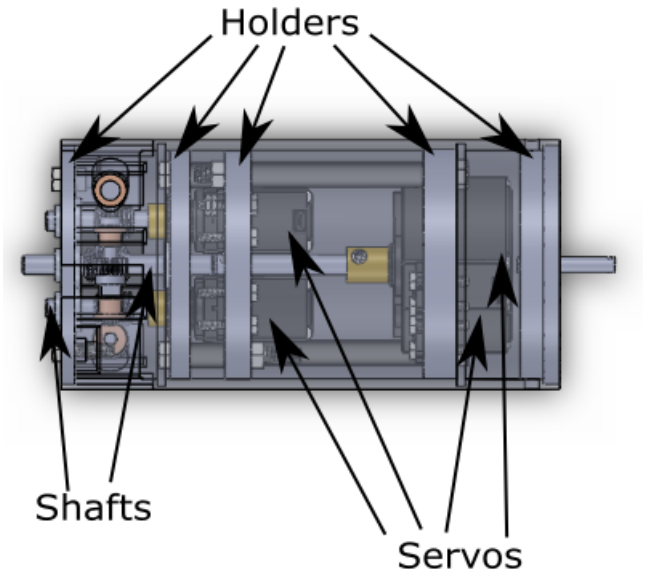

Figure 86: Top view of the powered module body

Figure 86 shows how tightly the four servo motors are assembled. Two pairs of servo motors control two pairs of opposite arms at the shoulder joints. In order to control four joints at the same end of the robot's body, the two rear servo shafts have to go between the two front servo motors. This way, the design variables defined earlier can be respected.

In order for the servo motors to be able to transmit torque through the worm gears on the shafts, all the components must be tightly assembled because worms tend to create high axial forces. First of all, servos are secured to servo holders, the shafts are then coupled to the servos and then slid through bushings into shaft holders.

The robot is assembled by sliding the main mechanisms inside the body and securing everything in place with end lids fixed by bolts. The main assembly procedure is shown on Figure 87.

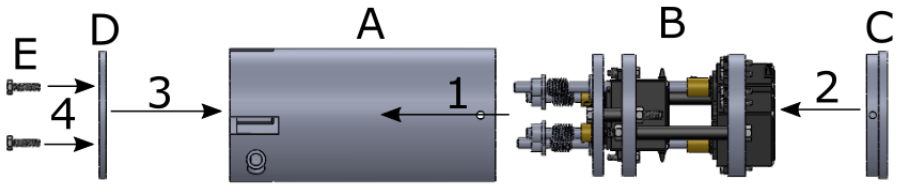

Figure 87: Exploded view of the powered module body assembly

Figure 87 shows the servo assembly B, being inserted in the direction of arrow 1 inside the cylindrical hollow body A. Once the servo assembly is rotated into its final resting place, the back lid C is bolted onto the main body behind the servo mechanism. Finally, the front lid D, is bolted (E) onto the body A as well.

Body Fabrication The inner components of the robot were assembled. The cylindrical holders supporting the servo motors and the shaft bushings were 3D printed, like the body itself and the shafts were machined out of aluminum. The robot's body is presented with and without the outside cover on Figure 88

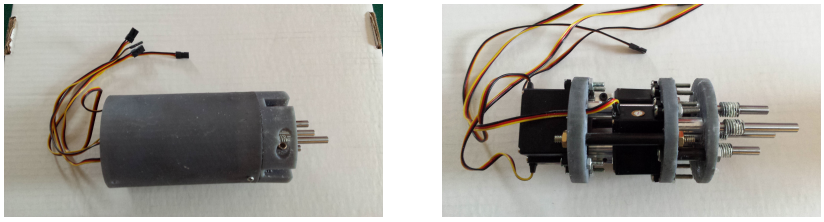

(a) Robot's body with body cover (No arms)

(b) Robot's body without cover (No arms)

Figure 88: Robot's main body components

All these components were printed or machined exactly like the original design, except the body cover was 3D printed in two parts. The reason for this change is that the 3D printer could not print a part of that size. So both parts were printed separately and then screwed together as can be seen on Figure 88.

The interior servo motors and holders assembly performed as expected, the parts were solidly assembled and there was no interference between the parts. However, the front of the outside body cover was a source of problems. The material had low strength and bent under load. As a consequence, the servos were unable to transmit useful torque to the arms. The faulty regions are indicated in Figure 89.

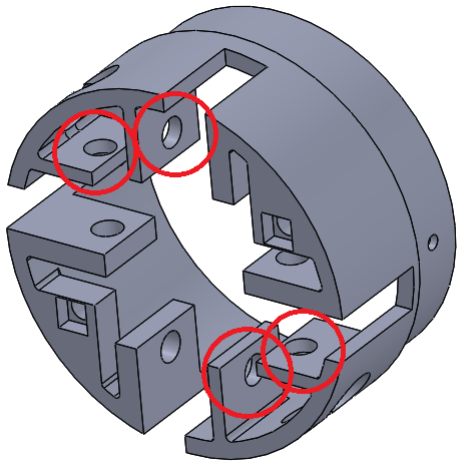

Figure 89: Front body housing with problematic regions circled in red

In Figure 89 support flanges for the shoulder motor shafts are circled in red. These flanges were under significant axial and radial load from the worm gear mechanism powered by the servo motors. The low thickness of the flanges prevented transmission of torque to the arms because they bent under the load due to their low density and strength as well as high porosity of the 3D printing material.

Body Design Solutions There are various possible solutions for this, first is to add material to the design to have thicker support flanges or supporting ribs, but increasing the thickness of these flanges would cause interference between components during navigation. Second solution is to add supporting material around the body to prevent that part from bending. This solution has been explored and will be discussed later. The third solution is to machine this part out of a more solid material like aluminum. Although it would be a costly and time consuming solution as it would require many hours of machining on a computer controlled machine. This kind of machining would not fit within the time frame for the project, but would be a solution for another iteration of the robot.

The body design would have to be modified to make it machinable because the current model is designed with a 3D printing process in mind, whereas a solid aluminum body part would have different requirements. Figure 90 shows the differences in the 3D printed design and the machined design.

Figure 90 shows the five main design changes that should be made for a functioning second iteration of the robot. Letter B in the figure shows the tabs or flanges that support the shafts in the assembly should be machined separately and then slid into

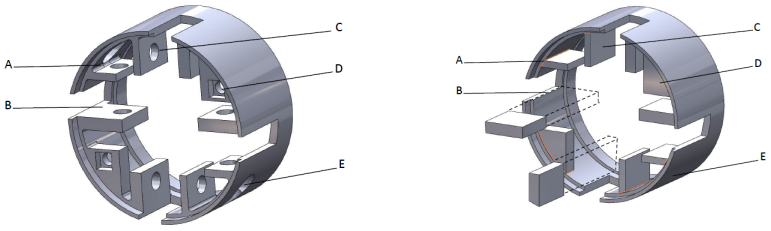

(a) 3D printed design (b) Machined arm design

Figure 90: Differences between the 3D printed design and the machined design

place and welded. Letter A shows where the welds should be. Letter C on the figure is the hole for the bushing that supports the shaft that doesn't appear on the modified version. This hole still needs to be machined, however to increase the precision of the assembly and ensure the shaft is correctly aligned, this hole should be drilled after the tabs are welded into place. Letter E shows other holes that are only aimed at allowing the shafts to be assembled. The figure on the right doesn't show this hole for the same reasons the holes represented by the letter C are machined after installation. However they wouldn't have to be made after the tabs are welded because they are only clearance holes, but it would simplify the drilling and machining operations required. Finally letter D shows the square hole with a round hole inside that disappeared on the figure on the right. The purpose of these holes is to hold a square nut in place to secure the front lid during assembly. However drilling a square hole is not possible and another type of fixture should be used. In this case a nut with a lock washer would be sufficient to hold the front lid in place. The round hole however should be machined after the front lid is in place again to ensure the alignment between the front lid and the body.

6.1.2 Arms

The arms of the robot proposed powered module is designed to transmit torque from the worm shaft and worm gear assembly of the shoulder joint to the wheel that is in contact with the pipe wall. Its design is explained in the following section.

Arm Design The arm design of the robot is an L-shaped solid part with a joint at each end for the shoulder and the wheel. This shape is necessary to avoid interference between the arm and the body itself. It is connected via bevel gears at the wheel's end and via a worm gear mechanism on the shoulder end. An arm assembly is shown on Figure 91.

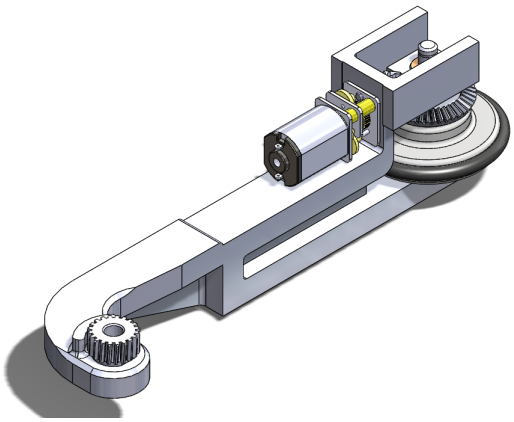

Figure 91: Powered module arm design

Figure 91 shows the main components of the arm assembly and the details of its design are also apparent. The worm shaft discussed earlier connects to the worm gear shown on the bottom of the figure. However, the propulsion of the robot is ensured by the gear motors installed on the arms directly as can be shown on the top of the figure. This design encapsulates the wheel mechanism in a compact region to avoid collision between the pipe wall and the arm as much as possible since the confined environment of operation of the robot is prone to difficult and singular configurations. Also for the same reasons, the arm's design is slender and ribs are added to increase the rigidity and structural integrity of the arm.

These arms are assembled in a particular fashion, this process is illustrated on Figure 92.

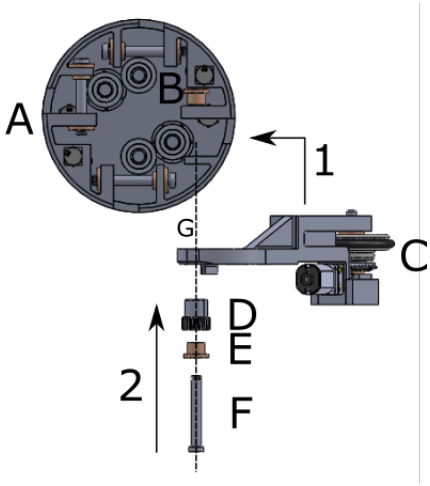

Figure 92: Exploded view of the powered module arm assembly

On Figure 92, the assembly procedure of an arm is shown. First, bushing B is put into place on main body A. Then arm C is inserted into the body from the side and is secured by subsequently inserting worm gear D, bushing E and shoulder shaft F along arrow number two (axis G), through a hole on the cover of the body. Finally a circlip (not shown) is put on shoulder shaft F to secure it in translation. All four arms are assembled similarly to complete the robot.

Arm Fabrication The robot's arms are also 3D printed parts. The actual arm is similar to the original design, as it can be seen on Figure 93.

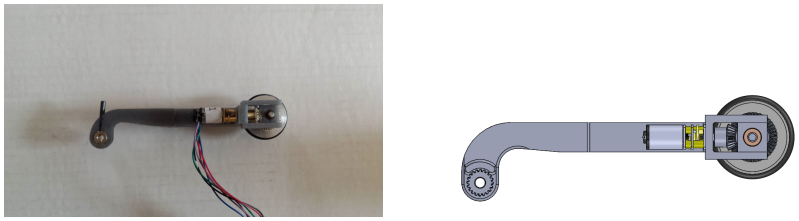

(a) Robot's assembled arm (b) Designed assembled arm

Figure 93: Comparison of the designed and actual robot's arms

A minor change added to the final design is the pin inserted in the arm into the worm gear, as can be seen on Figure 93a). The original design included a press fitted worm gear into the arm. However, after a short test period, the gear tended to wear the arm material. Press fitting a brass worm gear into a softer, less dense and more porous

material caused backlash due to wear in the system. Therefore the pin transmits torque from the worm gear to the arm with less backlash.

The arms of the robot were also made of 3D printed material that bent significantly under load and therefore could not apply sufficient force on the the pipe wall to function properly.

Arm Design Solutions There are multiple solutions to alleviate this situation. First, machining the arms in aluminum, which would take too much time to fit within the time frame of the project, but certainly would prevent most bending from happening and therefore make the robot suitable for its task. Alternatively, only part of the arms could be machined into aluminum. This more cost and time-effective solution would still prevent a certain amount of bending in the arms under load, but the extent of the gain of this solution would be hard to predict.

Even though these solutions imply a greater cost, more fabrication time and also possibly more weight for the robot to carry, the change of material is almost unavoidable for the arms to bear the load from the servos and the weight of the robot during use. Adding more plastic to the 3D printed design wouldn't help sufficiently as the strength of the plastic is too low and there aren't any other 3D printing material available. However, the 3D printer used for this job was the $Formlabs1+$ available at the University of Ottawa, if the printing were to be made at another location where a significantly more rigid material would be available, then the arms could possibly be strong enough to bear the weight of the robot and the load from the servo motors through the worm gear mechanisms.

The design of the arm itself could be modified to improve is effectiveness and also its machinability. Especially since machining the arms from a denser, more rigid material is an almost unavoidable solution to create a functioning robot, having an easier to machine arm design would certainly be an advantage and design modifications to include a solution to other problems should be done as well. These design changes are shown on Figure 94.

(a) Original design (b) Modified design

Figure 94: Modifications on the arm design

The shape of the corner of the arm, labeled A and E has been changed to a less rounded shape to slightly increase rigidity, but mainly to provide a flat surface to drill the hole represented by letters C and G. This hole is to insert a threaded insert and a set screw to lock the worm gear in place during use to limit wear on the part and ensure the torque can be fully transmitted from the shaft to the arm. The rib B has been removed because it didn't provide any extra rigidity to the arm and would prove difficult to machine. On a similar note, the wheel end bracket D (H), has also been slightly modified to more even surfaces for easier machining in a subsequent iteration of the robot.

6.1.3 Assembly

The assembly of the robot differs from the original design in order to try to diminish some problematic situations. The main problems were that the material bent under the load and the worm gears produced significant forces in the axial direction as well as radial direction. The assembly was modified to alleviate these problems. The original design as well as the final assembly are shown side by side on Figure 95.

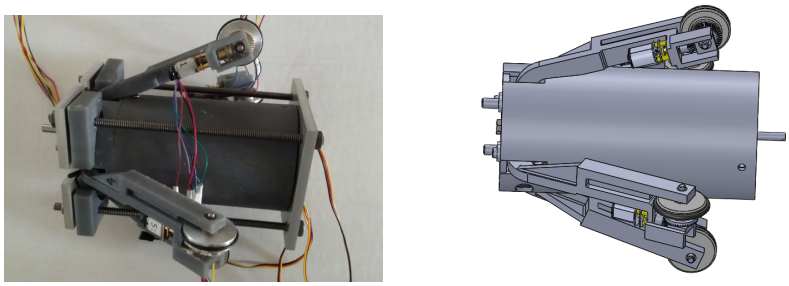

(a) Actual power module assembly (b) SolidWorks power module assembly

Figure 95: Difference between the original design and actual fabrication of the power module

Support flanges were added, along with threaded rods and a support plate at each end. Each of these components are shown on Figure 96.

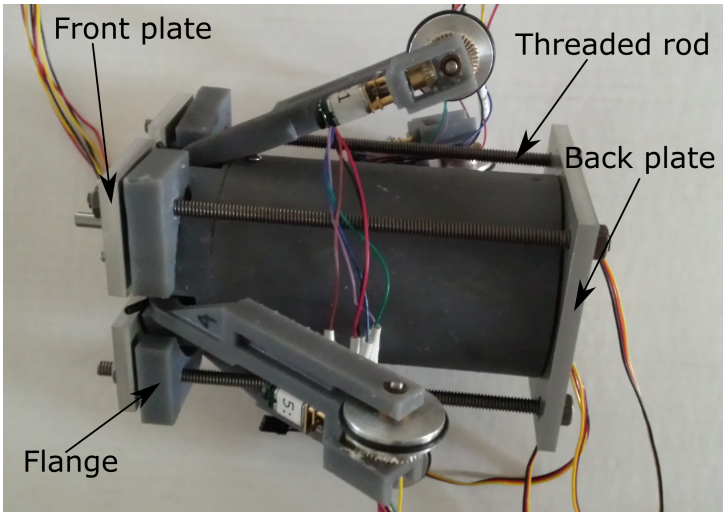

Figure 96: Actual assembly of the power module with labels

First, support flanges were added outside the front body housing where bending tended to occur during operation. These flanges had the sole purpose of adding rigidity to the front body housing part that was bending under load (Additional details about the support plates are given in Appendix D). These plates were resting on the worm gears at one end and the servo motors at the other end to prevent axial movement of the assembly during operation. However, the front body housing part still bent from the reaction forces from the worm gears because the plates did not prevent bending of the interior flanges.

6.1.4 Finite Element Analysis

First, finite element analysis of structural components should have been performed on the design. It has been done in other robotic designs discussed previously and the data gathered from the analyses were important in the validation of their model. In this experimental design, it would also have been beneficial to have at least an approximate value of stress inside the mechanical components of the robot. More specifically, the calculation of stresses and reaction forces acting on the support flanges and the arm joints would have helped determine the deflections that rendered the actual components unusable under typical operation conditions. Such analyses could have been performed with known softwares for finite element analyses such as Pro Engineer [59], ADAMS[57] or ANSYS[61].

In order to use a finite element analysis software efficiently, the efforts acting on various parts of the structure have to be estimated for worst case scenario of loading. The reaction forces acting on the structure are mainly caused by the worm shaft operated by the servo motor. The four worm shafts powering the arms are shown assembled on Figure 97.

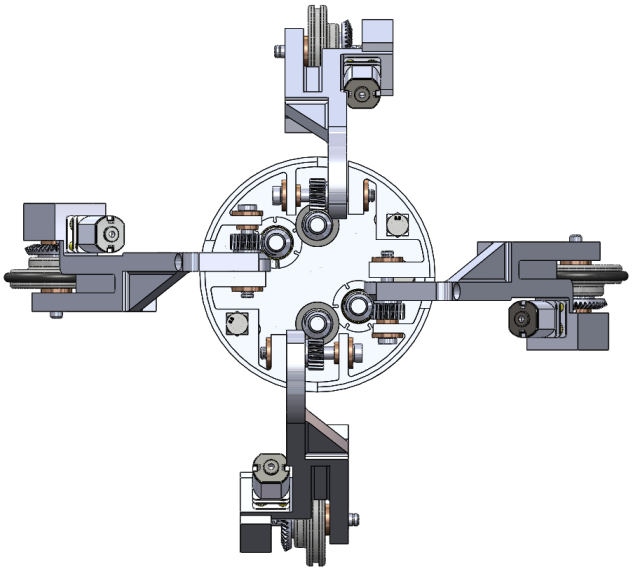

Figure 97: All worm shafts activating the wheels

As it was explained earlier, the parts of the robot most prone to bending and deflection were the main body support flanges that hold the shaft bushings and the arms. The

analysis of these two structures will be performed separately.

Body Analysis The body analysis consists of finding the reaction forces in the shaft support flanges due to the worm shafts. The leftmost mechanism of Figure 97 is zoomed in and seen from different angles to understand what and where are the acting forces in this assembly. This is shown on Figure 98.

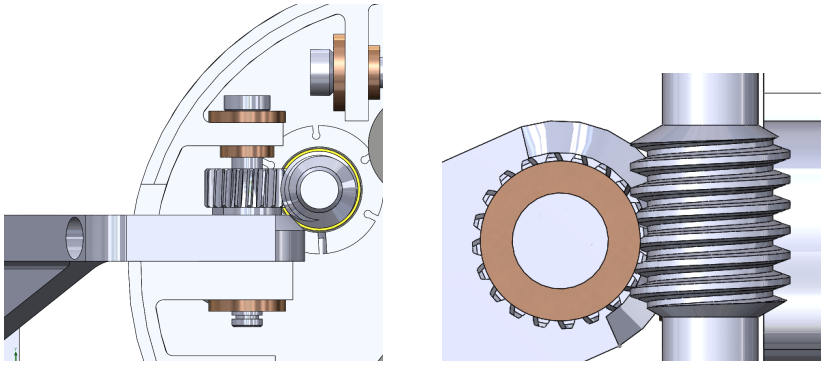

(a) Front view of a worm shaft mechanism

(b) Top view of a worm shaft mechanism

Figure 98: Worm shaft mechanism close up views

The same mechanism was sketched with the worm shaft and worm gear separated to show where the forces were acting. This type of gear assembly tends to create large axial, radial and tangential forces compared to other gear assemblies like helical gears. The forces are shown in Figure 99.

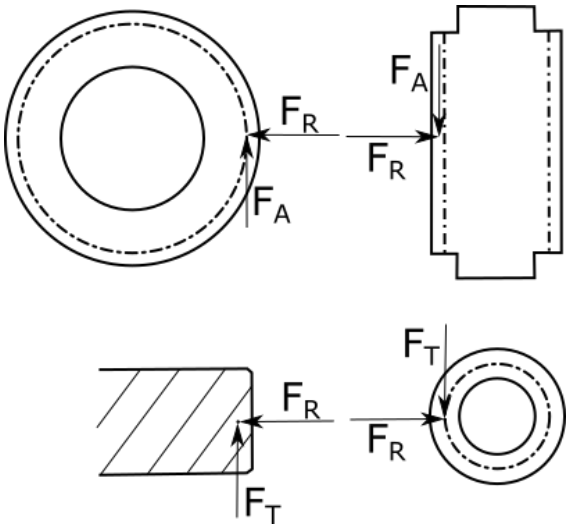

Figure 99: Sketch of the worm assembly to show acting forces

In Figure 99, the axial force F_A, the tangential force F_T and the radial force F_R are shown. The forces are in equal and opposite directions on the shaft and the gear. These forces are then transferred to the shaft supporting the worm gear. The efficiency of such a worm gear assembly should be somewhere between 0.5 and 0.6 [72], but assuming the largest efficiency should provide a factor of safety to the calculation. Figure 100 shows the reaction force on the shaft.

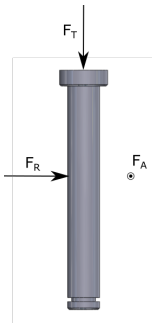

Figure 100: Reaction forces acting on the shoulder shaft

Since force F_A is from the worm gear that is allowed to freely rotate on the shaft, then only the friction force of the worm gear interior hole on the shaft is acting, but is negligible compared to other forces. The worm freely rotates on the shaft since the shaft is a support only and the worm gear is directly inserted into the arm, therefore the axial force F_A is directly propagated to the arm in its entirety. However, forces F_T and F_R act on the shaft. Actually, the shaft takes the entire load of these combined forces and transmits them to the robot body. The regions that takes the load are the flanges or tabs on the front part of the body and two tabs separate the loads evenly since the radial force F_R is acting at the middle section of the shaft. The free body diagram is shown on Figure 101.

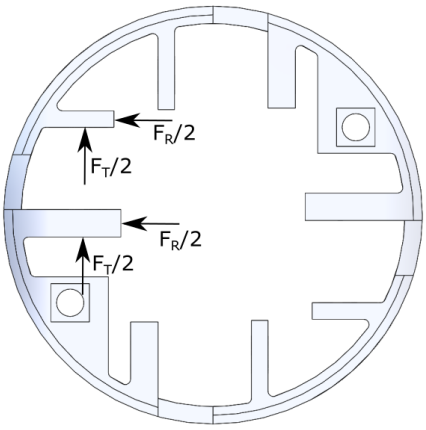

Figure 101: Reaction forces acting on the main body flange structures

In order to calculate the stresses and the deflection in the part that are induced by these forces, the only unknown left is the modulus of these forces. The tangential force F_T is given by the following equation[72] :

$$F_T = \frac{T}{P.R.}\eta$$

Where T is the motor torque of 0.4Nm, $P.R.$ is the pitch radius of the worm shaft of 0.0045m and η is the efficiency (0.6). The value for F_T is 53.33N. Similarly, F_R can be calculated the following way[72] :

$$F_R = F_T \frac{tan(\alpha_N)}{sin(\beta)}$$

Where α_N is the pressure angle of the worm (20°) and β is the lead angle of the worm (3.18°), which gives a value of 349.56N.

These values could in turn be used in finite element analysis calculations to know the stresses and deflections of the body support flanges. Images of this finite element analysis for the body in aluminum are shown on Figure 102.

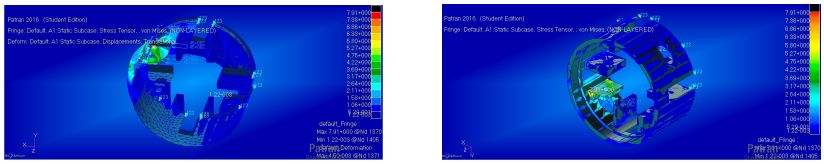

(a) FEA analysis of the body (front)

(b) FEA analysis of the body (back)

Figure 102: FEA analysis of the robot's main body component

This analysis performed in Adams gives a general idea of the stresses in the body at the most critical locations and the maximal stress value found for the part if it were made of aluminum to be 7.91 MPa which is well below the tensile strength of any aluminum which is around 275 MPa [70].

Arm Analysis A similar analysis should be performed on the arm as well because it is a critical component that has to support a big load from the motor and the weight of the robot itself. The worst case scenario for an arm would be the worm motor providing full torque to it while this arm is supporting the entire weight of the robot. An image of this situation is shown on Figure 103.

Where T is the worm gear torque, L is the length between the joints (0.111m), W is the weight of the robot (20N) and F is the reaction force from the pipe wall. The torque T can be calculated the following way:

$$\begin{aligned} T &= torque\ motor \times reduction\ ratio \times \eta \\ T &= 0.4Nm \times 10 \times 0.6 \\ T &= 2.4Nm \end{aligned}$$

Knowing T, the force F can be computed.

$$\begin{aligned} F &= W + \frac{T}{L} \\ F &= 20 + \frac{2.4}{0.111} \\ F &= 41.72N \end{aligned}$$

The force F is directly transferred to the shaft and then to the structure that supports the bushings and the shaft. The regions of the arm that support the loads are shown on Figure 104.

The R_{Torque} force is the reaction force of the torque from the worm gear acting on the surface drawn in red in Figure 104. The load is transferred to this face since the torque is transmitted from the worm gear with the use of a pin in the arm itself. The spring steel pin is considered rigid since its strength is much larger than the arm. The contact force from the wheel on the wall acts on the wheel shaft, which is then transferred to the region in red in Figure 104. This sketch is the loading scenario shown on Figure105.

Much like the previous analysis of the body, this finite element analysis of the arm is made under the assumption that the part is made of aluminum to test the structural integrity of the part under the worst case scenario of loading. In this case, the highest value of stress is 30.8 MPa, which is also below the tensile strength of the aluminum.

6.1.5 Other recommendations

Various other aspects of the design required some deeper thinking and some will be discussed here to avoid problems in subsequent designs and iterations of the robot or simply to improve on this proposed design. The main reason these recommendations are addressed in this section is that the overall design is discussed in details, but some important functions were the foundation of this robot and were not discussed earlier.

Simulation The simulation pipeline scenarios programmed for determining design parameters that produced the fewest number of collision were considered to be even and without any sort of defect. However, the next step in the simulation of the proposed robot design would be to redo the simulation including specific disturbances of the environment that could represent real life hazard for navigation. The defects to represent would be welding lips causing a bump on the surface, or a crevasse that could be caused by corrosion in the pipeline for example. These disturbances would make plausible navigation scenarios and would further prove the navigation capability of the robot in a pipeline environment.

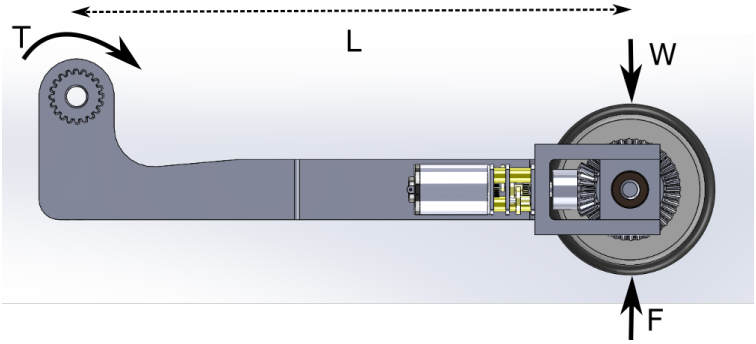

Figure 103: Forces acting on the arm structure

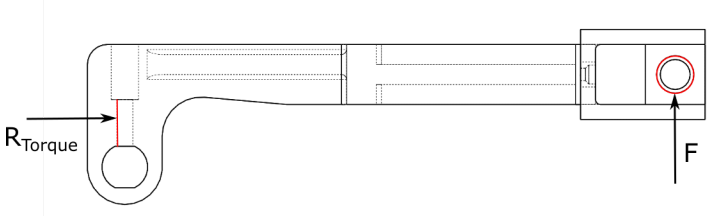

Figure 104: Regions supporting the load on the arm structure

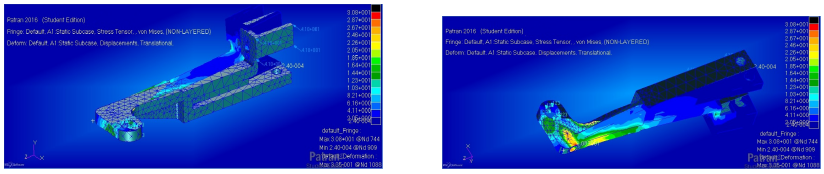

(a) FEA analysis of the arm (front)

(b) FEA analysis of the arm (back)

Figure 105: FEA analysis of the robot's arm

Sealing Then, sealing of various parts could be an important addition to the design as the robot might navigate in uncontrolled environments and encounter small particles, dust, liquids or humidity. Preventing these hazards from entering the casing or mechanisms of the robot could most likely lengthen the life of the components and the robot itself. In the current design, most components are enclosed, but some joints are not and should be protected, like the shoulder joint and the wheel motors' gearboxes.

Cable Management Also, cable management might be an issue with this robot design. Multiple wires have to be placed between actuated modules and other control and battery modules located at the rear of the robot. Cables would have to be drawn from the sealed end cap to these modules with enough flexibility to allow the modules to move with respect to one another, but not loose enough to entangle with the passive joints between each modules. Also, a slip ring would be necessary to allow the sensing module to rotate continuously without causing wire entanglement. Flat wire lines could be used to minimize wire bending in one direction and allow flexibility in another.

Data Gathering Moreover, data gathering has to be planned. The sensing module gathers data from its various sensors and could send the information directly through wires to an external memory located in another module. Then this external memory device could be removed for analyzing and replaced by a new one to continue pipe inspection with the robot. Likewise, the depleted battery module could also be replaced with another one with fresh batteries and sent to another pipeline for inspection. Meanwhile the depleted batteries could recharge until the next robot retrieval where they would be switched again.

Feedback Control Position feedback could be performed on the arm servo motors as well. This would provide information on the state of the arms during navigation, like the wheel motors. It would require more components and wires, but it would also provide more control over the arm movements.

Inertial Measurement Unit An inertial measurement unit could be added on another module. This component would give the orientation of the robot with respect to the Earth's gravity field by measuring acceleration in all direction as well as rotational acceleration. This device could provide additional information on the state of the robot during navigation.

7 Conclusions

The proposed robot design is made for travel in pipelines of diameters 6 to 8 in without any type of collisions for the five types of pipe configurations possible for standard pipelines. The proposed design can navigate and gather sensing data about the integrity of the pipeline for straight pipes, 90° bends, 135° bends, 180° bends and pipe diameter variations of 8 to 6 in. The robot is able to navigate continuously in these pipe configurations.

The robot could operate autonomously in these pipe configurations given that the pipeline has no pipe section different than the five discussed earlier. Data about the quality of the pipeline would be gathered at the end of an inspection with an external memory being retrieved from the robot to analyze.

The robot design has been optimized for three parameters to avoid collisions during pipe inspection. These parameters are the wheels' radius, the distance between shoulder joints and the trailer half-length between two modules. They are evaluated at 0.0125m, 0.03m and $0.4 * D_{Pipe}$ respectively.

Recommendations have been made for subsequent iterations of this robot design to allow for field experiment functionality. These recommendations range from structural design changes, material substitution, fabrication choices as well as other factors such as cable management, communication and components sealing.

Finally, it can be said that through various simulations and design parameter determination, an autonomous pipe inspection robot design has been proposed. This work shows the feasibility of the project and aims to be the ground work for another iteration of a similar pipe inspection robot.

References

[1] H. Liu. *Pipeline Engineering*. CRC Press, 2003.

[2] US Department of Transportation Pipeline and Hazardous Materials Safety Administration. Data and statistics. Website, December 2015. https://hip.phmsa.dot.gov/analyticsSOAP/saw.dll?Portalpages.

[3] L. Payne. Old pipelines likely to create additional problems. *Pipeline and Gas Journal*, 230:54–55, December 2003.

[4] S. Rimkevicius, A. Kaliatka, M. Valincius, G. Dundulis, R. Janulionis, A. Grybenas, and I. Zutautaite. Development of approach for reliability assessment of pipeline network systems. *Applied Energy*, 94:22–23, 2012.

[5] J. Yuan, X. Wu, Y. Kang, and C. Huang. Description of an inspection robot for long-distance transmission pipeline on-site overhaul. *Industrial Robot: An International Journal*, 36:546–550, 2009.

[6] Not available. Digital visual sidewall scanning: Streamlning collection and analysis of inspection data. *Pipeline and Gas Journal*, 237, 2010.

[7] P.D.V. Buschinelli, J.R. Melo, A. Albertazzi Jr., J.M.C.Santos, and C.S. Camerini. Optical profilometer using laser based conical triangulation for inspection of inner geometry of corroded pipes in cylindrical coordinates. 2013.

[8] K. Kawasue and T. Komatsu. Shape measurement of a sewer pipe using a mobile robot with computer vision. *International Journal of Advanced Robotic Systems*, 2012.

[9] R.M. Buehrer and S. Venkatesh. *Handbook of Position Location: Theory, Practice and Advances*. Jihn Wiley and Sons, Inc., 2012.

[10] B.H. Zhuang, W. Zhang, and D.Y. Cui. Noncontact laser sensor for pipe inner wall inspection. *Society of Photo-Optical Instrumentation Engineers*, 1998.

[11] A. J. Lynch. Magnetic flux leakage robotic pipe inspection: Internal and external methods. 2009.

[12] X.L. Jiang, Y.F. Xia, J.L. Hu, F.H. Yin, C.X. Sun, and Z. Xiang. Optimal design of mfl sensor for detecting broken steel strands in overhead power lines. *Progress in Electrmagnetic Research*, 121:301–315, 2011.

[13] M. Beller. Pipeline inspection utilizing ultrasound technology: On the issue of resolution. Technical report, Pigging Products and Services Association, 2007.

[14] Sharp Corporation. Gp2y0ah01k0f sharp sensor. Website, Avril 2007.

[15] G. Bright, D. Ferreira, and R. Mayor. Automated pipe inspection robot. *Industrial Robot*, 24(4):285–289, 1997.

[16] Y. Zhang and G. Yan. In-pipe inspection robot with active pipe-diameter adaptability and automatic tractive force adjusting. *Mechanism and Machine Theory*, 42:1618–1631, 2007.

[17] T. Oya and T. Okada. Development of a steerable, wheel-type, in-pipe robot and its path planning. *Advanced Robotics*, 19(6):635–650, 2005.

[18] A. Kakogawa and S. Ma. Stiffness design of springs for a screw drive-in-pipe robot to pass through curved pipes and vertical straight pipes. *Advanced Robotics*, 26:253–276, 2012.

[19] D. Lee, J. Park, D. Hyun, G. Yook, and H. Yang. Novel mechanism and simple locomotion strategies for an in-pipe robot that can inspect various ipe types. *Mechanism and Machine Theory*, 56:52–68, 2012.

[20] N.S. Roslin, A. Anuar, M.F.A. Jalal, and K.S.M. Sahari. A review: Hybrid locomotion of in-pipe inspection robot. *Procedia Engineering*, 41:1456–1462, 2012.

[21] V. Artigue and M. Pascal. A new method for path planning of an in-pipe inspection robot. *Procedings of DETC'03 ASME 2003 Design Engineering Technical Conferences and Computers and Information in Engineering Conference*, 2003.

[22] M. Horondinca, I. Doroftei, E. Mignon, and A. Preumont. A simple architecture for in-pipe inspection robots. Technical report, Université Libre de Bruxelles, Brussels, Belgium, 2000.

[23] S.M. Ryew, S.H. Baik, K.M. Jung, S.G. Roh, and H.R. Choi. Inpipe inspection robot robot system with active steering mechanism. *Procedings of the 2000 IEEE/RSJ International Conference on Intelligent Robots and Systems*, 2000.

[24] K.U. Scholl, V. Kepplin, K. Berns, and R. Dillmann. Controlling a multijoint robot for an autonomous sewer inspection. *Procedings of the 2000 IEEE International Conference on Intelligent Robots and Systems*, 2000.

[25] H. Sarfraz. Kinematics and optimal control of a mobile parallel robot for inspection of a pipe-like environments. 2014.

[26] O. Tatar, D. Mândru, and I. Ardelean. Development of mobile robot minirobots for in-pipe inspection tasks. *MECHANIKA*, 2007.

[27] H.M. Kim, J.S. Suh, Y.S. Choi, T.D. Tring, H. Moon, J. Koo, S. Ryew, and H.R. Choi. An in-pipe robot with multi-axial differential gear mechanism. In *IEEE/RSJ International Conference on Intelligent Robots and Systems*, Tokyo, Japan, November 2013.

[28] D.-W. Kim, C.-H. Park, H.-K. Kim, and S.-B. Kim. Force adjustment of an active pipe inspection robot. In *ICROS-SICE International Joint Conference*, Fukuoka, Japan, August 2009.

[29] 22nd Internationial Syposium on Automation and Robotics in Construction, editors. *Design, Modeling and Prototyping of a Pipe Inspection Robot*, Ferrara, Italy, September 2005.

[30] Y.-S. Kwon and B.-J. Yi. Design and motion planning of a two-module collaborative indoor pipeline inspection robot. *IEEE Transaction on Robotics*, 28(3), June 2012.

[31] G. Granosik. Hypermobile robots - the survey. *J. Intell Robot Systems*, 75:147–169, 2014.

[32] P.D. Spanos, R.B. Berka, and P. Tratskas. Multisegment large space robot: Concept and design. *Journal of Aerospace Engineering*, 13:123–132, October 2000.

[33] K.J. Kyriakopoulos, G. Migadis, and K. Sarrigeorgidis. The ntua snake: Design, planar kinematics and motion planning. *Journal of Robotic Systems*, 16:37–72, 1999.

[34] R. Baker, D. Driscoll, G. Vradis, and H. Schempf. A new tool for long-range visual inspection of live gas mains. *GasTIPS*, 2005.

[35] A. Percy, I. Spark, Y. Ibrahim, and L. Hardy. A numerical control algorithm for navigation of an operator-driven snake-like robot with 4wd-4ws segments. *Robotica*, 29:471–482, 2010.

[36] T. Miyagawa and N. Iwatsuki. Characteristics of an in-pipe mobile robot with wheel drive mechanism using planetary gears. In *IEEE International Conference on Mechatronics and Automation*, Harbin, China, August 2007.

[37] S. Hirose, H. Ohno, T. Mitsui, and K. Suyama. Design of a in-pipe inspection vehicle for 25, 50, 150 diameters pipes. In *International Conference on Robotics and Automation*, Detroit, Michigan, USA, May 1999.

[38] G. Legnani and R. Faglia. Harmonic drive transmissions: the effects of their elasticity, clearance and irregularity on the dynamic behaviour of an actual scara robot. *Robotica*, 10:369–375, 1992.

[39] T. Marilier and J.A. Richard. Non-linear mechanic and electric behavior of a robot axis with a harmonic-drive gear. *Robotics and Computer-Integrated Manufacturing*, 5:129–136, 1989.

[40] D. Vassileva, Y. Kiyosawa, and M. Suzuki. Sensorless torque control for a robot with harmonic drive reducers. *Mechanics Based Design of Structures and Machines*, 39:253–267, 2011.

[41] Z. Shi, Y. Li, and G. Liu. Adaptive torque estimation of robot joint with harmonic drive transmission. *Mechanical Systems and SIgnal Processing*, 96:1–15, 2017.

[42] T. Okada and T. Sanemori. Mogrer: A vehicle study and realization for in-pipe inspection tasks. *IEEE Journal of Robotics and Automation*, 3(6), 1987.

[43] J. Park, D. Hyun, W.-H. Cho, T.-H. Kim, and H.-S. Yang. Normal-froce control for an in-pipe robot accordig to the inclination of pipelines. *IEEE Transaction on Industrial Electronics*, 58(12), December 2011.

[44] Y.-S. Kwon, B. Lee, I.-C. Whang, and B.-J. Yi. A pipeline inspection robot with a linkage type mechanical clutch. In *IEEE/RSJ International Conference on Intelligent Robots and Systems*, Taipei, Taiwan, October 2010.

[45] P. Li, S. Ma, B. Li, and Y. Wang. Development of an adaptive mobile robot for in-pipe inpection task. In *IEEE International Conference on Mechatronics and Automation*, Harbin, China, August 2007.

[46] A. Kakogawa and S. Ma. Stiffness design of springs for a screw drive in-pipe robot to pass through curved pipes and vertical straight pipes. *Advanced Robotics*, 26:253–276, 2012.

[47] Y.-C. Chang and Y. Yamamoto. On-line path planning strategy integrated with collision and dead-lock avoidance schemes for wheeled mobile robot in indoor environments. *Industrial Robot: An International Journal*, 35:421–434, 2008.

[48] Y.Y. Lwin and Y. Yamamoto. Obstacle-responsive navigation scheme of a wheeled mobile robot based on look-ahead control. *Industrial Robot: An International Journal*, 39:282–293, 2012.

[49] H.J. Zhang, J.W. Gong, Y. Jiang, G.M. Xiong, and H.Y. Chen. An iterative linear quadratic regulator based trajetory tracking controller for a wheeled mobile robot. *Journal of Zheijiang University*, 13:593–600, 2012.

[50] M. Hoy. A method of boundary following by a wheeled mobile robot based on sampled range information. *International Journal of Robotic Systems*, 72:463–482, March 2013.

[51] N.B. Hui and D.K.Pratihar. Soft computing-based navigation schemes for a real wheeled robot moving among static obstacles. *International Journal of Robotic Systems*, 51:333–368, 2008.

[52] A.V. Savkin and M. Hoy. Reactive and shortest path navigation of a wheeled mobile robot in cluttered environments. *Robotica*, 31:323–330, 2013.

[53] Y. Kim and B.K. Kim. Efficient time-optimal two-corner trajectory planning algorithm for differential-driven wheeled mobile robots with bounded motor control inputs. *Robotics and Autonomous Systems*, 64:35–43, 2015.

[54] L.Lapierre, R. Zapata, and P. Lepinay. Combined path-following and obstacle avoidance control of a wheeled robot. *The International Journal of Robotics Research*, 26:361–375, April 2007.

[55] D. Vishal and P.V. Manivannan. Multi-body dynamics simulation and gait pattern analysis of a bio-inspired quadruped robot for unstructured terrains using adaptive stroke length. *Artif Life Robotics*, 21:493–499, August 2016.

[56] M.H. Korayem and H. Ghariblu. Analysis of wheeled mobile flexible manipulator dynamic motions with maximum load carrying capacities. *Robotics and Autonomous Systems*, 48:63–76, July 2004.

[57] MSC Software. Adams. Website http://www.mscsoftware.com/product/adams, .

[58] C.K. Woo, H.D. Choi, S. Yoon, S.H. Kim, and Y.K. Kwak. Optimal design of a new wheeled mobile robot based on a kinematic analysis of the stair climbing states. *International Journal of Robotic Systems*, 49:325–354, March 2007.

[59] PTC Software. Creo/pro-engineer. Website http://www.ptc.com/cad/pro-engineer, .

[60] D. Zhang, Z. Li, and J. Chen. Design and optimization of an omnidirectional permanent-magnetic wheeled wall-climbing microrobot with mems-based electromagnetic micromotors. *Advanced Robotics*, 26:197–218, April 2012.

[61] ANSYS Inc. Ansys. Website http://www.ansys.com/.

[62] L.Yang, L. Qimin, and L. Zhangxing. Design and optimization of wheeled-legged robot: Rolling-wolf. *Chinese journal of mechanical engineering*, 27, 2014.

[63] A. Siravuru, S.V. Shah, and K. M. Krishna. An optimal wheel-torque control on a compliant modular robot for wheel-slip minimization. *Robotica*, 35:463–482, 2017.

[64] MathWorks. Matlab. Websitehttps://www.mathworks.com/products/matlab.html.

[65] L. Douadi, D. Spinello, and W. Gueaieb. Dynamics and control of a planar multibody mobile robot for confined environment inspection. *Journal of Computational and Nonlinear Dynamics*, 10, January 2015.

[66] L. Douadi, D. Spinello, W. Gueaieb, and H. Sarfraz. Planar kinematics analysis of a snake-like robot. *Robotica*, 32(5):659–675, August 2014.

[67] Canadian Energy Pipeline Association. Canada's undergroupd pipeline network. Website, March 2016. http://www.cepa.com/about-pipelines/types-of-pipelines.

[68] C.Maier. Meeting the chaleenges facing small-diameter combination inspection. *Pipeline and Gas Journal*, 234:42–43, August 2007.

[69] Alberta Energy Regulator. Report 2013-b: Pipeline performance in alberta. Technical report, Alberta Energy Regulator.

[70] E. Oberg, F.D. Jones, H.L. Horton, and H.H. Ryffel. *26th edition Machinery's Handbook*. Industrial Press, 2000.

[71] ANSI. Welded and seamless wrought steel pipes asme/ansi b36.10/19. Website, March 2016.

[72] J.-L. Fanchon. *Guide des sciences et technologies industrielles*. afnor editions/Nathan, 2009.

[73] S. Goudreau and J.-P. Marier. *Notes de cours de Dessin de Machines*. Université Laval, 2012.

[74] Akron Bearing Company. Akron bearing. Website, October 2015. http://www.akronbearing.com/gears/.

[75] University of South Florida. Florida center for instructional techology. Website, October 2015. http://etc.usf.edu/.

[76] TravTigerEE. Cc by-sa 3.0. Own Work, May 2016. https://commons.wikimedia.org/w/index.php?curid=24278627.

[77] J.M. Mirats Tur and W. Garthwaith. Robotic devices for water main in-pipe inspection: A survey. *Journal of Field Robotics*, 27(4):491–508, 2010.

[78] P. Salameh. Limb design for salamander and centipede robots. Technical report, École Polytechnique Fédérale de Lausanne, January 2011.

[79] H. Lin, G.G. Leisk, and B. Trimmer. Goqbot: a caterpillar-inspired soft-bodied rolling robot. *IOP Publishing*, 2011.

[80] P. Liljebäck, K. Pettersen, O. Stavdahl, and T. Gravdahl. Controllability and stability analysis of planar snake robot locomotion. *IEEE Transaction on Automation Control*, 56(6), June 2011.

[81] P. Liljebäck, K. Pettersen, O. Stavdahl, and T. Gravdahl. Experimental investigation of obstacle-aided locomotion with a snake robot. *IEEE Transaction on Automation Control*, 27(4), August 2011.

[82] B. Klaasen and K.L. Paap. Gmd-snake2: A snake-like robot driven by wheels and a method for motion control. *Proceedings of 1999 International Conference on Robotics and Automation IEEE*, 1999.

[83] H. Wei, Y. Cui, H. Li, J. Tan, Y. Guan, and Y. Li. Kinematics and implementation of a modular caterpillar robot in trapezoidal wave locomotion. *International Journal of Advanced Robotics Systems*, June 2013.

[84] L. Xiaopeng, M. Hongwei, L. Weijian, and W. Chuanwei. Research on the posture kinematics model of multi-joint caterpillar robot and its motion control. *Applied Mechanics and Materials*, 52-54, March 2011.

[85] A. Akbarzadeh and H. Kalani. Design and modeling of a snake robot based on work-like locomotion. *Inernational Journal of Advanced Robotics*, 26:537–560, 2012.

[86] S. Wakimoto, J. Nakajima, M. Tanaka, T. Kanda, and K. Suzumori. A micro snake-like robot for small pipe inspetion. Technical report, Okayama University, 2003.

[87] S. Wakimoto, M. Tanaka, and K. Suzumori. A miniature inspection robot negociating pipes of widely varying diameter. Technical report, Okayama University, 2003.

[88] A.S. Boxerbaum, K.M. Shaw, H.J. Chiel, and R.D. Quinn. Continuous wave peristaltic motion in a robot. *Inernational Journal of Robotics Reasearch*, 31: 302–318, 2012.

Appendix A

Mechanical Components Theory

Gears and Gear Trains

A gear is a cylindrical mechanical part with teeth destined to transmit power. Whereas a gear train is the assembly of at least two gears[72, 70, 73]. Gears may vary in style, depending on the configuration of the assembly. Two types of gears will be explored here: spur gears and bevel gears.

Spur Gears Spur gears are probably the most common type of gears. They are cylindrical and designed to transmit power through parallel shafts. They can be made out of many different materials, have different pitch angles, number of teeth and can obviously have different diameters.

Figure 106: Spur gear train example [74]

In Figure 106, the smaller gear is the driving gear, or pinion and the larger gear is the driven gear. The number of teeth or diameter of the spur gears is generally the most important data to acquire for a specific gear train, since it will dictate the gear ratio. It's especially useful in electronic applications where motors usually have high rotating speeds and need to have a speed reducer. The gear ratio is calculated the following way[70]:

$$m_G = \frac{N_G}{N_P} \tag{22}$$

where m_G is the gear ratio, N_G is the number of teeth on the gear and N_P is the number of teeth on the pinion. In order to get the output speed and the output torque, the ratio would be used like this:

$$\omega_{out} = \frac{\omega_{in}}{m_G} \tag{23}$$

$$\tau_{out} = \tau_{in} m_G \tag{24}$$

Bevel Gears Bevel Gears are conical gears that transmit power through intersecting or offset shafts. They are shown on Figure 107.

Figure 107: Bevel gear train example [75]

Though these gears can also vary a lot in fabrication details, typical straight bevel gears as shown on Figure 107 have their gear ratio calculated the same way as regular spur gears. Only the mounting is different. They are very useful when the axis of rotation has to be shifted 90°.

Wheels and slippage

When a wheel turns, it can be in two different types of motion: rolling without slip or rolling with slip. Depending on various parameters, a powered wheel can change from one state to the other. In the simplest case of a wheel resting on a flat horizontal surface receiving an input torque, the wheel can either start slipping with respect to the group and rotate on itself or it can start rotating slower and also move forward. With constant wheel size, normal force and coefficient of friction between the wheel and the ground, the wheel will slip if it receives an input torque greater than a certain threshold and roll if it is below the same value. To find this threshold, a free body diagram is necessary. It is presented on Figure 108.

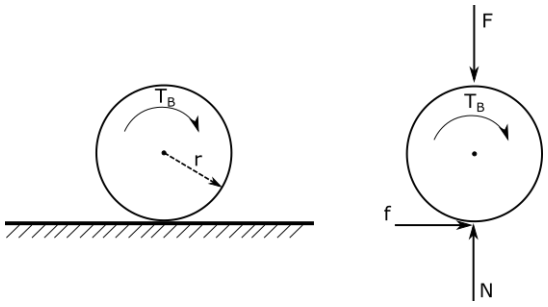

Figure 108: Free body diagram of a wheel on a flat surface

In this simple case, the force F represent the force pushing the wheel on the ground, being its weight or some outside force. The input torque is denoted T_B, the normal force is N and the friction force is f. In this case, without actual numbers, it's impossible to know if the wheel will slip. However, it can be determined analytically, because

it is known that the friction force varies with the torque, but only up to a certain torque value. This is mainly because the friction force f is the only force counteracting the torque T_B. The force f is determined by:

$$f = \mu N$$

Where μ is the coefficient of static friction between the wheel and the ground. Also, taking the sum of moment around the wheel center of radius r:

$$\begin{aligned} T_B &= f \cdot r \\ T_B &= \mu \cdot N \cdot r \end{aligned}$$

However, this friction has an upper limit that is bound by the coefficient of friction mentioned earlier. So if T_B becomes higher than the maximum value of f times r, then the friction force cannot compensate for the torque and the wheel slips. It can be represented mathematically by the following:

$$\begin{aligned} T_B &\geq \mu \cdot N \cdot r(\text{It slips}) \\ T_B &< \mu \cdot N \cdot r(\text{It doesn't slip}) \end{aligned}$$

It is represented on the following figures. First the situation in which the torque T_A is greater than the threshold value on Figure 109.

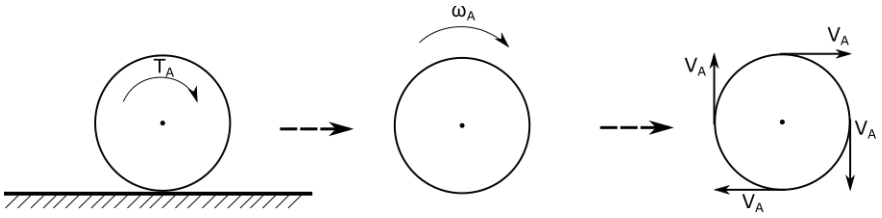

Figure 109: Sketch of a wheel slipping on a flat surface

Then the situation where the wheel doesn't slip is shown on Figure 110. In this scenario, the torque T_B is lower, below the threshold, and therefore the wheel doesn't slip, meaning the total velocity of the point of contact of the wheel with the ground is 0. As the figure shows, the combination of of rotational and translational velocities is the reason why the velocity at the point of contact is 0.

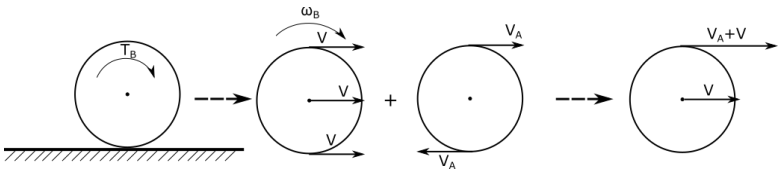

Figure 110: Sketch of a wheel slipping on a flat surface

Appendix B

In this section, the possible range of motion for each arm will be calculated experimentally. Though the results are taken from the SolidWorks model, it gives a good idea of the actual range of motion of the actual robot. It is actually calculated by checking the necessary range of motion for the arms to travel in a minimum sized pipeline to a maximum sized pipeline. Figure 111 shows the minimum angle of the arms with respect to the body for a 6 in pipeline.

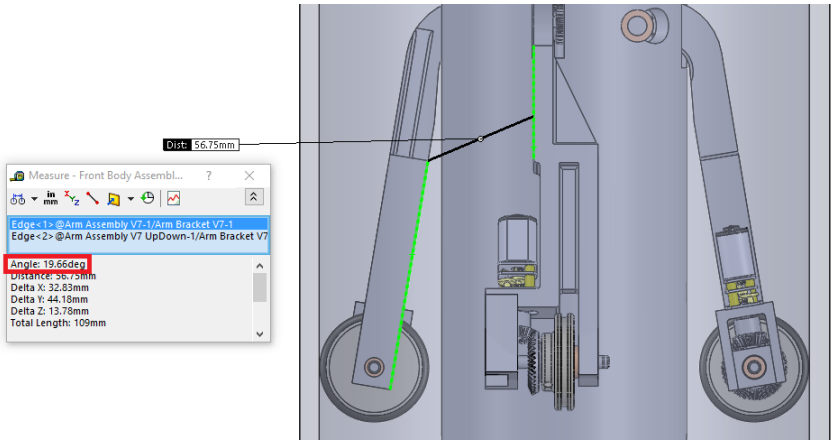

Figure 111: Angle of the arms in a 6in pipeline

The value of the angle is shown in the red rectangle in the figure and is 19.66°. Similarly, the maximum angle of the arm in a 8 in pipeline can be found. It is shown on Figure 112.

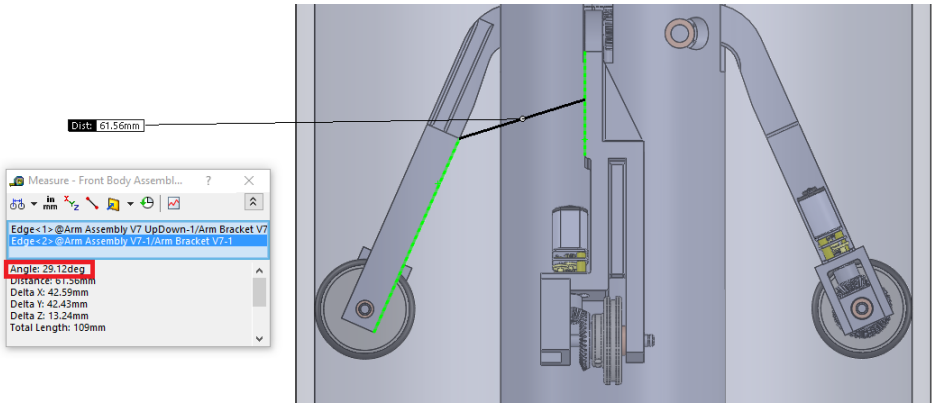

Figure 112: Angle of the arms in a 8in pipeline

The value of the angle in the red rectangle is 29.12°.

The range of motion(rom) is then found with the following calculation:

$$\begin{aligned} rom &= \text{max. angle} - \text{min. angle} \\ rom &= 9.46 \end{aligned}$$

Also, knowing that between the servos and the arms, there is a worm gear with a reduction ratio of 10, the servo has to rotate by at least 94.6°.

Appendix C

In this section, the various simulation results are presented by simulation scenario.

Straight Pipe

First of all, Figure 113 shows the constant angle of the arms throughout the pipe, as expected.

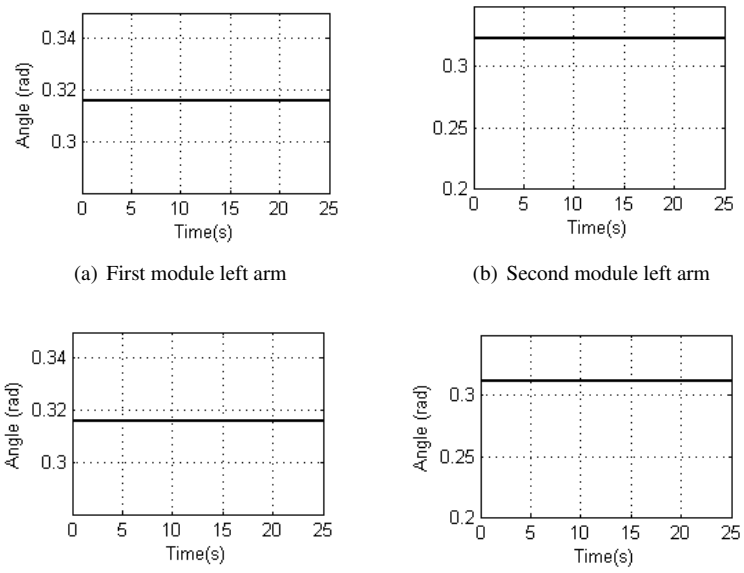

(a) First module left arm

(b) Second module left arm

(c) First module right arm

(d) Second module right arm

Figure 113: Angle of the arms of the two powered modules during travel in a straight pipe

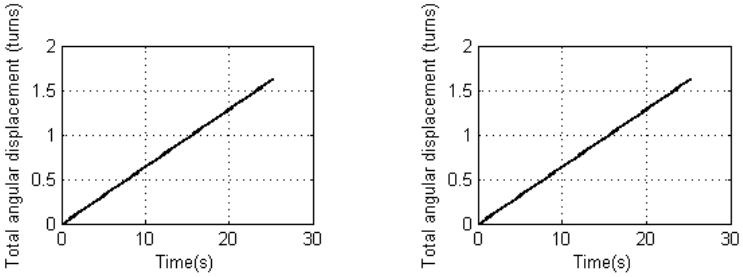

(a) First module left arm

(b) Second module left arm

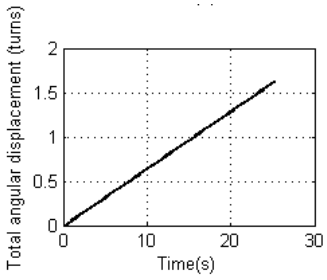

(c) First module right arm

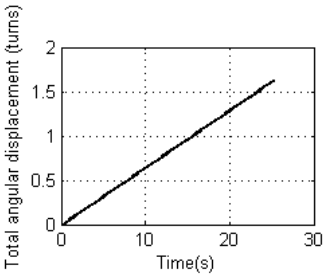

(d) Second module right arm

Figure 114: Angular position of the wheels of the two powered modules during travel in a straight pipe

Then, Figure 114 shows the constant progression of the wheels position, while Figure 115 shows the steady wheels' speeds. Again here, everything as expected of the robot since the pipe section and curvature remains the same at all times.

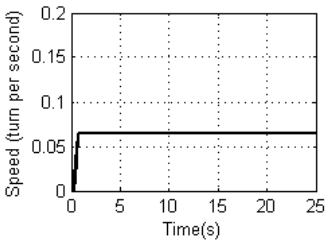

(a) First module left arm

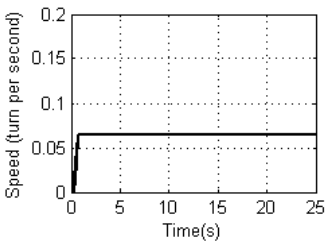

(b) Second module left arm

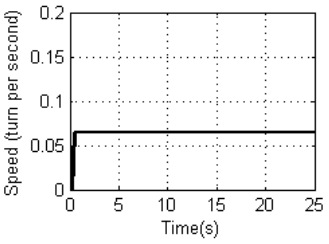

(c) First module right arm

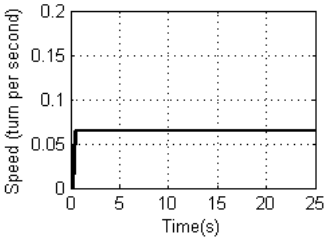

(d) Second module right arm

Figure 115: Angular speed of the wheels of the two powered modules during travel in a straight pipe

Changing Pipe Diameter Section

This subsection presents the angular position of the wheels during travel in a pipe of varying diameter.

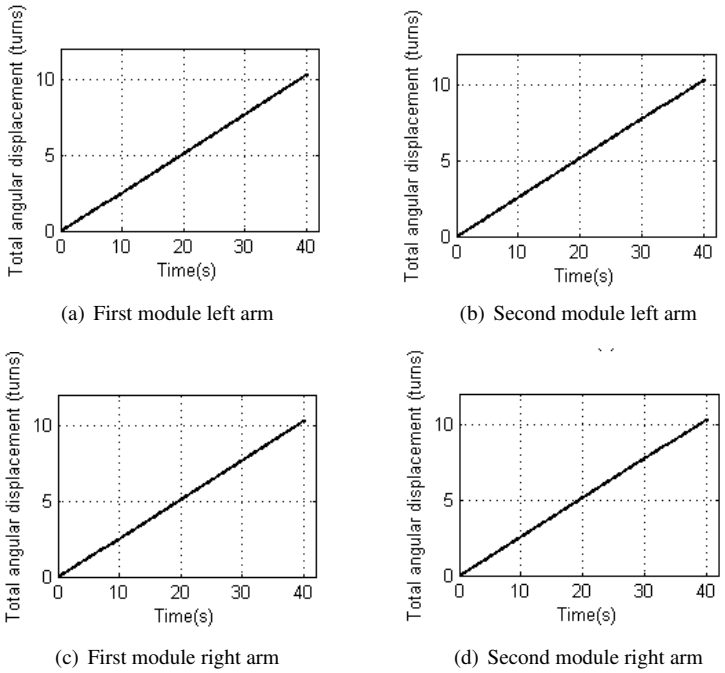

(a) First module left arm

(b) Second module left arm

(c) First module right arm

(d) Second module right arm

Figure 116: Angular position of the wheels of the two powered modules during travel in a pipe of reducing diameter (8 to 6 in)

Figure 116 doesn't provide much new information, the robot stays at a relatively constant speed throughout the pipeline, so the wheels rotate a similar number of turns.

Appendix D

In this section, additionnal details about the support plates located at both ends of the fabricated robot are given.

Flanges were 3D printed and were supported by threaded rods. However, to hold these rods, two supporting plates had to be machined. The front supporting plate resting on the worms to prevent them from moving axially and the back plate supporting the back of the servos at the other end. The supporting plates are shown on Figure 117.

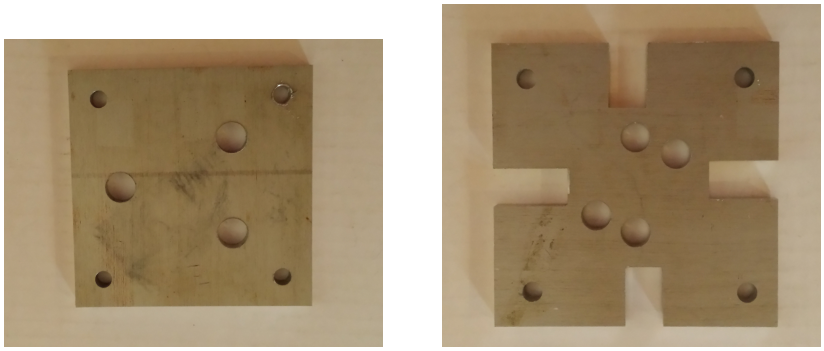

(a) Robot's back plate (b) Robot's front plate

Figure 117: The robot's two supporting plates

The back plate has three holes in it to allow all the internal wires of the robot to pass through and connect to another module. The front plate also has four holes in it, but they are machined with precision to fit bushings that will support the four servo shafts. The indentations in the front plate are to avoid interference with the arms.

Appendix E

The prototype powered module has servo motors and gearmotors and have different control parameters. To consolidate the communication between Matlab and the drive mechanisms, an Arduino Mega board was used. This controller has the ability to control multiple devices on various channels through a COM port on a computer.

Servo Motors

Servo motors are manufactured to be easy to control. They require only a single line of code on an arduino to reach a certain angle and they stay at the specified angle until a different command is input. This way, the arm angle simulation results obtained previously could be compiled and read without alteration to control the robot in an experiment.

DC Gear Motors

DC motors are controlled differently than servo motors, their rotation speed is proportional to the voltage input. Similarly to the servo motors, the speed of each DC gear motor has been found during the simulations. This gathered data is the target for each gear motor. However, gear motors require controllers to adjust their speeds and minimize the error with the desired value and a PID controller was used for this task. The details of the PID controller is presented next.

PID Controller

There are three components to a PID controller. Each component's value is added to the error signal in order to minimize the error and be as close to the desired signal as possible. There is a proportional (P), integral (I) and derivative (D) portion that have various effects on the output. A typical representation of this closed loop system is shown on Figure 118.

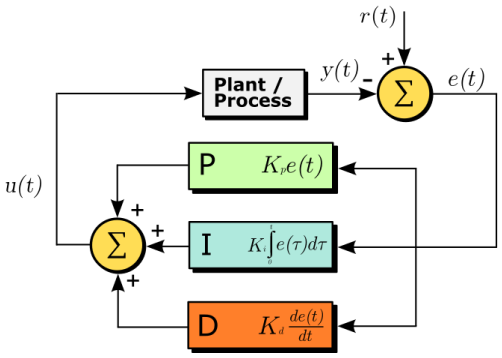

Figure 118: Graphical representation of a PID controller [76]

Controller Results

The PID controller was coded into a $Matlab$ program to find desirable values for the gains. The desired speed curve was built to give smooth acceleration and deceleration and encoders were wired and placed on the motors to get their speeds. The goal was to get the motors to rotate at the desired input speed as fast as possible while minimizing the error between the input and the output. The results for the four wheels are presented in the graphs of Figure 119 and 120.

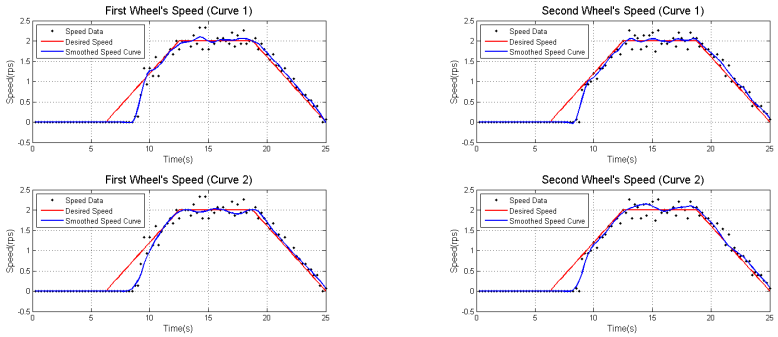

(a) Control of wheel 1

(b) Control of wheel 2

Figure 119: Speed PID control of wheels 1 and 2

These tests were performed without any load on the wheels to tune the PID controller. The red trapezoidal curve represents the desired speed for each motor. A trapezoidal shape was used as desired speed curve because it represents acceleration, constant speed and deceleration and is a simple test curve for the motors. The graphs show

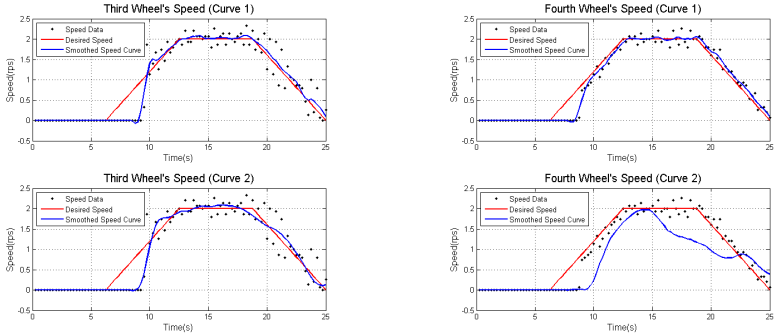

(a) Control of wheel 3

(b) Control of wheel 4

Figure 120: Speed PID control of wheels 3 and 4

two curves in blue for each wheel. Each curve represents the same data, smoothed by a different algorithm.

The gathered data mostly stayed within $\pm 10\%$ of the desired value, but all graphs showed lag at the beginning. The explanation for this lag is that the signal sent to the motor through the controller is a fraction of the maximum voltage that the controller can direct to the motors. However, when this voltage value is below a certain threshold, there is no wheel rotation because of internal resistance and friction.

After the approximately three second lag period, the data points tend to stay near the desired red curve without overshoot. During deceleration, the linear transition period from constant speed to complete stop prevents this lag from occurring.

Appendix F

Multiples means of locomotion for robots exist. They are grouped in two main subsections: Biologically inspired robots and wheeled robots. The following sections describe the most common robot designs and mechanisms for pipe inspection. Some of the discussed means of locomotion are presented in Figure 121.

Biologically inspired robots have the major advantage of being able to navigate in a multitude of different environments. For instance, a legged robot can walk on uneven and rough terrain where a wheeled robot would surely stall. Some biologically inspired robot can even be amphibious [78]. Some robots use very original means of locomotion to overcome real world obstacles based on real world fauna [79, 80, 81, 82], but they do so at the expense of more energy consumption or without total control over the locomotion. Wheeled robots are less suited for rugged terrain, but are more efficient and more easily controlled.

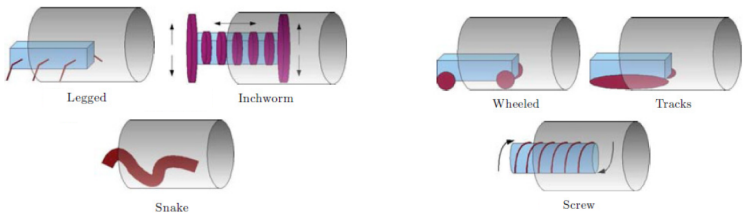

(a) Biologically inpired robots (b) Wheeled robots

Figure 121: Different means of locomotion for a pipe inspection robot [77]

Vehicle robots tend to be inherently more stable compared to biologically inspired robots. Also, biologically inspired robots may have alternating motion of their centers of gravity during locomotion which can be problematic while retrieving data.

Biologically Inspired Robots

The robot locomotion styles that are inspired by nature are of different types, but are mainly grouped into four categories: caterpillar [79, 83, 84] , centipede [78], snake [80, 81, 85, 86, 87, 82] and worm [85, 88].

Caterpillar Robots For the caterpillar-like robots models, there is variety in how the robots are designed to move. A model uses four arms for locomotion [84] while another type of model is moved by a trapezoidal wave across it's body[83]. An example is a robot with four independent track systems and it is shown on Figure 122.

This model is specifically designed to address complex and difficult terrain situations while retaining traditional motion mechanisms[84]. It is an attempt at having a stable robot on uneven ground and still using wheels and tracks along with arms. Another design that draws heavy inspiration from the caterpillar is the one shown on Figure 123.

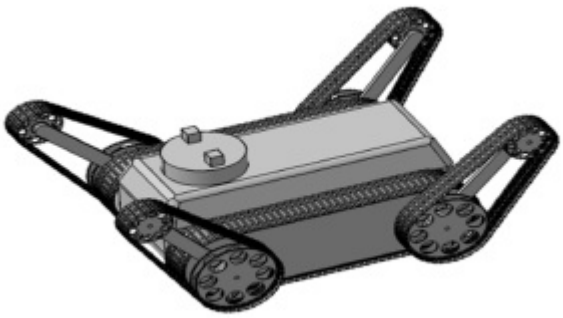

Figure 122: A tracked and arm-bearing caterpillar robot [84]

Figure 123: A trapezoidal wave driven caterpillar robot [83]

In this figure it is possible to see the proposed design through many different steps of its motion mechanism. This specific gait has been proven to be inherently more stable for a five joint robot and also provides good clearance for obstacles across rugged terrain [83].

The caterpillar design offers good maneuverability on rugged terrain at the expense of energy consumption. This design is also inherently slow and therefore is not suited for long distance inspection. Moreover, a pipeline is a semi-controlled environment where the walls are expected to be mostly free of major defects or obstacles, which this design is typically expected to face.

Centipede Robots Another type of locomotion inspired by nature that require the use of legs is the centipede robot [78], as seen on Figure 124. In this design, a long slender body is pushed forward by multiple sets of similar legs, like the design shown on Figure 124 a). It is also similar to the salamander limb design in the same article that has multiple body segments, but only some have legs for locomotion. This design can be seen on Figure 124b). Not unlike the caterpillar models discussed earlier, this design performs well on rough, uneven surfaces. Which is usually not the case for pipes. Also, again similarly to the previous design, legged robots tend to be less energy efficient.

(a) A centipede robot [78]

(b) A salamander robot [78]

Figure 124: 2 Multiple-body robots with multiple sets of legs

Worm Robots One more seldom seen type of robot locomotion is the inchworm locomotion. [85, 88] This mean of transportation is either a multi-body robot that moves by making a sinusoidal wave across its central axis very much like the caterpillar robots discussed earlier[85], or the robot uses peristaltic motion. [88] In peristaltic motion, some parts of the body of the robot slide in and out of each other in sequence to induce movement like an earthworm. This design allows movement of the robot on many different surfaces and terrain. However, the irregular motion of the robot inhibits fast linear speeds, hence it is not ideal for traveling long distances either. This type of motion can also complicate data acquisition. However, this type of robot is inherently very

stable. It is shown at four different steps of it's motion over one second on Figure 125. The robot is shown moving to the right as the extended body parts that touch the ground are moved to the left.

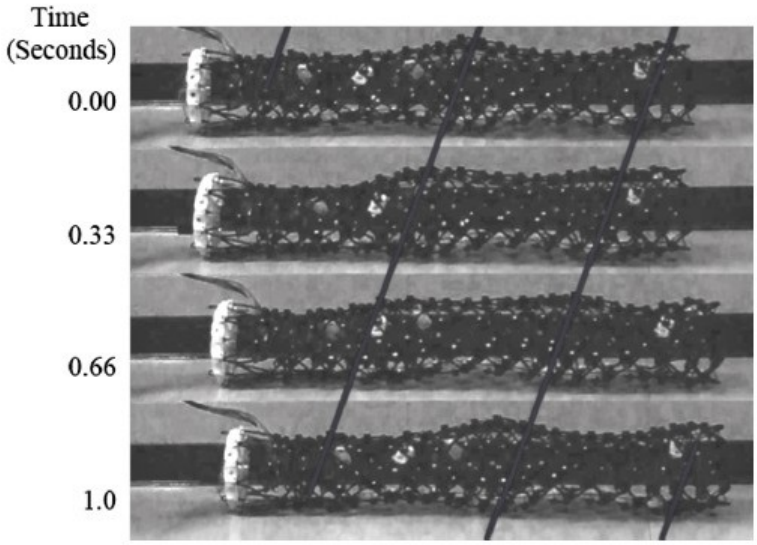

Figure 125: A peristaltic motion driven robot [88]

Another worm design is shown on Figure 126. It combines the sinusoidal motion of a snake, but in a vertical plane. This robot provides reasonable size and stability for a worm robot [85], but still needs to be experimented for tridimensional terrain.

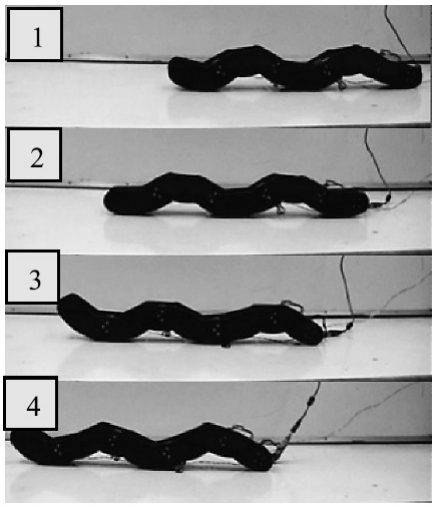

Figure 126: A snake robot based on sinusoidal snake locomotion [85]

Snake Robots The last type of biologically inspired robot locomotion method studied is the snake locomotion. This structure generates motion through friction without the use of wheels or legs.

A model that more closely mimics the motion pattern of snakes is presented on Figure 127[80, 81]. This design undulates horizontally using obstacles along its path.

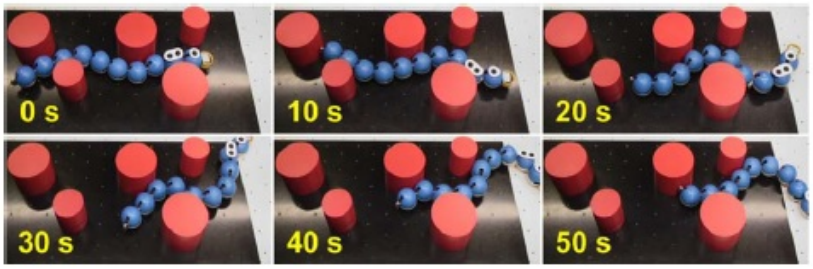

Figure 127: A snake robot based on obstacle avoidance [81]

This design is ideal for cluttered environments and planar surfaces, both of which are not typical of pipe environments. Another similar design proposes wheels to move the snake-like robot in a similar fashion [82] instead of obstacles.

Finally, another design proposes a snake robot specifically for pipe inspection en-

vironments and it is shown on Figure 128 [86, 87]. This design relies on sinusoidal motion of the robot body linkages while using the pipe walls as support. This design relies heavily on its environment to move, however in this scenario, the robot has a continuous surface to lean on and only a certain number of possible scenarios to encounter. The motion of this robot is shown on Figure 128.

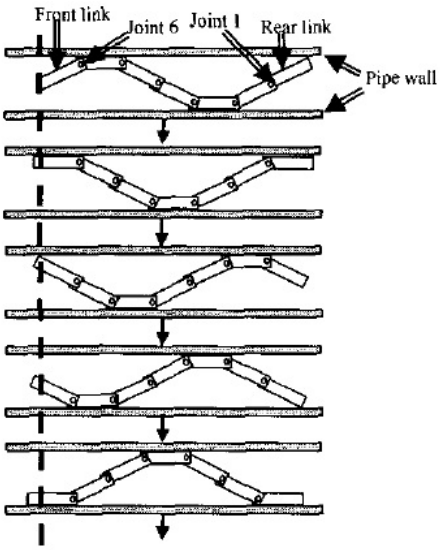

Figure 128: A snake robot using walls for locomotion [86]

This design structure has the advantage of being highly mobile in possible singular configuration scenarios, like sharp corners and T-branches. It can be adaptable to various pipe diameters as well. On the other hand, the efficiency of this kind of locomotion is unknown and is most likely low due to friction losses.